

INFRARED STUDIES OF ACTIVE GALAXIES

by

Walter Franklin Kailey

A Dissertation Submitted to the Faculty of the

DEPARTMENT OF ASTRONOMY

In Partial Fulfillment of the Requirements

For the Degree of

DOCTOR OF PHILOSOPHY

In the Graduate College

THE UNIVERSITY OF ARIZONA

1988

INFORMATION TO USERS

The most advanced technology has been used to photograph and reproduce this manuscript from the microfilm master. UMI films the text directly from the original or copy submitted. Thus, some thesis and dissertation copies are in typewriter face, while others may be from any type of computer printer.

The quality of this reproduction is dependent upon the quality of the copy submitted. Broken or indistinct print, colored or poor quality illustrations and photographs, print bleedthrough, substandard margins, and improper alignment can adversely affect reproduction.

In the unlikely event that the author did not send UMI a complete manuscript and there are missing pages, these will be noted. Also, if unauthorized copyright material had to be removed, a note will indicate the deletion.

Oversize materials (e.g., maps, drawings, charts) are reproduced by sectioning the original, beginning at the upper left-hand corner and continuing from left to right in equal sections with small overlaps. Each original is also photographed in one exposure and is included in reduced form at the back of the book. These are also available as one exposure on a standard 35mm slide or as a 17" x 23" black and white photographic print for an additional charge.

Photographs included in the original manuscript have been reproduced xerographically in this copy. Higher quality 6" x 9" black and white photographic prints are available for any photographs or illustrations appearing in this copy for an additional charge. Contact UMI directly to order.

U·M·I

University Microfilms International
A Bell & Howell Information Company
300 North Zeeb Road, Ann Arbor, MI 48106-1346 USA
313/761-4700 800/521-0600

Order Number 8905792

Infrared studies of active galaxies

Kailey, Walter Franklin, Ph.D.

The University of Arizona, 1988

U·M·I

**300 N. Zeeb Rd.
Ann Arbor, MI 48106**

INFRARED STUDIES OF ACTIVE GALAXIES

by

Walter Franklin Kailey

A Dissertation Submitted to the Faculty of the

DEPARTMENT OF ASTRONOMY

In Partial Fulfillment of the Requirements

For the Degree of

DOCTOR OF PHILOSOPHY

In the Graduate College

THE UNIVERSITY OF ARIZONA

1988

As members of the Final Examination Committee, we certify that we have read the dissertation prepared by Walter Franklin Kailey entitled INFRARED STUDIES OF ACTIVE GALAXIES

Date _____

STATEMENT BY AUTHOR

This dissertation has been submitted in partial fulfillment of requirements for an advanced degree at The University of Arizona and is deposited in the University Library to be made available to borrowers under rules of the Library.

Brief quotations from this dissertation are allowable without special permission, provided that accurate acknowledgment of source is made. Requests for permission for extended quotation from or reproduction of this manuscript in whole or in part may be granted by the head of the major department or Dean of the Graduate College when in his or her judgment the proposed use of the material is in the interests of scholarship. In all other instances, however, permission must be obtained from the author.

SIGNED: _____

Walter F. Kailay

To Jenai.

Acknowledgments

This work was largely supported by a National Aeronautics and Space Administration grant under the Graduate Student Researcher Program. I wish to take this opportunity to express my gratitude to NASA for making it all possible and even enjoyable. The National Science Foundation has also contributed to the support of this work.

I would like to thank Mark Cornell, Mike Margulis, Steve Pompea, George Rieke, and Marcia Rieke for assistance, advice, and moral and material support they gave me during the course of this work. Special thanks go to Mike for many fascinating and therapeutic games of chess. I am very grateful, too, for the help I received all along the way from my mother and father.

Thanks, above all, to my wife, Jenai, for extraordinary contributions in the form of patience, understanding, encouragement, and assistance.

Table of Contents

List of Figures	8
List of Tables	9
Abstract	10
Chapter 1. INTRODUCTION	12
Chapter 2. A STUDY OF WARM <u>IRAS</u> SEYFERTS	17
I. Introduction	18
II. Sample Selection	19
III. Observations and Data Reduction	21
A. Optical Spectroscopy	21
B. Satellite Data	24
IV. Spectral Classification	28
V. Statistical Properties of Warm <u>IRAS</u> Galaxies	32
A. Basic Statistics	32
B. Space Density of Seyferts	34
VI. Spectral Properties of Warm and Cold Seyferts	39
A. Infrared To Optical Flux Ratio	39
B. Optical Emission Line Ratios	44
VII. Summary	48
Chapter 3. IR SPECTRAL PROPERTIES OF NORMAL AND ACTIVE GALAXIES: 1. A CATALOG OF INFRARED BRIGHT GALAXIES	50
I. Introduction	51
II. Sample Selection	53
III. Basic Observational Properties of the Sample	59
A. Distances	59
B. Optical Properties	66
C. Comparison to a Control Sample	69
IV. <u>IRAS</u> Satellite Data	75
A. Processing of <u>IRAS</u> Data	77
B. Comparison with PSC Fluxes	86
V. Discussion	90
A. IR Color-Color and Color-Luminosity Relations	90
B. Single Band Luminosities	106
VI. Summary	108
Chapter 4. IR SPECTRAL PROPERTIES OF NORMAL AND ACTIVE GALAXIES: 2. THE EFFECT OF NUCLEAR ACTIVITY ON THE INFRARED COLORS OF GALAXIES	112
I. Introduction	113
II. Observations	117
A. 10 μ m Photometry	117
B. Optical Spectroscopy	126

A. Derivation	133
B. Biases in the Compactness Parameter	134
IV. Discussion	145
A. Relationship of R' to Optical Galaxy Properties	145
B. Relationship of R' to Infrared Galaxy Properties	151
V. Conclusion	159
Chapter 5. CONCLUSIONS	162
I. Summary of Results	162
II. Suggestions for Future Work	165
Appendix A. NUCLEAR REDDENING ESTIMATES FOR IBGS GALAXIES	170
List of References	174

List of Figures

2-1. log N-log S Diagram for Warm Seyferts at 25 Microns	38
2-2. 25/60 Micron Color vs. IR/Optical Flux Ratio	43
2-3. BPT Diagram for <u>IRAS</u> Seyferts	47
3-1. Total/PSC Flux versus Optical Diameter	88
3-2. <u>IRAS</u> Color-Color Diagram	101
3-3. IR Color-Luminosity Diagram	102
3-4. IR/Blue Color Luminosity Diagram	103
3-5. Second <u>IRAS</u> Color-Color Diagram	104
3-6. Second <u>IRAS</u> Color-Color Relation: Starburst Galaxies	105
4-1. Discrepancies in 10 Micron Flux Measurements	122
4-2. Percentage Errors Due to Flux Discrepancies	123
4-3. Classification of Nuclear Emission Line Ratios	132
4-4. Compactness Parameter vs. Nuclear Reddening	140
4-5. Compactness Parameter vs. Aperture / Diameter	141
4-6. Corrected Compactness Parameter vs. A/D	142
4-7. Concentration Parameter vs. Aperture / Diameter	143
4-8. Compactness Parameter vs. Morphological Type	149
4-9. Concentration Parameter vs. Morphological Type	150
4-10. Second <u>IRAS</u> Color-Color Relation	154
4-11. Compactness Parameter vs. Infrared Luminosity	155
4-12. Concentration Parameter vs. Infrared Luminosity	156
4-13. F60/F100 versus Nuclear Luminosity	157
4-14. R'xLIR vs. (Nuclear IR / Total Blue) Luminosity	158

List of Tables

2-1. Optical Spectroscopy of Warm <u>IRAS</u> Galaxies	21
2-2. Emission Line Fluxes for Warm IRAS Galaxies	23
2-3. IRAS Fluxes From Coadded Survey Scans	26
2-4. Redshifts and Classifications of Warm Galaxies	30
2-5. 25 μ m Luminosity Statistics of Warm Seyferts	36
3-1. Assumed Wavelength Boundaries of <u>IRAS</u> Filters	54
3-2. The Infrared Bright Galaxy Sample	58
3-3. Recession Velocities and Distance Estimates	62
3-4. Observational Properties of the Infrared Bright Galaxy Sample	64
3-5. The Modified Hubble Type Parameter (t)	68
3-6. Control Sample of RC2 Galaxies	73
3-7. Average Optical Properties	75
3-8. Color Corrected Total <u>IRAS</u> Fluxes for the Infrared Bright Galaxy Sample	76
3-9. IR Source Models for Extended Sources	82
3-10. Starburst Galaxy Sample	99
3-11. Fraction of L_{IR} in <u>IRAS</u> Bands	106
3-12. Squared Linear Correlation Coefficients	108
4-1. 10 Micron Nuclear Measurements of IBGS Objects	124
4-2. Nightly 10.6 μ m Sensitivity Variations	126
4-3. Spectroscopy of IBGS Galaxies	127
4-4. Emission Line Fluxes for IBGS Galaxies	128
4-5. Classification of the Nuclear Spectrum of IBGS Galaxies . . .	130
4-6. Compactness Parameters for IBGS Galaxies	144
A-1. Constants Used to Determine Reddening	171
A-2. Dust Reddening of IBGS Galaxies	172
A-3. Reddening Estimates from Published Spectroscopy	173

Abstract

IRAS observations of extragalactic objects are analyzed, supplemented by optical spectroscopy and $10\ \mu\text{m}$ photometry. The relationship between various forms of activity in the nuclei of spiral galaxies and their mid- to far-infrared spectral energy distributions is explored. It is shown that more than 70% of galaxies with $F_{60}/F_{25} \leq 3$ are Seyferts, while the remainder have bright optical emission lines in their nuclear spectra. It is argued that most Seyferts are powered by their active nuclei at $25\ \mu\text{m}$, while there is some indication that Seyferts with large F_{60}/F_{25} flux ratios are undergoing starbursts in the vicinity of their nuclei.

The properties of a sample of bright, extragalactic IRAS sources are studied. A catalog containing total infrared and blue fluxes, distance estimates, recession velocities, and morphological classifications for these objects is presented. The brightest sources at mid- to far-infrared wavelengths are (in order of frequency) nearby, normal spiral galaxies; galaxies with disturbed or irregular morphology (often known interacting galaxies); type 2 Seyferts; and dust-embedded type 1 Seyferts. All of these sources are dominated by thermal emission from dust. The dust in the peculiar, irregular, and Seyfert galaxies is exposed to a higher mean intensity of radiation. Moreover, these IR-active galaxies tend to have strong, compact nuclear sources at $11\ \mu\text{m}$, whether or not they contain a known Seyfert nucleus. The distinctive spectral behavior of IR-luminous galaxies is shown to result from the presence of compact, dust-dominated

IR nuclear sources, which are the predominant cause of IR luminosities above $10^{11} L_{\odot}$. Compact IR sources are always associated with a dust-embedded region of ionized gas in the galaxy's nucleus, which may exhibit Seyfert, LINER, or H II region characteristics. The luminosity of the compact nuclear source is well correlated with its 60/100 μm color. This relationship is a vital clue to the nature of these sources and has potential application as a standard candle.

Chapter 1

INTRODUCTION

The All Sky Survey of the Infrared Astronomical Satellite (IRAS) was carried out in less than ten months between 1983 January 26 and 1983 November 22. Yet five years after the completion of its mission, no branch of astronomy is untouched by it. In recognition of this fact, the Third International IRAS Conference at Queen Mary College in London was aptly named "Comets to Cosmology."

The study of active galaxies has been impacted by IRAS as much, if not more, than other branches of astronomy. Indeed, the discovery of a new class of active galaxies--exemplified by IC 4553 (Arp 220)--which are characterized by spectacularly peculiar morphology, unremarkable optical spectral properties, and quasar-like luminosities ($\geq 10^{12} L_{\odot}$) emerging almost entirely at far-IR wavelengths, is widely considered "the most extraordinary extragalactic discovery made by IRAS."¹

It is particularly satisfying that IRAS, the most significant contribution of modern technology to astronomy in this decade--and perhaps longer--should have its greatest impact in the field of active galaxies, for the nature of these objects is one of the longest standing problems in any of the physical sciences. The interested reader is referred to Weedman's (1976) excellent review for the history of the study of active galaxies. Here it is appropriate to sketch but a few of the relevant details.

¹Heckman, Armus, and Miley (1987).

The study of active galaxies is roughly characterized by three distinct phases. In the first phase the issue was only occasionally noticed, in passing as it were, or (later) studied (almost inadvertently) by pioneers with a predilection for the unusual, unexplained, and unknown--men such as Zwicky, Arp, Markarian, and Lipotevsky. This period began with the discovery by Slipher (1918) of the high excitation emission line spectrum of the bright stellar nucleus of NGC 1068 (a type 2 Seyfert). Slipher noted the extreme physical conditions indicated by the spectrum but offered no explanation for them. The problem was largely ignored until Seyfert (1943) pointed out the existence of vaguely similar unexplained emission nebulae in the nuclei of several bright galaxies. That a major--arguably the most important--class of active galaxies bears Seyfert's name in consequence of his single, innocuous study of them (he was subsequently interested in unrelated matters) is an ironic reminder of the inattention lavished on active galaxies during what we have termed the first phase of their study.

The second phase begins with the discovery of variability on timescales comparable to one year in the type 1 Seyfert NGC 4151 (Pacholczyk and Wymann 1968) and with Sargent's (1970) demonstration that a continuum of physical properties, including luminosity, existed between Seyfert galaxies and quasars. These findings were published five to seven years after the discovery of variability in the quasar 3C48 (Matthews and Sandage 1963), which had provided much fuel for the raging debate as to whether the redshifts of quasars were cosmological. The realization that

Seyfert galaxies were very probably nearby quasars and, of course, the converse realization that quasars were very likely situated at the center of primordial galaxies became increasingly widespread; and scientific writings on the subject of Seyferts and quasars swelled to a torrent.

Barely five years after these events, rapid technological advances in infrared detector technology made studies of extragalactic objects at wavelengths from $1\mu\text{m}$ to $100\mu\text{m}$ feasible for the first time (Rieke and Lebofsky 1979 and references therein). Three significant results emerged almost immediately from extragalactic infrared studies: the discovery of large infrared excesses with galaxy-like luminosities in the central regions of a few nearby, dusty galaxies (notably NGC 253 and M82), the discovery that many Seyfert galaxies and a few quasars are dominated by luminous emission at $10\mu\text{m}$ and longer wavelengths (Rieke 1978), and, finally, the finding that nearly half of all large spiral galaxies exhibited substantial $10\mu\text{m}$ excess (relative to expected stellar emission) in their nuclei which was probably attributable to emission from warm interstellar dust (Rieke and Lebofsky 1978; Lebofsky and Rieke 1979).

With these findings, the nuclear starburst phenomenon, as well as the importance of the infrared region of the electromagnetic spectrum to the study of active galaxies began to be widely recognized. Thus a third, distinctive phase in the study of these objects began. This most recent phase has been characterized by multi-spectral studies of active galactic nuclei and nuclear starbursts. Such studies (e.g. Rieke et al. 1980; Rieke et al. 1985; Edelson and Malkan 1986; Edelson, Malkan, and Rieke

1987; Ward et al. 1987) typically involve optical, infrared, and radio observations and often UV and X-ray data as well, with heavy emphasis on the infrared region of the spectrum.

The advent of this third phase in the study of active galaxies thus set the stage for IRAS's contribution, since widespread use of an approach stressing infrared measurements would not have been possible without the All Sky Survey, which made infrared observations between 10 μm and 100 μm available for a large, unbiased sample of extragalactic objects for the first time.

IRAS's contributions to the study of active galaxies have been reviewed by Lawrence (1988). Three aspects of this contribution stand out as particularly significant to the present work. The discovery of a new class of far-infrared galaxies with luminosities comparable to those of quasars has already been mentioned. Secondly, IRAS has focused new attention on the importance of galaxy interactions and mergers, which are primarily inferred from morphological peculiarities (e.g. Toomre and Toomre 1972), in causing galaxy activity. Thirdly, IRAS has shed new light on the relationship between normal and active galaxies and has motivated renewed interest in a unified theory of galaxy activity and the place occupied by galaxy activity in the formation and evolution of (especially late type) galaxies.

The importance of galaxy activity within any scheme of galaxy formation and evolution is widely recognized, and, in fact, could be said to be one of the primary factors motivating the great amount of attention

these objects have received since what we have called the second historical phase of their study. It is easily demonstrated by (1) the relation of Seyfert galaxies to quasars, since the latter are one of our principle observational clues to the nature of the early universe; and (2) the increasing body of observations (to which we shall contribute herein) indicating a continuum of levels and varieties of nuclear activity, even in "normal" late type galaxies.

This dissertation does not represent an attempt to unify the theory of active and normal late type galaxies. It does, however, represent a step in the direction of an eventual solution to this problem; and it is hoped that the ideas and observational evidence presented in the following chapters will help to stimulate work which will eventually lead to the attainment of that goal.

The method we have used in pursuing this objective is to attempt to understand various aspects of the IRAS database, as they relate to active and normal late type galaxies. This has been done through careful analysis of the IRAS data itself and through the ground-based acquisition and analysis of supplementary observational data. The considerations adduced above should make the value of such an approach to the study of late type galaxies sufficiently obvious. However, it should be kept in mind that understanding the IRAS database (or any portion thereof) is not an end in itself, but rather a means to an end.

Chapter 2

A STUDY OF WARM IRAS SEYFERTS¹

Abstract

The properties of galaxies with abnormally blue 25/60 μm flux ratios ("warm" galaxies) are discussed. It is shown that, after exclusion of previously known Seyferts from the sample, more than 70% of galaxies with $F_{60}/F_{25} \leq 3$ for which optical spectroscopy is available are Seyfert galaxies and that most are of type 2. It should be possible to discover ~130 new Seyferts in this way, all detected by IRAS at 25 μm and lying more than 30° from the Galactic plane. The space density of Seyfert galaxies which do and don't meet this color criterion is discussed. The newly discovered type 2 Seyferts have a space density comparable to known Markarian Seyfert galaxies but less than type 2 Seyferts in the CfA redshift survey. The 25 μm emission of most Seyferts appears to be dominated by their nuclei, while much evidence from this work and previous studies indicates Seyferts with steeply rising far infrared spectra ("cold" Seyferts) are dominated by star formation regions at 60 μm and 100 μm . We find that the cold Seyferts have significantly lower 25 μm luminosities, which is consistent with these ideas. The nuclear optical emission line ratios of cold type 2 Seyferts are intermediate between those of warm Seyferts and H II regions, suggesting regions of massive star formation exist in the

¹This material was previously published in the Astrophysical Journal, Vol. 326, pp. 653-661.

immediate vicinity of the nucleus.

I. Introduction

One of the earliest results in the study of active galactic nuclei to emerge from the Infrared Astronomical Satellite (IRAS) was the development of a method for efficiently selecting Seyfert galaxies based on their abnormally flat or "warm" 25/60 μm flux ratios. Galaxies exhibiting such flux ratios are commonly referred to as "warm IRAS galaxies." Discovery of new Seyfert galaxies among warm IRAS galaxies has been carried out successfully by Carter (1984; hereafter C84) and de Grijp *et al.* (1985; hereafter dG85). Osterbrock and de Robertis (1985; hereafter OdR) have summarized and added to the results of these authors. Since the pre-IRAS sample of Seyfert galaxies has long been known to suffer from bias against type 2 Seyferts (e.g. Simkin, Su, and Schwarz 1980; Phillips, Charles, and Baldwin 1983; Osterbrock 1984) and against heavily reddened and IR bright objects (Rudy 1984; Rieke 1978), it was hoped that the warm IRAS galaxies--possibly in conjunction with other selection techniques--might provide a more unbiased sample of Seyferts. In addition, new insights into the emission mechanisms operating in Seyferts might result from studying such a sample.

We report in this chapter the results of a study of warm IRAS galaxies carried out with the goals of understanding the statistical properties of Seyfert galaxies selected on the basis of 25/60 μm flux ratios and the physical properties which distinguish them from normal

galaxies, as well as other Seyfert galaxies.

II. Sample Selection

Galaxies may be efficiently selected from the IRAS Point Source Catalog (Beichman et al. 1985b; hereafter PSC) by requiring a detection at 60 μm and also that the flux density in this band exceed the flux or flux limit at 12 μm (Soifer et al. 1984). Occasional stars satisfying these criteria must be subsequently removed from the sample. It is necessary to impose a color criterion, and hence the requirement of detection in some band other than 60 μm , in order to segregate Seyferts from normal galaxies. Adding the requirement of a 25 μm detection gives an essentially monochromatic flux limited sample (increasingly incomplete at fainter 25 μm fluxes), since the 25 μm flux of galaxies is almost always less than the 60 μm flux, whereas IRAS was more sensitive at the latter wavelength. For the 221 galaxies selected in this way from among the first 5000 high latitude PSC entries, the average spectral index (α , $F_\nu \propto \nu^\alpha$) between 25 μm and 60 μm is $\langle \alpha_{25,60} \rangle = -2.04 \pm .64$. Of this sample, 88% were detected at 100 μm as well with $\langle \alpha_{60,100} \rangle = -1.14 \pm .80$.

We define the term "warm IRAS galaxies" to mean objects selected as outlined above for which the ratio of $F_{60}/F_{25} \leq 3$, which corresponds to $\alpha_{25,60} \geq -1.25$. The test is made without applying the (small) color corrections to the PSC fluxes. Objects which do not meet this criterion are occasionally referred to as "cold" galaxies. It should be pointed out that our definition differs slightly from those employed by C84, dG85,

and OdR and that about half of known Seyferts are not warm. Furthermore, the CfA Seyfert galaxy sample (Edelson 1987), which was flux limited using Zwicky photographic magnitudes and subsequently selected by optical spectroscopy contains 26 cold Seyferts, 13 warm Seyferts, and 6 ambiguous cases. Thus warm Seyferts constitute a significant portion but not a majority of Seyfert galaxies; their main importance, however, derives from the extremely high percentage of warm galaxies which are Seyferts (see Section V), which suggests a causal connection between the Seyfert phenomenon and the mid-infrared emission in these objects.

We have obtained optical spectroscopy on two samples of warm IRAS galaxies. The galaxies and dates of observation are given in Table 2-1. The first sample (galaxies with 1 under Date in Table 2-1) consists of eight galaxies chosen from IRAS Circulars 11 and 16, which were not known Seyferts at the time of observation. The IRAS circulars were short lists of IRAS sources and fluxes released before the full PSC. Four of these galaxies have also been observed by OdR or dG85, as indicated in Table 2-1.

Table 2-1
Optical Spectroscopy of Warm IRAS Galaxies

Designation	α (1950.0)	δ (1950.0)	Dates ^a	Comments
MCG 2-3-22	00 ^h 46 ^m 37. ^s 8	-12°45'27"	1,2	not warm, <u>PSC</u> error
IRAS 0135-13	01 35 37.6	-13 07 28	1	
ESO 543-G11	01 37 51.3	-22 30 16	2	
NGC 839	02 07 15.9	-10 25 10	2	not warm, <u>PSC</u> error
ZG 0229+02	02 29 04.4	+02 35 13	2	
NGC 1163	02 58 03.3	-17 20 58	2	not warm? <u>PSC</u> error
MCG 2-8-39	02 58 04.0	-11 36 55	2	
UGC 2514	03 01 16.5	-01 17 53	2	
NGC 1320	03 22 17.7	-03 13 05	2	
IRAS 0425-07	04 25 22.6	-07 15 17	1,2	
IRAS 0425-04	04 25 56.9	-04 40 25	1,2	also in OdR
IRAS 0428-09	04 28 10.8	-00 44 09	1,2	also in OdR
IRAS 0450-03	04 50 14.1	-03 17 54	1	also in OdR
IRAS 0521-12	05 21 48.6	-12 45 27	1	also in dG85, OdR
UGC 4085	07 51 26.3	+53 27 45	2	not warm, <u>PSC</u> error
IRAS 2121-17	21 21 54.1	-17 57 43	1	

Notes to Table 2-1

a. Observing dates are (1) 22 and 23 September 1984, and (2) 30 November and 1 December 1986.

The second sample (galaxies with 2 under Date in Table 2-1) consists of all 12 warm IRAS galaxies in the PSC with $0^h < \alpha < 8^h$, $\delta > -25^\circ$, $|b| > 30^\circ$, and $F_{25} > .2$ Jy which were either known to be non-Seyfert galaxies or known galaxies which were not known Seyferts. There is an overlap of four objects with the previous sample.

III. Observations and Data Reduction

A. Optical Spectroscopy

Optical spectra of the objects in the first sample were obtained on the nights of 22 and 23 September 1984 using the Steward Observatory 90" telescope on Kitt Peak, the Boller & Chivens spectrograph with a 600 mm^{-1}

grating blazed at 3568 Å, and a blue sensitive Carnegie image tube followed by a pulse counting Reticon array. The Reticon pixel covered 1 Å, and the 3" circular aperture resulted in 5.6 Å resolution over the range 3500 Å to 6200 Å in the final spectrum. This resolution is the average full width at half maximum of night sky lines in our spectra after fitting a dispersion curve and rebinning the data. Sky and object spectra were taken simultaneously through apertures separated by 10" in right ascension. The telescope was wobbled between the apertures every four minutes during the observations, which lasted between 16 and 64 minutes for each object.

Standard stars from Oke (1974; EG 26 and EG 145) were used for flux calibration. Both standards were observed twice, and one of these was thrown out due to poor seeing (4"). The remaining standard star observations and all of the galaxy observations were made under photometric conditions with 2".5 seeing. The data were reduced and redshifts and line fluxes measured using the Interactive Reduction System at Steward. We estimate that the RMS error in our absolute flux calibration due to seeing and guiding errors using a small (3") aperture is not more than 20%. Flux ratios for the brighter lines are good to 10%. Flux ratios marked by a colon (see Table 2-2) have uncertainties of 30% or larger due to poor continuum estimation by the reduction software, a blend of emission and absorption features at the same or nearby wavelengths, or blended emission features. The fluxes in Table 2-2 were normalized such that the total flux in [O III] $\lambda\lambda 4959, 5007$, $F_{[OIII]}=100$.

In one case (IRAS 0428-09) where this value was not available, the flux of [O II] $\lambda 3727$ was set to 100. In the case of IRAS 2121-17, the $\lambda 4959$ flux could not be reliably measured and was set equal to one third of the $\lambda 5007$ flux. The last column in Table 2-2 gives the logarithm of $F_{[OIII]}$ in $\text{erg cm}^{-2} \text{s}^{-1}$. Values marked with a colon in this column are uncertain by $\sim \pm 0.3$.

Table 2-2
Emission Line Fluxes for Warm IRAS Galaxies

Designation	[Ne V]	[O II]	H δ	H γ	[O III]	He II	H β	H α	[N II]	[S II]	[S II]	[O III]
λ	3425.8	3727.3	4101.7	4340.5	4363.2	4685.7	4861.3	6562.8	6583.4	6717.0	6731.3	Flux
IRAS 0135-13	8.1	3.2	...	0.9	3.5	3.1	3.1	-12.7
ESO 543-G11	...	9.0	18.9	37.8	...	2.2:	91.9:	237.5	-13.1:
ZG 0229+02	...	275.0	...	19.9:	72.8	280.7	57.0	30.5:	47.0:	-13.6:
MCG 2-8-39	...	4.4:	0.6	2.3	1.7	2.4	4.8	12.9	11.4	2.8	2.1	-12.7:
UGC 2514	5.0:	22.5	15.0	-13.2:
NGC 1320	3.3	3.1	3.6	6.2	22.6	15.2	3.2	4.1	-12.7:
IRAS 0425-07	...	32.1	4.8	9.5	0.8	...	21.4	55.0	11.9	-12.8
IRAS 0425-04	...	52.3	147.0	97.3	44.1	46.0	-14.3
IRAS 0428-09	...	100.0	116.8:	59.0:
IRAS 0450-03	...	10.1	...	1.1	3.5	4.3	4.3	-13.1
IRAS 0521-12	10.0	6.7	...	33.8:	2.8:	3.2	59.4	-12.4
IRAS 2121-17	53.0:	...	69.9:	336.4:	452.8:	-13.1:

The second sample of warm galaxies was observed on 30 November and 1 December 1986. The telescope and instrument were as given above, and the observing procedure was changed as follows: A 300 mm^{-1} grating and dual 2"5X5" slits with 25" separation were used, resulting in 8 Å resolution. A filter with zero transmission shortward of 3600 Å was used to block the second order light in the red, giving useful data from 3800

Å to 7200 Å. Redshifts were determined as with the previous data, while flux calibration was accomplished within the National Optical Astronomy Observatory's Interactive Reduction and Analysis Facility (IRAF, version 2.5). Line fluxes from these spectra were measured using IRAF's deblending routine, which fits a gaussian profile to the lines assuming the width of all lines in the blend to be the same. This procedure is inadequate when absorption features are present and for Seyferts of type 1 or composite types, but produces very reliable fluxes in other cases. We estimate the line flux ratios from these spectra (also in Table 2-2) to be typically accurate to $\pm 10\%$. Because of the narrow slit used and poorer seeing ($\sim 3''$) during these observations, the absolute flux calibration is not reliable; the values of $\log F_{[\text{OIII}]}$ derived from these spectra are marked with colons (uncertainty $\sim \pm 0.3$) in Table 2-2.

B. Satellite Data

One dimensional coadded IRAS survey data were obtained from the Infrared Processing and Analysis Center (IPAC) for objects in the second sample in order to make better estimates of the fluxes in the IRAS bands. The IPAC software (ADDSCAN) provides a choice of flux estimators, which are described in the IPAC User's Guide (Persson 1986). All of the estimators agree very well for bright, unconfused sources. We used FNU(T) for the weighted mean of all scans in all cases where special problems were not encountered. This is essentially equivalent to aperture photometry with background subtraction using an aperture just larger than

the IRAS beam centered on the PSC coordinates of the source. Although the PSC confusion and cirrus flags did not indicate obvious difficulties with any of these sources, problems with the data arose frequently; and we now discuss them.

Some the sources were situated near one or more large positive or negative excursions from the background ("spikes" which were seen only in the 12 μm or 25 μm bands) or near an abrupt change in the background level. In these cases the flux was estimated from either the peak of a point source template plus sloping background fitted to the data or the integral between zero crossings of the flux or an average of these estimators. The noise was set equal to the largest noise estimate whose corresponding flux estimator was used in the average. In two extreme cases, no meaningful estimate of the flux could be made due to these problems. The flux estimates in all four IRAS bands and corresponding noise estimates are in Table 2-3.

Table 2-3
IRAS Fluxes From Coadded Survey Scans

Designation	F ₁₂	s ₁₂	F ₂₅	s ₂₅	F ₆₀	s ₆₀	F ₁₀₀	s ₁₀₀
MCG 2-3-22	236	69	1500	33	2270	94
ESO 543-G11	90	24	390	32	610	24	590	108
NGC 839	540	31	2570	63	14260	51	17960	137
ZG 0229+02	70	30	210	33	600	42	1250	108
NGC 1163	180	32	760	35	2180	71
MCG 2-8-39	280	19	440	27	530	41	980	93
UGC 2514	280	23	880	36	930	35	770	213
NGC 1320	260	34	1350	27	2320	29	2910	138
IRAS 0425-07	70	24	270	21	700	27	1260	123
IRAS 0425-04	170	22	1550	31	4270	27	4000	84
IRAS 0428-09	70	19	300	19	550	22	880	341
UGC 4085	100	22	210	33	1610	26	3530	103

The IPAC User's Guide (Persson 1986) warns of a possible tendency of the ADDSCAN program systematically to overestimate fluxes as compared with the PSC. This tendency has been confirmed by Claussen *et al.* (1987), who find a +5% discrepancy at 12 μm and +10% at 25 μm . Our data also confirm the trend and allow us to quantify it (at least for sources slightly above the detection limits) at the longer wavelengths. Based on ADDSCAN fluxes for the twelve warm galaxies currently under discussion and twelve other galaxies selected for cold to average 25/60 μm flux ratios, we find the ADDSCAN fluxes systematically larger than the PSC fluxes by $36\pm 15\%$, $17\pm 11\%$, $15\pm 6\%$, and $10\pm 3\%$ at 12 μm , 25 μm , 60 μm , and 100 μm respectively. The errors are the standard error in the mean. PSC fluxes marked as uncertain were included in these statistics, although they were found to disagree more strongly with the ADDSCAN fluxes, often by factors of .5 to 2. If these fluxes are excluded, the ADDSCAN fluxes are found

to be higher by $23\pm 11\%$ and $9.5\pm 2.5\%$ at $25\ \mu\text{m}$ and $60\ \mu\text{m}$ respectively. Based on these figures, a conservative downward correction of 10% was applied to the ADDSCAN fluxes before using them in any computation or comparison with other fluxes. The values in Table 2-3 have not been so corrected.

In three cases the ADDSCAN fluxes reveal that the classification of the object as a warm IRAS galaxy was due to large errors in the PSC fluxes, and in a fourth case there is reason to doubt strongly the PSC flux. Comments to this affect appear opposite these sources in Table 2-3. A discussion of the individual sources follows.

MCG 2-3-22: The $25\ \mu\text{m}$ flux estimate given by the PSC exceeds that derived by ADDSCAN by a factor of two. The signal to noise ratio in the band is about 3 to 1, but a negative noise spike only slightly weaker than the source itself appears in the coadded $25\ \mu\text{m}$ data separated from the source by about $1'$ and is worst in the weighted mean coadd.

NGC 839: The PSC flux at $60\ \mu\text{m}$ is low by a factor of 2.5. There is a nearby point source, which is unresolved at $100\ \mu\text{m}$. The separation of the two sources is $\sim 2.5'$, and they have virtually identical signal at $60\ \mu\text{m}$. Both sources are clearly visible in the individual scans. The $60\ \mu\text{m}$ and $100\ \mu\text{m}$ fluxes given in Table 2-3 were derived by assuming the flux of the confusing source equal to that of NGC 839 and dividing their joint flux by two. This agrees with the point source template fit at $60\ \mu\text{m}$ to within 20%. Furthermore this amount of contamination is about what one would expect based on the $60\ \mu\text{m}$ point spread function of IRAS (Beichman

et al. 1985a) and the separation of the sources. It is unclear what caused the error in the PSC 60 μm flux estimate.

NGC 1163: This galaxy probably does not have a "warm" 25/60 μm flux ratio. The coadded survey data are too noisy at 25 μm to allow any meaningful estimate of the source flux. There is a fairly large noise peak which coincides roughly with the source position, but it is in no way distinguishable from similar peaks throughout the data, and its position and height are most properly regarded as a coincidence.

UGC 4085: A low spacial frequency component of the 25 μm noise results in a background level in the immediate vicinity of the source which is depressed below the local mean. FNU(T) is negative, despite the appearance of an obvious point source. The peak flux of a point source template fitted to the data was used to estimate F_{25} and results in a flux level well below that published in the PSC. The source is not a warm galaxy.

IV. Spectral Classification

We have classified our optical spectra as those of Seyfert galaxies; H II region galaxies; Low Ionization Nuclear Emission Regions (LINERs); or Transition galaxies, which are intermediate between the last two types. The classifications are as defined and discussed in OdR. The four objects in our sample in common with OdR were classified without reference to the OdR results and found to agree. This group included a type 1.5 Seyfert, a type 2 Seyfert, a LINER, and a Transition galaxy. Table 2-4 contains

redshifts and spectral classifications for all warm Seyferts discovered using IRAS to date. Objects which are not warm IRAS galaxies or which were known to be Seyferts before the IRAS data were released have been excluded from this table. Following OdR, we have listed the warm IRAS galaxies by a shortened IRAS designation. Alternative designations, where available, are given in the last column of the table for the galaxies observed in this work.

Table 2-4
Redshifts and Classifications of Warm Galaxies

IRAS Name	meas. z	avg. z	Class.	Comments
0135-13	.0403	.0403	2	
0137-22	.0862	.0862	1.5	ESO 543-G11
0229+02	.0275	.0275	H	ZG 0229+02
0258-11	.0298	.0298	2	MCG 2-8-39
0301-01	.0134	.0134	L	UGC 2514
0322-03	.0090	.0090	2	NGC 1320
0425-07	.0988	.0988	H	
0425-04	.0154	.0155	L	
0428-09	.0468	.0468	T	
0450-03	.0161	.0159	2	
0521-12	.0490	.0490	1.5	
0611-320500	2	
1051-271606	2	
1105-110546	2	
1119+040382	H	
1121-280136	2	
1246-110476	2	
1249-130137	1	
1304-230095	2	
1305-240137	H	C84 classification
1319-160167	2	
1431-320255	2	
1509-210441	1	
1524+000505	2	
1548-030300	2	
1832-590194	1.8	C84 classification
2121-17	.111:	.111:	1	

Redshifts measured from our spectra appear in the first column of Table 2-4. Those in the second column are averages of our measurements with the average redshift over C84, dG85, and OdR, as published in OdR. Agreement between our results (based on all bright emission lines in our spectra) and the average redshifts in OdR is excellent; the redshifts are accurate to the number of digits given in the table.

Classifications of objects not observed by us are taken from OdR with two exceptions, which are noted in the table. The meaning of the symbols in the fourth column of Table 2-4 is as follows: H for H II region galaxy; T for Transition galaxy (intermediate between types H and L); L for LINER; 1, 1.5, 1.8, 2 for the corresponding Seyfert types [see Osterbrock and Dahari (1983) for a description of types 1.5 and 1.8]. Hereafter the spectral classes are occasionally referred to by these symbols, and objects of type 1, 1.5, and 1.8 (all of which possess broad emission line regions) are referred to as type 1. The C84 and OdR classifications disagreed in the case of IRAS 1305-24, 1319-16, and 1832-59. We prefer the C84 classification of 1305-24 as type H, based on its $\lambda 5007/H\beta$, $\lambda 3727/\lambda 5007$, and $\lambda 5007/\nu F_{\nu}(60 \mu m)$ flux ratios, all of which are typical of type H objects and abnormal for type 2 (Baldwin, Phillips, and Terlevich 1981; hereafter BPT; Section VI.A). We have adopted the OdR classification of 1319-16 as type 2 based on their discussion and their Figure 2. We have adopted the C84 classification of 1832-59 as type 1.8 based on the discussion in C84 and references therein.

There is a much higher incidence of Seyfert galaxies in Table 2-4 than in the corresponding table of OdR (Table VII). This results from the exclusion of galaxies not detected at $25 \mu m$ by IRAS, which inheres in our definition of warm IRAS galaxies. The large fraction of objects of types H, L, and T found by OdR among their sample are predominantly those listed by dG85 with IRAS $25 \mu m$ upper limits greater than $1/3$ of their $60 \mu m$ flux. It is clearly useful to exclude these objects from consideration. The

incidence of various forms of nuclear activity among warm IRAS galaxies will be discussed further in the next section.

V. Statistical Properties of Warm IRAS Galaxies

A. Basic Statistics

Inspection of Table 2-4 reveals that all of the warm IRAS galaxies exhibit nuclear emission lines in their optical spectra, as previously concluded by C84 and OdR. More significantly, 74% of these objects are Seyfert galaxies, after exclusion of previously known Seyferts from the sample. The Seyferts are 70% type 2 and 30% type 1. Before exclusion of previously known Seyferts, warm galaxies are 79% Seyferts.

This high incidence of type 2 Seyferts is in fact the only significant difference between the IRAS-discovered warm Seyferts and the pre-IRAS warm Seyferts and almost certainly accounts for their omission from the latter group. The well known bias against type 2 Seyferts among optically discovered Seyfert galaxies has been alluded to above. It is easily demonstrated by the fact that 67% of the 69 warm Seyferts in the catalog of Véron-Cetty and Véron (1985) are of type 1. OdR found the IRAS-discovered type 2 Seyferts to be more highly reddened on average than Koski's (1978) optically selected sample; but extreme dust reddening of the new warm type 2 objects is probably not the main cause of this bias, since Edelson and Malkan (1986) and Kailey and Lebofsky (1987) have found strong indications that the most heavily reddened Seyferts have cold mid-infrared spectra. The OdR result is most easily understood by noting that

Koski's type 2 Seyferts were mostly made up of Markarian galaxies, which tend to have warm mid-infrared colors and modest (for type 2 Seyferts) amounts of dust.

To assess what impact the new population of IRAS-discovered Seyferts is likely to have on the Seyfert galaxy luminosity function, we have selected a complete sample of warm IRAS galaxies from the IRAS database at IPAC. The sample consists of all objects in the PSC with Galactic latitude $|b| \geq 30^\circ$ with at least grade 2 fluxes at $60 \mu\text{m}$ and $25 \mu\text{m}$ [see Beichman et al. (1985a)] having $F_{60} > F_{12}$ and $F_{60}/F_{25} \leq 3$, which are not associated with a known Galactic object, such as an SAO star, a planetary nebula, or a molecular cloud. The restriction of the sample to high Galactic latitude greatly reduces the problem of contamination of the sample by Galactic objects, which becomes increasingly common for warm sources within 30° of the Milky Way. A plot of the logarithm of the number of objects brighter than a given flux level versus the logarithm of that flux level (a log N-log S plot) has a slope -1.5 , indicating completeness of the sample and a uniform distribution of the objects in Euclidean space, out to $.29 \text{ Jy}$. There are 223 objects in the sample brighter than this limit in the 6.1 sr of sky included.

Taking account of the flux limit and coverage, there are among the 223 warm IRAS galaxies in our flux limited sample about 31 known type 1 Seyferts and 16 known type 2 Seyferts, excluding the IRAS-discovered Seyferts in Table 2-4. We expect 74% of the remaining 176 warm galaxies to be Seyferts: 91 of type 2 and 39 of type 1. Combining these with the

pre-IRAS known warm Seyferts, the complete sample contains 70 type 1 Seyferts and 107 type 2 Seyferts.

B. Space Density of Seyferts

The results just derived can be used to estimate the space density of warm Seyferts. The fraction of all Seyferts which are warm can then be determined by comparing this to the best available estimate of the space density of all Seyferts. The number of objects per unit luminosity in a flux limited sample,

$$N(L, F_{\min}) dL = \phi(L) dL \int_0^{R_{\max}(L, F_{\min})} \Omega R^2 dR, \quad (1)$$

where $\phi(L)$ is the luminosity function of the objects, F_{\min} is the flux limit, and Ω is the solid angle surveyed. $R_{\max}(L, F_{\min})$ is the maximum distance to which objects of luminosity L will be included in the sample:

$$R_{\max} = 1/2\pi^{-1/2} F_{\min}^{-1/2} L^{1/2}. \quad (2)$$

The solution for the space density is straightforward:

$$\rho = \int_0^{\infty} \phi(L) dL = (24\pi^{3/2}/\Omega) N(F_{\min}, \Omega) F_{\min}^{3/2} \langle L^{-3/2} \rangle. \quad (3)$$

Here $N(F_{\min}, \Omega)$ is the total number of objects in the sample with flux limit F_{\min} over solid angle Ω and $\langle \dots \rangle$ indicates the average over objects in the sample. From equation (1) it is apparent that $N(L, F_{\min})$ is separable in L and F_{\min} . Therefore $\langle L^{-3/2} \rangle$ will be independent of the flux limit of the sample used to determine it; in fact, it will be the

same for incomplete samples as well as complete ones, so long as the incompleteness is a function only of the flux level.

The cumulative 25 μm flux distribution of currently known warm IRAS Seyferts is shown in Figure 2-1. The figure shows that neither the pre-IRAS warm Seyferts, nor the IRAS-discovered warm Seyferts suffer from any severe bias in 25 μm flux at flux levels brighter than .4 Jy. Such a 25 μm flux bias would be expected if the effective optical flux limit of the optically selected sample were so bright that a significant number of objects have $F_{25}/F_{\text{optical}} < F_{\text{min}}(25 \mu\text{m})/F_{\text{min}}(\text{optical})$ and can be seen, for example, in the 25 μm flux distribution of the CfA Seyfert galaxy sample.

We have computed the average 25 μm luminosity density, $\langle L_{25} \rangle$, as well as $\langle L_{25}^{-3/2} \rangle$ for the pre-IRAS warm Seyferts, the IRAS-discovered warm Seyferts, and for both groups jointly (broken down by Seyfert type), using only objects with $F_{25} > .4$ Jy (since it is conceivable that the bias at very low flux levels depends in some way on luminosity). There is no measurable, statistically significant difference between the IRAS-discovered and pre-IRAS Seyfert populations in either of these quantities. It is therefore appropriate to use the value of $\langle L^{-3/2} \rangle$ for both groups jointly in determining the space density of warm Seyferts. These statistics, assuming a Hubble constant of $75 \text{ km s}^{-1} \text{ Mpc}^{-1}$, are listed in Table 2-5.

Table 2-5
25 μ m Luminosity Statistics of Warm Seyferts

Group	$\langle L_{25} \rangle$ (erg s ⁻¹ Hz ⁻¹)	$\langle L_{25}^{-3/2} \rangle$ (erg ^{-3/2})
Type 1	(2.56 \pm 1.02)x10 ³¹	(5.41 \pm 3.84)x10 ⁻⁴⁶
Type 2	(1.40 \pm 0.29)x10 ³⁰	(1.16 \pm 0.30)x10 ⁻⁴⁶
Both	(2.07 \pm 0.61)x10 ³¹	(3.62 \pm 2.23)x10 ⁻⁴⁶

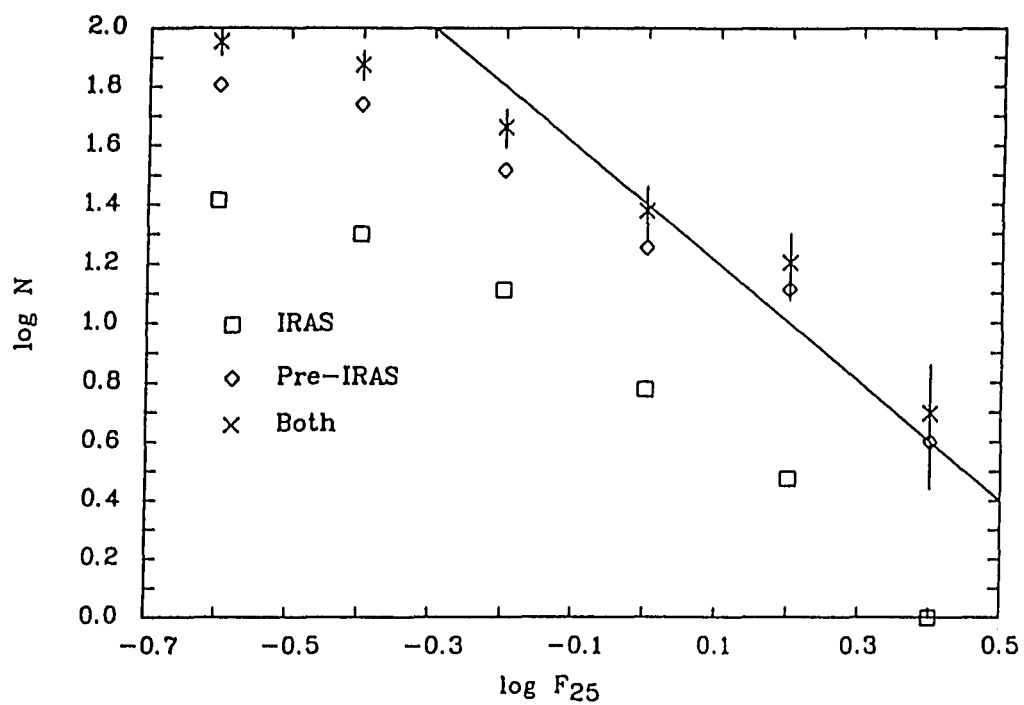
Using equation (3) and the results of the previous section, the space density of warm IRAS Seyferts is: (type 1) (1.1 \pm .8)x10⁵, (type 2) (4.4 \pm 1.1)x10⁴, and (types 1 and 2) (2.1 \pm 1.3)x10⁵ Gpc⁻³. The values for type 1 and for both types are not well determined. This is due to the wide range of 25 μ m luminosity densities exhibited by type 1 Seyferts, which makes accurate determination of the moments of the distribution difficult. More specifically, the 25 μ m luminosity function of warm type 1 Seyferts does not turn over sufficiently rapidly at the low luminosity end to allow an accurate measurement of their integrated space density using IRAS. A more accurate value for the space density of warm type 1 Seyferts can be derived using optical fluxes, if and when they become available for these objects.

For comparison, we have applied this method of determining space densities to optical flux limited subsets of the CfA Seyfert galaxy sample (Edelson 1987) and the Markarian Seyferts (Meurs and Wilson 1984) using blue luminosities. Flux densities in the B photometric band were derived

from the Zwicky photographic magnitudes in both instances. The space densities derived in this way are in good agreement with those obtained by summing over the 60 μm luminosity function of the CfA Seyferts published by Edelson, Malkan, and Rieke (1987; hereafter EMR) and the optical luminosity function of Markarian Seyferts published by Meurs and Wilson. For the CfA sample, we obtain space densities of (type 1) $(1.2 \pm 0.5) \times 10^5$, (type 2) $(4.8 \pm 2.1) \times 10^4$, and (types 1 and 2) $(1.7 \pm 0.5) \times 10^5 \text{ Gpc}^{-3}$; and for the Markarian Seyferts, we obtain (types 1 and 2) $(4.7 \pm 1.8) \times 10^4 \text{ Gpc}^{-3}$. All values are reduced to a Hubble constant of $75 \text{ km s}^{-1} \text{ Mpc}^{-1}$.

We conclude that the space density of the various groups of Seyfert galaxies considered are all within a factor of a few of each other and of the order of 10^5 Gpc^{-3} , in agreement with EMR. If the spectroscopically selected CfA Seyferts represent the true Seyfert population, then it is about three times as dense as the Markarian Seyfert galaxies. Warm type 2 Seyferts are about as dense as Markarian Seyferts, and the space density of warm Seyferts overall is not well determined but would appear to lie somewhere between that of the Markarian Seyferts and the CfA Seyferts.

Figure 2-1
log N-log S Diagram for Warm Seyferts at 25 Microns



VI. Spectral Properties of Warm and Cold Seyferts

A. Infrared To Optical Flux Ratio

In discussing the 25/60 μm colors of Seyfert galaxies, it is important to recall the degree of variation among Seyferts in this property: $\alpha_{25,60}$ typically ranges from -2.5 to 0 with roughly one half of known Seyferts on either side of -1.25. The fact that $\alpha_{25,60}$ is an extremely efficient predictor of Seyfert activity among the warmest objects establishes a causal link between the Seyfert nucleus and the 25 μm and/or 60 μm emission in these galaxies. Further insight can be obtained by examining the relationship of the 25/60 μm flux ratio to the global characteristics of the spectral energy distribution.

The nuclear [O III] $\lambda 5007$ emission line flux is a good indicator of the optical power emitted by a Seyfert nucleus, since it has been shown to scale with the strength of the nonthermal continuum (Yee 1980) and because it is not expected to vary on timescales shorter than the light-travel time for the narrow-line region, say 300 to 1000 years. To study the IR to optical flux ratios of Seyferts, we have assembled $\lambda 5007$ fluxes for IRAS-discovered warm Seyferts from this work, C84, and OdR. Emission line fluxes for a large sample pre-IRAS known Seyferts have been taken from Yee (1980). Measurements of a few additional objects were taken from C84 (three warm type 1 Seyferts), our unpublished spectra of UGC 12138 and NGC 1229 (warm Seyferts) taken on 24 September 1984, and our unpublished spectrum of VII Zw 73 (a cold Seyfert) taken on 30 November 1986. We have

assumed a $\lambda 5007/\lambda 4959$ flux ratio of 3 where necessary in computing the $\lambda 5007$ flux (F_{5007}) from the published measurements.

In Figure 2-2 we have plotted the $60\ \mu\text{m}$ to $25\ \mu\text{m}$ flux density ratio against $\nu F_\nu/F_{5007}$ for frequencies, ν , corresponding to $25\ \mu\text{m}$, $60\ \mu\text{m}$, and $100\ \mu\text{m}$. In the figure IRAS-discovered Seyferts are shown as asterisks and pluses (types 1 and 2), while pre-IRAS Seyferts are indicated with 1's and 2's. The combination of intrinsic scatter and measurement error is apparently large enough to overwhelm any systematic differences between these classes of Seyferts in IR to optical flux ratio. If the type H warm IRAS galaxies were plotted in Figure 2-2, they would lie well above the warm Seyferts in IR to $\lambda 5007$ luminosity.

The ratio of $25\ \mu\text{m}$ luminosity to $\lambda 5007$ luminosity is uncorrelated with $\alpha_{25,60}$; the linear correlation coefficient indicates a probability of slightly greater than 50% of obtaining a better correlation from random data. At $60\ \mu\text{m}$ the correlation of the two flux ratios is greater than 99.9% significant using the same test, and the slope of the regressed relation is $1.2 \pm .3$. At $100\ \mu\text{m}$, the relation is even more significant and has a slope of $1.8 \pm .4$. From this we conclude that the principal difference between the cold and warm Seyferts lies at wavelengths greater than $25\ \mu\text{m}$, and that the cold Seyferts have an excess of this long wavelength emission, as compared with the warm Seyferts. Furthermore, the excess emission rises significantly more steeply than ν^{-1} between $60\ \mu\text{m}$ and $100\ \mu\text{m}$.

This spectral behavior is suggestive of star formation in the disk of the cold Seyferts in sufficient quantity to overwhelm the far infrared spectrum of the Seyfert nucleus. If we compare the 25/60 μm flux ratios of 20 IRAS point sources in the disks of M31 and M33 (which are presumably star formation sites in these galaxies), we find their average $\alpha_{25,60}$ is -2.33, which is comparable to that of the coldest Seyferts. None of the M31 or M33 sources have $\alpha_{25,60} > -1.25$, and only one comes within .1 of this value. Extreme examples of cold Seyferts with strong star formation in the vicinity of their nuclei are provided by the heavily obscured type 2 Seyfert, Arp 220 (Rieke et al. 1985), which has $\alpha_{25,60} = -2.90$, and the type 1 Seyfert NGC 7469 (Cutri et al. 1984), which has $\alpha_{25,60} = -1.80$.

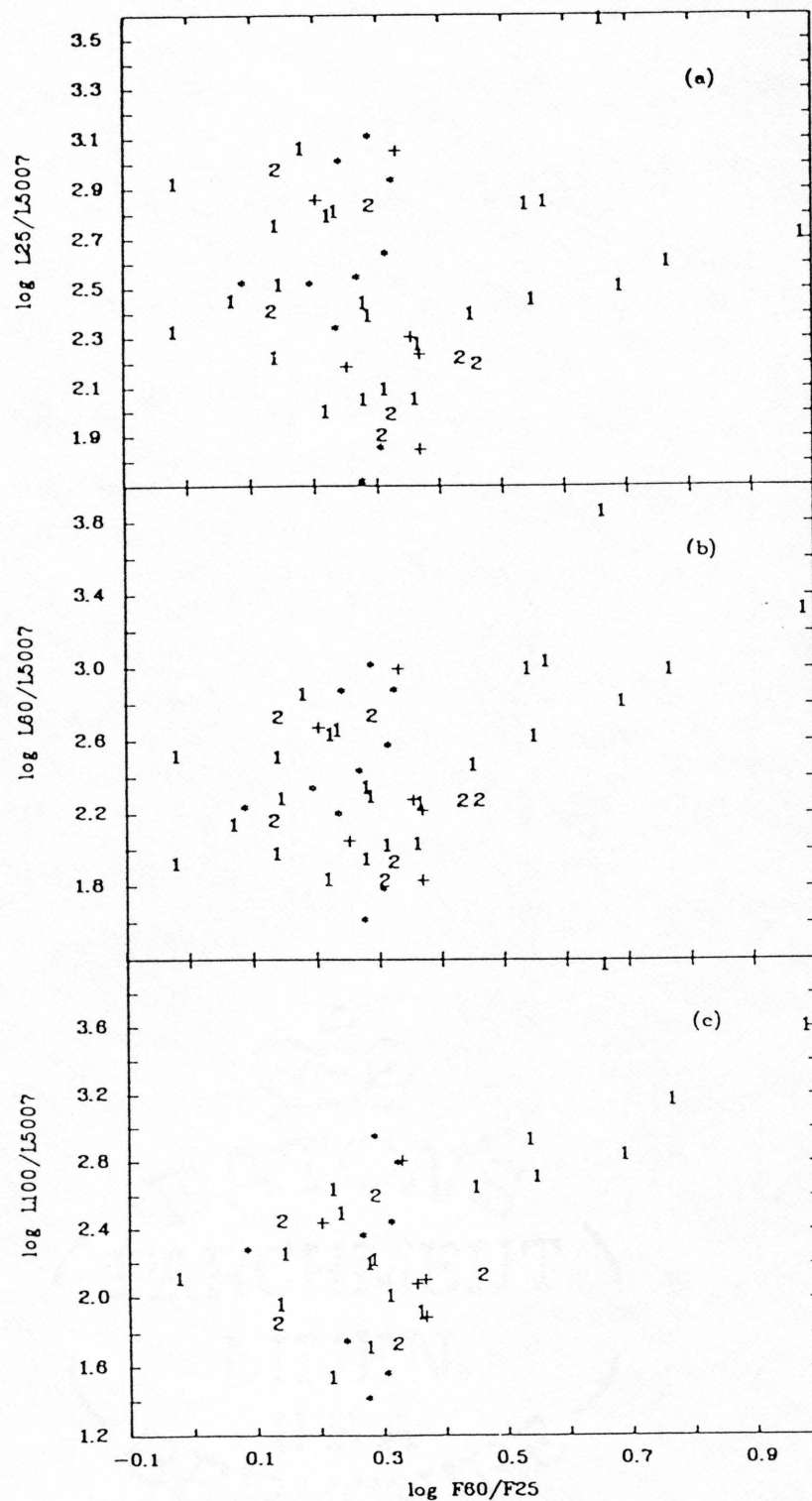
EMR have reached a similar conclusion regarding the far infrared spectrum of cold Seyferts using an independent method of investigation. These authors demonstrated a correlation between the ratio of 11 μm flux in an 8" aperture to the 11 μm flux of the entire galaxy and $\alpha_{12,60}$. (The correlation holds for $\alpha_{25,60}$ as well). The correlation cannot arise from variations in the physical size of a single source, as it would be washed out by the large range of distances (and hence angular sizes) in the data. Thus it can only be modelled using two sources: one much smaller and the other much larger than the 8" aperture.

Ward et al. (1987) studied an X-ray selected sample of mostly type 1 Seyferts, and they also concluded that those with steeply rising far infrared spectra were dominated at these wavelengths by emission from the host galaxy. These authors also showed the cold objects to have

significantly lower X-ray luminosities, which is consistent with the idea that the cold objects are those whose Seyfert nuclei are less luminous relative to the host galaxies.

We interpret the absence of a correlation between $\log F_{25}/F_{60}$ and $\log F_{25}/F_{5007}$ as an indication that, whereas a significant portion of the 60 μm flux in the cold Seyferts arises in the disk of the host galaxy, the 25 μm flux is dominated by the Seyfert nucleus. To be consistent with the results of Ward et al. (1987) this demands that the cold objects have lower 25 μm luminosities. This is indeed the case. The average $\log L_{25}$ (in $\text{erg s}^{-1} \text{Hz}^{-1}$ assuming a Hubble constant of $75 \text{ km s}^{-1} \text{Mpc}^{-1}$) of the cold and warm galaxies in the CfA Seyfert galaxy sample is 30.4 ± 0.2 and 30.8 ± 0.2 . That of the IRAS discovered warm Seyferts is 31.0 ± 0.1 . As expected, there is no significant difference between the two samples of warm objects; but a Student's t-test shows the difference between the cold and warm Seyferts to be greater than 99% significant.

Figure 2-2
25/60 Micron Color vs. IR/Optical Flux Ratio



B. Optical Emission Line Ratios

BPT have developed an empirical system for classifying the optical emission line spectra of galaxies based on several emission line flux ratios. It is instructive to compare the properties of IRAS-discovered warm Seyferts, pre-IRAS warm Seyferts, and cold Seyferts using this system.

Figure 2-3 is a plot of the $\lambda 3727/\lambda 5007$ emission line flux ratio against the $\lambda 5007/H\beta$ flux ratio for seven IRAS-discovered type 2 Seyferts (shown as asterisks in the figure), for which the relevant data were available from C84 or this work. The locus of H II regions in this diagram, taken from BPT, is indicated in the figure. The type 2 Seyferts studied by Koski (1978) have been plotted for comparison with the IRAS-discovered Seyferts. All of the emission line ratios are referred to apertures narrower than 5" and thus to the central ~ 2 kpc or less of the galaxy. Warm Seyferts are plotted as W's, cold Seyferts as C's, and ambiguous cases as question marks. Internal reddening corrections have not been applied to the flux ratios plotted in panel (a), while Koski's dereddened flux ratios are plotted in panel (b). Objects in Koski's sample which are not type 2 Seyferts (the last six objects in his Table 1) have not been included in this figure.

The separation of the various classes of objects in Figure 2-3 is striking, even when no corrections for internal reddening are applied to the data, while the reddening corrections seem to reduce the scatter.

The IRAS-discovered Seyferts are separated from the pre-IRAS warm Seyferts in the opposite direction from the cold Seyferts. For the IRAS-discovered Seyferts, the difference in $\lambda 3727/\lambda 5007$ ratios is explainable by a larger average reddening, as found by OdR. An average reddening of ~ 2.9 magnitudes at 4861 \AA would be required to bring their mean $\lambda 3727/\lambda 5007$ ratio into agreement with the average dereddened value of the Koski (1978) warm Seyferts. This amount of reddening is consistent with the average for IRAS-discovered type 2 Seyferts found by OdR. These authors deduced an average E_{B-V} of .8, which implies ~ 2.7 magnitudes of extinction at 4861 \AA . The higher $\lambda 5007/H\beta$ ratio of the IRAS-discovered type 2 Seyferts is easily explained by the fact that Koski's line ratios were computed after subtraction of an approximately matched absorption line spectrum. The difference can be explained if the $H\beta$ fluxes in the IRAS Seyferts are reduced by $\sim 25\%$ on average due to stellar absorption lines, which is consistent with the appearance of the spectra.

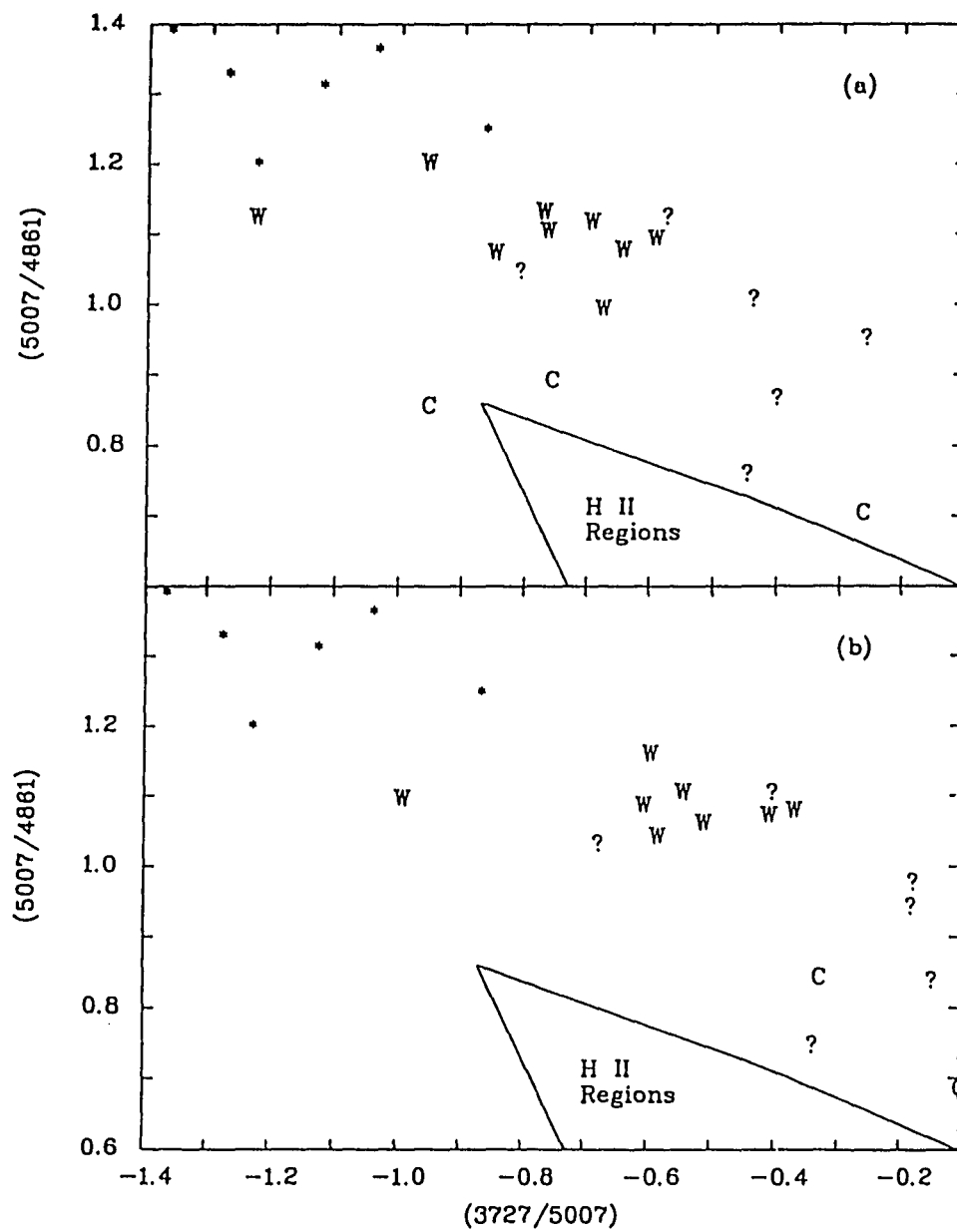
Although there are only three cold type 2 Seyferts in the sample, they appear to be cleanly separated from the warm Seyferts. Furthermore, the Seyferts with ambiguous $25/60 \text{ }\mu\text{m}$ colors are separated from the warm Seyferts in the same sense; and it is reasonable to suppose that most of these are in fact cold objects whose IRAS $25 \text{ }\mu\text{m}$ flux limits are not good enough to exclude the possibility of warm colors.

More emission line flux ratios for cold Seyferts will be needed to confirm their apparent separation from the warm Seyferts in Figure 2-3. However, on the basis of these data, we tentatively conclude that the cold

Seyferts lie between the warm Seyferts and the locus of H II regions in the $\lambda 3727/\lambda 5007-\lambda 5007/H\beta$ diagram. It therefore seems likely that the emission line ratios of the cold Seyferts are significantly contaminated by H II regions in the vicinity of the nucleus.

In conjunction with the results of EMR and of the previous section, this would imply that cold type 2 Seyferts are forming massive stars in regions which include but are not confined to the immediate vicinity of their nuclei. This hypothesis can be verified by using long slit spectroscopy or narrow band $H\alpha$ imaging to extrapolate the contribution of H II regions to the nuclear emission line spectrum. We would predict that Seyferts with higher H II region contributions are those with colder 25/60 μm flux ratios. Furthermore, if H II regions are the main source of 60 μm emission from the host galaxy (which is not unlikely), this technique would allow a determination of the intrinsic 25/60 μm color of the Seyfert nuclei. If our conclusions are correct, the nuclear mid-infrared colors of all Seyferts should closely resemble those of warm Seyferts. Direct verification of this prediction must await mid-infrared imaging.

Figure 2-3
BPT Diagram for IRAS Seyferts



VII. Summary

Optical spectroscopy has now been published on 27 extragalactic IRAS sources satisfying $F_{60}/F_{25} \leq 3$, and 20 have been found to be Seyfert galaxies. The remaining seven have emission line spectra of varying strength, which may be classified as nuclear H II regions, LINERs, or transitions between these classes of spectra. Six of the IRAS-discovered Seyferts are type 1 or composite types, and this fraction is much lower than that found in pre-IRAS warm Seyferts. Seyfert galaxies newly discovered using 25/60 μm color selection are expected to double the size of the sample of known Seyferts detected by IRAS at 25 μm but will not significantly impact the current estimate of the Seyfert galaxy luminosity function (EMR).

It is probable that a majority of Seyfert galaxies do not satisfy the selection criteria discussed here. Previous work (Ward et al. 1987; EMR) has indicated that these "cold" Seyferts are dominated by an extended source in the far infrared. Three of the results reported here support this conclusion. (1) There is no difference between the 25 μm to blue luminosity ratios of cold and warm Seyferts, but the cold Seyferts have significantly higher IR/optical luminosity ratios than the warm Seyferts at 60 μm ; and this trend is stronger at 100 μm . We interpret this as an indication that most Seyferts are dominated by their nuclei at 25 μm but that the cold Seyferts are increasingly dominated by molecular clouds and/or other cold disk emission at longer wavelengths. (2) The cold

Seyferts have lower average 25 μm luminosity, as expected based on this interpretation. (3) Based on a small amount of available data, the nuclear emission line ratios of cold type 2 Seyferts appear to be intermediate between those of warm type 2 Seyferts and H II regions. If confirmed, this result would imply formation of massive stars in the immediate vicinity of the nucleus, and the cold infrared excess might be explainable by giant molecular clouds associated with the star forming activity.

Chapter 3

IR SPECTRAL PROPERTIES OF NORMAL AND ACTIVE GALAXIES:

1. A CATALOG OF INFRARED BRIGHT GALAXIES

Abstract

Total color corrected fluxes at each of the IRAS wavelengths are presented for a sample of 70 isolated galaxies or galaxy mergers selected for brightness integrated over the IRAS spectral range. A variety of other observational data has been assembled from the literature. Infrared selection produces significantly more Seyfert galaxies and galaxies with disturbed or irregular morphology than optical selection from among late type, peculiar, and irregular galaxies. Morphologically disturbed galaxies have axial ratios that are biased toward unity, which explains the axis ratio bias in infrared-selected samples of spiral galaxies. The infrared spectra of objects in our sample can be understood in terms of a two component model similar to that proposed by Helou (1986). The infrared spectral characteristics of the two components are quite distinct: the quiescent component exhibits a small range of colors which are uncorrelated with infrared luminosity, while the other, active component is characterized by two parameters, one of which determines its IR spectral shape and the other its IR luminosity. The ratio of active to quiescent contributions is highest in the IRAS 25 μ m band. The active IR component is very frequently associated with a Seyfert nucleus and/or peculiar morphology. The similar IR spectral characteristics of Seyfert

and peculiar galaxies may be due to a common phenomenology involving infall of gas and dust onto a compact nuclear source of UV and optical radiation.

I. Introduction

Several lines of evidence emerging from the Infrared Astronomical Satellite (IRAS) All Sky Survey point to a change in the nature of extragalactic sources above an infrared luminosity of about $10^{10} L_{\odot}$. Below this luminosity, the infrared to blue luminosity ratio of galaxies, $L_{\text{IR}}/L_{\text{B}}^1$, is fairly constant at about 0.6 (Rieke and Lebofsky 1986), while above it $L_{\text{IR}}/L_{\text{B}}$ is linearly correlated with L_{IR} over two orders of magnitude (Soifer et al. 1987). This behavior is most easily explained on the hypothesis that galaxies with L_{IR} less than $\sim 10^{10} L_{\odot}$ are powered predominantly by star formation and by early type stars both in the blue and in the infrared, while the more IR-luminous galaxies possess an IR power source which contributes relatively little to their optical luminosity. The critical IR luminosity, $L_{\text{C}} \sim 10^{10} L_{\odot}$, beyond which only these super-luminous, high IR/B sources appear, is a natural consequence of the observed sizes of disk systems and limits on their star formation rate and luminosity per square parsec. The lower limit to the luminosity of either type of source is not known.

Another result which points in the same direction is the correlation of the 60/100 μm flux ratio, F_{60}/F_{100} with infrared luminosity (de Jong

¹ See Section V.

et al. 1984; Rieke and Lebofsky 1986; Miley, Neugebauer, and Soifer 1985; Soifer et al. 1987), which is seen in Seyfert as well as normal galaxies. This relationship, like the $L_{\text{IR}}/L_{\text{B}}-L_{\text{IR}}$ relation, is essentially nonexistent below $L_{\text{IR}} \sim 10^{10} L_{\odot}$ but becomes progressively more pronounced with decreasing scatter toward higher luminosities.

A few galaxies exist with infrared luminosities measured by IRAS which equal or exceed typical quasar luminosities. Sanders, Soifer, and Neugebauer (1988) have observationally studied a sample of such objects and found them to be homogeneous in their properties. Optical, infrared, and radio observations of these objects show (1) highly disturbed optical morphologies, (2) bright nuclear emission lines reddened by dust, (3) massive concentrations of molecular material toward their nuclei, (4) large $10 \mu\text{m}$ and $20 \mu\text{m}$ luminosities concentrated in a small central region. Sanders et al. have suggested that these super-luminous "far-infrared galaxies" may all be powered by a quasar/Seyfert nucleus seen through a thick dust shell. Both the dust shell and the active nucleus are the hypothesized result of a galaxy merger, which causes dissipation of angular momentum and settling of large amounts of dust and gas toward the nucleus of the merger product. The Sanders et al. hypothesis raises some interesting questions. Are the far-infrared galaxies fundamentally different from other IR-luminous galaxies, or are they merely extreme examples of a phenomenon which is more widespread? How many causes are there for the infrared excesses seen in late type galaxies, and how may we distinguish between them?

The purpose of this chapter and the next is to further our understanding of IR-luminous galaxies, here termed active galaxies, by differentiating their IR spectral characteristics from those of normal or quiescent galaxies and using those characteristics to constrain possible physical models of the phenomena which give rise to their impressive luminosities and infrared excesses.

In Section II we discuss the selection of a sample of infrared bright galaxies, and in Sections III and IV we present a variety of observational data pertaining to these objects. We conclude with a preliminary investigation of the effect of Seyfert activity (the probable or certain presence of a Seyfert nucleus in a galaxy) and morphological peculiarity on the known behavior of galaxies in IR color-color and color-luminosity diagrams and a brief discussion of the influence of galaxy activity--as defined by IR spectral characteristics--on various monochromatic luminosities and on integrated IR luminosity. The next chapter will deal specifically with the issue of nuclear activity (activity confined to a small central region of a galaxy) and its importance in explaining the relationships discussed here.

II. Sample Selection

To explore a wide range of galaxy activity and its effect on the IR spectra of galaxies, it was decided to select an IR-bright sample of galaxies with as little color bias (within the IRAS spectral range) as possible. In this way the full range of IR spectral properties will be

sampled in a more unbiased fashion than would be achieved by the use of a monochromatic flux limit.

An approximation to IR flux integrated from 7 μm to 130 μm is

$$F_{\text{IR}} = (24f_1 + 9.1f_2 + 5.9f_3 + 1.4f_4) \times 10^{-11} \text{ erg s}^{-1} \text{ cm}^{-2}, \quad (1)$$

where f_1 , f_2 , f_3 , and f_4 are the IRAS Point Source Catalog (version 2; Beichman et al. 1985b, hereafter PSC) fluxes at 12 μm , 25 μm , 60 μm , and 100 μm respectively. This formula was derived by approximating the IRAS filters as rectangular transfer functions with the wavelength boundaries given in Table 3-1. The somewhat arbitrary nature of the assumed wavelength boundaries is unimportant, as any similar scheme gives rise to a flux estimate which, for all practical purposes, is the same.

Table 3-1
Assumed Wavelength Boundaries of IRAS Filters

Band	$\lambda(\text{center})$	$\lambda(\text{left})$	$\lambda(\text{right})$
1	12 μm	7 μm	16 μm
2	25 μm	16 μm	31 μm
3	60 μm	31 μm	80 μm
4	100 μm	80 μm	130 μm

We have selected a sample of galaxies using the following six criteria:

1. Galactic latitude, $|b| > 20^\circ$; and $-20^\circ \leq \delta \leq +70^\circ$. The northern declination limit was chosen to ensure that the objects were observable using the Steward 61" telescope. After elimination of

regions of the sky not covered by the IRAS survey, the total solid angle covered by our sample is 5.93 sr.

2. It was required that the IRAS flux, $f_3 > f_1$, whether or not the fluxes involved were upper limits. This has the effect of eliminating most Galactic objects but does not eliminate any galaxies from the sample. Even galaxies with upper flux limits at 12 μm were not selected against in this way, since the flux limit used to select the sample was bright enough to ensure that the lowest lower limit on f_3/f_1 of objects in our sample was well above the cutoff value of unity (it was 20).
3. A flux limit $F_{\text{IR}} \geq 1.2 \times 10^{-9} \text{ erg s}^{-1} \text{ cm}^{-2}$ was imposed. For objects which were not completely detected by IRAS, the upper limit on F_{IR} was computed and used to make the selection. The value of the flux limit was chosen to ensure a very high detection rate in all IRAS bands and a sample size of ~ 100 objects. Eight objects in the sample were undetected in the PSC at 12 μm , and two were undetected at 25 μm , while all were detected at 60 μm and 100 μm . Except for two objects not detected at 12 μm , all of the objects which were undetected in the PSC were subsequently detected using one-dimensional coadds of IRAS survey data at IPAC; thus the sample is essentially 100% detected in all four IRAS bands.
4. Objects with PSC associations, all of which were with known galactic sources, were eliminated. Remaining objects were kept in the sample, provided that they were associated only with a known

extragalactic object, or that inspection of the Palomar Observatory Sky Survey Plates (POSS) revealed a galaxy within the IRAS error ellipse. All objects which met the latter test were, in fact, associated with a known extragalactic object.

5. Galaxies with optical 25th magnitude per square arcsecond isophotal diameters greater than 8', which have been studied by Rice et al. (1988), were eliminated, since they are well resolved by IRAS, making the methods used here inappropriate for studying them (and also producing a strong bias against them in our sample). This criterion resulted in the elimination of sixteen objects from the sample. The bias in our sample caused by resolution effects will be discussed further below.
6. Sources with close companions of appreciable size or brightness were eliminated, due to potential confusion. The IRAS detectors are 5'.05x3'.03 at 100 μ m, and the 60 μ m detectors are 4'.75 wide. Thus sources with companions within 3 to 5' are potentially confused. These sources were eliminated in the following manner. For objects north of -02° , the Uppsala General Catalog (Nilson 1973; hereafter UGC) was searched for all companions within 5'. If any were found, the source was discarded if the companion was within 2.5 magnitudes at B and if its distance from the IRAS source less half its major axis diameter was less than 3'. An identical test was performed for objects south of -02° by making measurements on the POSS Plates. Eight objects were eliminated in this way, while three objects with

UGC companions within 5' were kept in the sample. Note that systems which are actually in contact or are in the process of merging were not eliminated from the sample, provided they could meet the other criteria.

These selection criteria are met by 70 objects, which are listed in Table 3-2 along with their coordinates, as given in the IRAS PSC. We refer to them below as the Infrared Bright Galaxy Sample (IBGS). Those with Galactic latitude $|b| > 30^\circ$ are all in the Soifer et al. (1987) Bright Galaxy Sample.

Because our sample was selected using PSC fluxes, it is biased against galaxies with large angular diameters and extended infrared emission. The bias increases toward shorter wavelengths. The IBGS by itself is therefore not suitable for estimating the space density of IR bright galaxies. However, this bias against extended sources will not affect any of our conclusions regarding the subset of these galaxies with L_{IR} appreciably greater than $10^{10} L_\odot$, since such galaxies rarely have angular diameters in excess of 4'. Furthermore, the only effect this bias has is that of excluding nearby objects from the sample, as the flux estimates we shall use are not biased against extended emission (see below).

Table 3-2
The Infrared Bright Galaxy Sample

Name	α (1950)	δ (1950)	Other Designation
NGC 34	00 08 33.3	-12 23 10	Mkn 938
NGC 157	00 32 13.8	-08 40 23	
ESO 541-IG23	01 05 18.1	-17 46 36	VV 114
NGC 520	01 21 59.6	+03 31 52	Arp 157
NGC 828	02 07 06.8	+38 57 18	
NGC 972	02 31 16.6	+29 05 35	
NGC 1022	02 36 04.7	-06 53 30	
NGC 1055	02 39 11.7	+00 13 52	
NGC 1068	02 40 07.2	-00 13 30	Arp 37
NGC 1084	02 43 32.3	-07 47 12	
NGC 1222	03 06 24.1	-03 08 48	Mkn 603
NGC 1614	04 31 35.8	-08 40 57	Mkn 617
NGC 2623	08 35 25.2	+25 55 49	Arp 243
NGC 2964	09 39 55.7	+32 04 36	Mkn 404
NGC 3079	09 58 35.0	+55 55 17	
UGC 5390	09 58 41.9	+16 00 43	
NGC 3077	09 59 17.1	+68 58 38	
NGC 3310	10 35 39.6	+53 45 49	Arp 217
NGC 3351	10 41 18.9	+11 58 02	
NGC 3437	10 49 52.8	+23 12 04	
NGC 3504	11 00 28.5	+28 14 27	
NGC 3593	11 11 59.7	+13 05 27	
NGC 3683	11 24 42.8	+57 09 09	
NGC 3810	11 38 23.9	+11 44 53	
NGC 3893	11 46 00.1	+48 59 19	
NGC 3949	11 51 05.1	+48 08 15	
NGC 4027	11 56 56.8	-18 59 14	Arp 22
NGC 4030	11 57 49.4	-00 49 16	
NGC 4038	11 59 19.6	-18 35 53	Arp 244
NGC 4041	11 59 38.8	+62 24 53	
NGC 4088	12 03 01.7	+50 49 07	Arp 18
NGC 4102	12 03 50.8	+52 59 21	
NGC 4157	12 08 34.4	+50 45 39	
NGC 4194	12 11 41.3	+54 48 10	Arp 160, Mkn 201
NGC 4214	12 13 09.3	+36 36 02	
NGC 4254	12 16 17.2	+14 41 38	
NGC 4303	12 19 24.1	+04 44 52	
NGC 4321	12 20 24.7	+16 05 44	
NGC 4388	12 23 14.4	+12 56 23	
NGC 4414	12 23 57.8	+31 29 58	

Table 3-2
(continued)

Name	α (1950)	δ (1950)	Other Designation
NGC 4418	12 24 22.1	-00 36 14	
NGC 4433	12 25 04.7	-08 00 13	
NGC 4501	12 29 28.2	+14 41 28	
NGC 4527	12 31 34.9	+02 55 47	
NGC 4536	12 31 52.7	+02 27 57	
NGC 4605	12 37 48.6	+61 52 50	
NGC 4654	12 41 25.3	+13 24 08	
NGC 4666	12 42 34.6	-00 11 21	
NGC 4691	12 45 38.7	-03 03 36	
NGC 4793	12 52 15.8	+29 12 37	
Mkn 231	12 54 04.7	+57 08 39	
NGC 4818	12 54 12.8	-08 15 19	
NGC 4984	13 06 17.9	-15 14 58	
NGC 5005	13 08 37.8	+37 19 28	
IC 860	13 12 40.1	+24 52 52	MCG+04-31-015
NGC 5054	13 14 17.9	-16 22 14	
IC 883	13 18 19.1	+34 23 49	Arp 193, I Zw 56
NGC 5248	13 35 02.6	+09 08 27	
Mkn 273	13 42 51.6	+56 08 14	
NGC 5506	14 10 38.9	-02 58 28	
NGC 5653	14 28 00.2	+31 26 17	
NGC 5676	14 31 01.2	+49 40 38	
NGC 5713	14 37 37.1	-00 04 34	VIII Zw 447
NGC 5775	14 51 26.8	+03 44 38	
ZG 1510+07	15 10 45.7	+07 24 42	
IC 4553	15 32 46.3	+23 40 10	Arp 220
NGC 6240	16 50 27.7	+02 28 58	
NGC 7469	23 00 44.6	+08 36 18	Arp 298
NGC 7479	23 02 26.6	+12 03 09	
Mkn 331	23 48 52.9	+20 18 20	

III. Basic Observational Properties of the Sample

A. Distances

Recession velocities, associations with galaxy groups and clusters, and distance estimates for IBGS objects are given in Table 3-3. The

heliocentric velocities in column 2 are from Soifer et al. (1987) where available. Others were obtained from Palumbo, Tanzella-Nitti, and Vettolani (1983; hereafter RVG) by a method similar to that of Soifer et al. Radio HI velocities were preferred. If available HI velocities were discrepant, those which were in agreement with the optical velocity with lowest quoted error were averaged. If no HI velocities were available, optical velocities with quoted errors within 10 km/s of the lowest error were averaged. This procedure was used in preference to a weighted mean, since velocities and error estimates in the RVG are of highly nonuniform quality (as noted therein). The procedure adopted reflects our feeling that HI velocities are most reliable, provided they refer to the correct source, while high dispersion optical work is preferable to estimates from low dispersion spectra (which will normally have much larger quoted errors than the former). Velocities obtained in this manner are indicated by "RVG" in column 3.

Associations with groups and clusters of galaxies are given in column 4 of Table 3-3. Group association was determined from the Huchra and Geller (1982) catalog, which tabulates members of quantitatively defined density enhancements in three-dimensional space and is complete to a Zwicky magnitude of ~ 13.5 . The association of NGC 4214 with the Uma group seems doubtful based on a large position and velocity error; it appears in parentheses in Table 3-3 and was not used in making the distance determination. An additional search for positional coincidences with nearby clusters of galaxies was made using search radii and velocity

ranges from Aaronson et al. (1986) and Tifft (1978). This search yielded good agreement on Virgo associations and no new group/cluster associations. Overall, roughly 1/2 of the galaxies in our sample were found to lie in Huchra/Geller groups, compared to 61% of galaxies with $m_Z < 13.5$. This tends to confirm the absence of significant differences in IR properties of galaxies in and out of clusters found by Devereaux, Becklin, and Scoville (1987).

Distance estimates based on an assumed Hubble constant of $75 \text{ km s}^{-1} \text{ Mpc}^{-1}$ are given in column 6 of Table 3-3. They have been derived as follows. The infrared Fisher-Tully relation (Aaronson et al. 1986) was adjusted to our assumed Hubble constant and applied in ten cases where data were available from Aaronson et al. (1982b). For the remaining objects a Virgocentric recession velocity and a linear Hubble relation was used. The recession velocity used was the mean Virgocentric recession velocity of the group of which the galaxy was a member (Huchra and Geller 1982) or, for field galaxies, the velocity given in column 3 of Table 3-3 corrected for a Galactic rotation speed of 300 km s^{-1} and an infall toward Virgo of 300 km s^{-1} . The latter value and the coordinates of the Virgo cluster were taken from Aaronson et al. (1986). The adopted infall velocity is consistent with two determinations by Aaronson et al. (1986; 1982a) using independent techniques. The derived local supercluster rest-frame recession velocity is given in column 5 of Table 3-3.

Table 3-3
Recession Velocities and Distance Estimates

Name	V_H	Ref	V_{LSC}	Group	D(Mpc)
NGC 34	5931		5723		76.3
NGC 157	1651		1444		19.3
IC 1623	5550		5286		70.5
NGC 520	2261		2086	HG52	28.3
NGC 828	5374	RVG	5392		71.9
NGC 972	1550	RVG	1501		20.0
NGC 1022	1498		1246	HG44	15.5
NGC 1055	1005		787	HG48	14.1
NGC 1068	1125		905	HG48	13.2
NGC 1084	1402		1145	HG44	15.5
NGC 1222	2600		2362		31.5
NGC 1614	4745		4492		59.9
NGC 2623	2157		2244		29.9
NGC 2964	1319		1489	HG64	21.3
NGC 3079	1170	RVG	1430		19.3
NGC 3094	2388		2503		33.4
NGC 3077	12	RVG	295	M81	4.5
NGC 3310	970		1246		16.6
NGC 3351	776		911	Leo	16.1
NGC 3437	1291		1483		19.8
NGC 3504	1549		1769	HG61	22.2
NGC 3593	621		788	Leo	16.1
NGC 3683	1656		1961		26.1
NGC 3810	995	RVG	1177		15.7
NGC 3893	977		1282	UMa	19.1
NGC 3949	804		1110	UMa	19.2
NGC 4027	1677		1716	HG33	22.9
NGC 4030	1463		1600		21.3
NGC 4038	1563		1606	HG33	22.9
NGC 4041	1234		1556	HG82	21.4
NGC 4088	763		1079	UMa	17.0
NGC 4102	863		1182	UMa	17.0
NGC 4157	771		1089	UMa	18.0
NGC 4194	2528		2851		38.0
NGC 4214	288		583	(UMa)	7.8
NGC 4254	2447		2670	Virgo	18.2
NGC 4303	1568		1748	Virgo	18.2
NGC 4321	1576		1807	Virgo	18.2
NGC 4388	2489	RVG	2709	Virgo	18.2
NGC 4414	730	RVG	1017	UMa	18.4
NGC 4418	2045		2202		29.4

Table 3-3
(continued)

Name	V_H	Ref	V_{LSC}	Group	D(Mpc)
NGC 4433	2978		3097		41.3
NGC 4501	2276	RVG	2507	Virgo	17.1
NGC 4527	1737		1916	Virgo	18.2
NGC 4536	1824		2001	Virgo	14.4
NGC 4605	140		475		6.3
NGC 4654	1034	RVG	1267	Virgo	17.0
NGC 4666	1645		1816	Virgo	18.2
NGC 4691	1115	RVG	1273	Virgo	18.2
NGC 4793	2515		2811		37.5
Mkn 231	12556		12896		171.9
NGC 4818	1050		1185	Virgo	18.2
NGC 4984	1259	RVG	1362	Virgo	18.2
NGC 5005	950		1274	HG68	17.1
IC 860	3862		4155		55.4
NGC 5054	1743	RVG	1843		24.6
IC 883	6870		7192		95.9
NGC 5248	1156		1399		18.7
Mkn 273	11400		11753		156.7
NGC 5506	1809		2006		26.7
NGC 5653	3514		3850		51.3
NGC 5676	2104		2465	HG73	31.3
NGC 5713	1900		2118	HG49	25.1
NGC 5775	1670		1909	HG50	26.3
ZG1510+07	3528		3786		50.5
IC 4553	5452		5772		77.0
NGC 6240	7299	RVG	7517		100.2
NGC 7469	4963		4913		65.5
NGC 7479	2382		2349		31.3
Mkn 331	5385		5359		71.5

Table 3-4
Observational Properties
of the Infrared Bright Galaxy Sample

Name	AGN	t	log D ₂₅	log R ₂₅	B _T	Ref	B _{0T}
NGC 34	2	-15	0.71	0.00	12.83	iffc	12.86
NGC 157		4	1.63	0.17	11.03		10.88
IC 1623		-15	1.06	0.10	15.23	hhhc	15.11
NGC 520		-15	1.68	0.35	12.05		11.54
NGC 828		-1	1.50	0.10	12.83	aaac	12.68
NGC 972		0	1.56	0.26	12.10		11.89
NGC 1022		1	1.40	0.08	12.20		12.12
NGC 1055		3	1.88	0.40	11.40		11.07
NGC 1068	2	3	1.84	0.07	9.51		9.45
NGC 1084		5	1.46	0.27	11.23		11.00
NGC 1222		-0.5	1.21	0.21	13.52	deee	13.33
NGC 1614		-5	1.12	0.06	13.60		13.53
NGC 2623		-15	0.79	0.08	14.40		14.29
NGC 2964		4	1.47	0.24	12.05		11.85
NGC 3079	2	5	1.88	0.65	11.20		10.67
NGC 3094		1	1.16	0.22	13.31	gggc	13.11
NGC 3077		0	1.66	0.10	10.65		10.58
NGC 3310		-4	1.56	0.09	11.20		11.12
NGC 3351		3	1.87	0.16	10.50		10.37
NGC 3437		5	1.41	0.44	12.64	aaac	12.28
NGC 3504		2	1.43	0.09	11.80		11.71
NGC 3593		1	1.76	0.37	11.70	aaab	11.40
NGC 3683		5	1.30	0.37	12.97	aaac	12.67
NGC 3810		5	1.63	0.14	11.25		11.13
NGC 3893		5	1.64	0.19	11.10		10.94
NGC 3949		4	1.47	0.21	11.60		11.43
NGC 4027		8	1.47	0.10	11.65		11.57
NGC 4030		4	1.63	0.12	11.56	aaac	11.45
NGC 4038		-9	1.41	0.16	11.30		11.15
NGC 4041		4	1.45	0.02	11.70		11.68
NGC 4088		4	1.76	0.36	11.10		10.81
NGC 4102		3	1.50	0.21	12.30		12.13
NGC 4157		3	1.84	0.62	11.67	aaac	11.17
NGC 4194		-10	1.39	0.17	12.95		12.78
NGC 4214		10	1.90	0.10	10.20		10.10
NGC 4254		5	1.73	0.05	10.43		10.37
NGC 4303	3	4	1.78	0.04	10.22		10.17
NGC 4321		4	1.84	0.05	10.11		10.05
NGC 4388	2	3	1.71	0.56	11.83		11.36
NGC 4414		5	1.56	0.22	10.95		10.77

Table 3-4
(continued)

Name	AGN	t	log D ₂₅	log R ₂₅	B _T	Ref	B _{0T}
NGC 4418	3	1	1.16	0.27	13.76	gggc	13.52
NGC 4433		2	1.36	0.32	12.92	aaac	12.63
NGC 4501	2	3	1.84	0.25	10.28		10.06
NGC 4527		4	1.80	0.44	11.31		10.94
NGC 4536		4	1.87	0.33	11.00		10.72
NGC 4605		-5	1.74	0.38	10.97		10.66
NGC 4654		6	1.67	0.20	11.10		10.98
NGC 4666		5	1.65	0.47	11.55		11.16
NGC 4691		-0.5	1.51	0.08	11.70		11.63
NGC 4793		5	1.46	0.24	12.30		12.09
Mkn 231	1	-5	1.24	0.17	14.30		14.09
NGC 4818		2	1.65	0.41	11.88	aaac	11.54
NGC 4984		0.5	1.44	0.10	11.71	aaab	11.62
NGC 5005	2	4	1.73	0.30	10.65		10.40
IC 860		3	0.80	0.20	14.56	iffc	14.37
NGC 5054		4	1.70	0.21	11.51	aaab	11.33
IC 883		-15	1.24	0.14	14.56	gggc	14.39
NGC 5248		4	1.81	0.12	10.80		10.70
Mkn 273	2	-15	1.11	0.57	14.80		14.00
NGC 5506	2	-1	1.46	0.45	13.19	aaac	12.81
NGC 5653		3	1.26	0.07	12.90		12.82
NGC 5676		4	1.59	0.28	11.60		11.36
NGC 5713		-4	1.45	0.05	12.00		11.95
NGC 5775		5	1.63	0.55	12.24		11.79
ZG 1510+07		0	0.71	0.27	15.00	iffc	14.75
IC 4553	2	-15	1.31	0.04	14.17	gggc	14.14
NGC 6240		0	1.34	0.28	11.90	aaab	11.59
NGC 7469	1	1	1.25	0.13	12.60		12.43
NGC 7479	3	5	1.61	0.10	11.70		11.61
Mkn 331		1	0.93	0.17	14.65	aaac	14.45

Source References for Table 3-4

The source of the information in columns 3-6 is indicated by four letters in column 7. If no letters are present, all information is from the RC2. This is true for 69% of the objects. Other sources are as follows:

- a. RC2: not specified unless other entries for this object utilize non-RC2 data.
- b. Revised Shapley Ames Catalog (Sandage and Tamman 1981) B_T magnitude derived from references given therein.

c. Either (1) Harvard magnitude corrected to RC2 system as listed in the RC2; (2) Zwicky magnitude corrected to RC2 system as recommended by Kirshner, Oemler, and Schechter (1978); or (3) the average of (1) and (2) if both are available. Agreement between "corrected" m_H and m_Z is not good ($\sim \pm 0.6$ mag), and these values should be considered highly uncertain.

d. My own estimate of Hubble type based on a V CCD frame with $2' \times 2'$ field and $0''.3$ pixels. A Bulge/disk decomposition performed on the same frame yielded a bulge/disk ratio typical of this morphological type (Kent 1985).

e. My own measurement of D_{25} , R_{25} , and B_{25} by elliptical isophote fitting performed on a V CCD frame with $2' \times 2'$ field and $0''.3$ pixels. The average $B-V$ color for the morphological type (Mihalic and Binney 1981) was assumed, and the ellipse parameters were extrapolated a short distance where necessary. Errors are less than ± 0.02 in all three quantities.

f. My own measurement of D_{xd} on the POSS made using a $10\times$ reticle with 0.1 mm markings and reduced to the RC2 scale in the same manner as specified in the RC2 for UGC diameters.

g. UGC morphology and diameters reduced to RC2 scale as specified in the RC2.

h. ESO catalog (Lauberts 1982) morphology and diameters reduced to RC2 scale as specified in the ESO catalog.

i. My own estimate of morphological type from POSS prints. Highly uncertain and indicative only of early/late, peculiar or not. These estimates have been checked for consistency with MCG and RNGC descriptions of the object wherever possible.

B. Optical Properties

Table 3-4 summarizes some of the important optical properties of galaxies in the IBGS. The presence of a Seyfert nucleus is indicated in column 2. The data are taken from Véron-Cetty and Véron (1987) and Edelson, Malkan, and Rieke (1987). In the table the numbers 1 and 2

indicate type 1 and 2 Seyferts respectively, and 3 indicates a possible or probable Seyfert according to Véron-Cetty and Véron.

Column 3 of Table 3-4 contains a modified Hubble type parameter, t , which is similar to the parameter T given in the Second Reference Catalog of Bright Galaxies (de Vaucouleurs, de Vaucouleurs, and Corwin 1975; hereafter RC2). Because the IBGS contains no galaxies earlier than S0 ($T=-1$), we have used negative values of the modified Hubble type parameter, t , to indicate morphological peculiarities and assigned a value of 0.5 to Hubble types S0 and S0/a. Thus a galaxy classified as Sap would have an RC2 T value of 1 and $t=-1$. The relationship between RC2 Revised Hubble Types, RC2 T values, and our parameter t is given explicitly in Table 3-5. The sample is completely classified with 87% of the classifications from a single source (RC2). The source of the morphological classifications (as well as other information in Table 3-4) is indicated in column 7 of Table 3-4.

Table 3-5
The Modified Hubble Type Parameter (t)

RC2 Revised Hubble Type	RC2 T	t
Pec.	...	-15
IrrI/IrrIp	10	10/-10
IrrII/IrrIIp	0	0
S0/S0p	-1	.5/-.5
S0a/S0ap	0	1/-1
Sab/Sabp	2	2/-2
Sb/Sbp	3	3/-3
Sbc/Sbcp	4	4/-4
Sc/Scp	5	5/-5
S/Sp	5	5/-5

The isophotal diameter, isophotal axial ratio, and integrated magnitude, in the B photometric band are listed in columns 4-6 of Table 3-4. Optical diameters are referred to the 25th magnitude B isophote and are given in units of 0.1 as in the RC2. The information in Table 3-4 is taken directly from the RC2 unless otherwise noted in column 7. Complete information has been obtained for all objects and reduced to the RC2 system using the sources given in the notes to Table 3-4, but the quality of the data is necessarily nonuniform. Complete RC2 information was available for 39% of the sample. The total B magnitude, corrected for inclination and redshift, B_{0T} , was computed as recommended in the RC2 and is given in column 8 of Table 3-4. The inclination correction applied to objects classified only as "peculiar" ($t=-15$) was $1.5 \times \log R_{25}$ mag. These estimates of total B magnitude are intended only to give a rough indication of the IR/B luminosity ratio with a minimal amount of inclination and redshift bias.

C. Comparison to a Control Sample

The incidence of nuclear activity and peculiarity and the axial ratio distribution of the IBGS must be compared to a sample of objects which are comparably well studied in the optical, since we have defined these properties using the results of optical studies. To gain further physical insight from the comparison, it is useful to control for incidental properties, other than infrared brightness, of objects in the IBGS sample, which could affect our results. The most obvious properties of our sample which could produce secondary biases are the absence of elliptical galaxies from the sample, the inclusion of 12 members of the Virgo cluster, and the angular diameter limit. Accordingly, we have selected a control sample with similar features.

The control sample was selected from the RC2. To facilitate the comparison, the objects were required to have entries for Revised Type, D_{25} , and R_{25} (most RC2 galaxies do). All objects selected were required to have a morphological type of peculiar, IrrII, or S0/a or later. The requirement $D_{25} < 8'$ was also imposed on the control sample. Six objects were selected from near the beginning of each hour of right ascension between 06^h and 15^h with the last three of each six required to have RC2 entries for B_T . Page boundaries in the RC2 were used to randomize the selection process: galaxies were chosen from the top of the first page whereon the first galaxy's right ascension exceeded the hour boundary. Additional objects were taken from near 12^h30^m to produce a suitable

concentration of galaxies near Virgo. This was done by taking six galaxies from the first page beginning after $12^{\text{h}}30^{\text{m}}$ and six from the top of the previous page in the manner just described. All galaxies in between these two sets of six having an entry under B_T (and satisfying the other criteria as well) were also added to the sample. This produced a sample of 80 galaxies with complete morphological type, diameter, and axial ratio information. Values of B_T were available in the RC2 for 59% of the control sample, compared with 69% of the IBGS. Active galactic nuclei and Virgo cluster members among the control sample were then identified in the same way as for the IBGS. These data are given in Table 3-6. The control sample contains 12 Virgo cluster members.

The mean optical properties of the IBGS and the control sample are compared in Table 3-7. The comparison is not perfect, since the mean optical diameter of the control sample is 30% below the IBGS value. Nonetheless we consider it highly significant that the incidence of Seyfert activity and peculiar morphology is much higher in the infrared bright sample. By summing over the tail of a binomial distribution, one can show that the chance of obtaining the same fraction or a higher fraction of Seyferts as found in the IBGS from a parent population containing the fraction of Seyferts found in the control sample is 0.01%. The corresponding probability for the incidence of peculiarity in the IBGS is 0.003%. Although galaxies with extremely bright stellar nuclei are sometimes classified as peculiar, this does not explain the high incidence of peculiarity in the IBGS. When possible, probable, or known Seyferts

are excluded, the remaining IBGS galaxies are still $30.4\% \pm 7.4\%$ peculiar, which is significantly (0.03% level of rejection) above the control sample proportion. This result clearly demonstrates the importance of nuclear activity and disturbed morphologies in generating far-infrared luminosity and the value of far-infrared observations for studying these phenomena.

The high incidence of disturbed morphology in the IBGS supports the conclusion of Armus, Heckman, and Miley (1987; here after AHM87) that the bias against large axial ratios seen by these authors and Burstein and Lebofsky (1986) in IR-selected samples is due to morphological disturbances, which give rise to less flattened intrinsic shapes. We attribute the nearly identical distribution of $\log R_{25}$ in the IBGS and control sample to the brightness of our flux limit, which causes many nearby, normal galaxies to be included in our sample, and to the bias against edge-on objects present in our control sample. Comparing the axial ratios of the peculiar and non-peculiar objects lends further support to this conclusion. For the 22 IBGS objects with $t \leq 0$, $\langle \log R_{25} \rangle = 0.19 \pm 0.03$, while that of the remaining 48 is 0.24 ± 0.02 . The average $\log R_{25}$ of the non-peculiar control objects is 0.19 ± 0.02 . The difference between the IR-selected peculiar and non-peculiar objects is at only the 84% confidence level but tends to confirm the AHM87 hypothesis, since objects in our IR-selected sample which various authors have independently classified as morphologically peculiar have axial ratios closer to unity than those which have not been so classified. Also, the non-peculiar IR-selected objects have larger axial ratios than

their optically selected counterparts (also at the 84% confidence level), as one would expect from a dusty disk which is optically thin in the infrared.

Table 3-6
Control Sample of RC2 Galaxies

Name	AGN	t	log D ₂₅	log R ₂₅	B _T	B _{0T}	Virgo
A0526-16		6	1.26	0.00			
A0527+73		10	1.36	0.00			
N1954		5	1.61	0.24			
N1964		3	1.79	0.39	11.50	11.19	
N1961		5	1.63	0.16	11.90	11.77	
N2139		6	1.34	0.06	12.05	11.55	
N2273	2	0.5	1.55	0.11			
I451		2	1.21	0.07			
N2290		0.5	1.17	0.24			
N2268		4	1.53	0.19	12.20	12.05	
N2339		4	1.44	0.11	12.30	12.21	
N2344		5	1.30	0.01	12.85	12.42	
A0724+40		10	1.20	0.12			
A0727+73		2	1.13	0.73			
A0729+66		9	1.47	0.16			
N2415		9	1.01	0.00	12.82	12.82	
N2427		8	1.75	0.34	12.36	12.09	
N2442		3	1.78	0.04	11.23	10.51	
N2544		0.5	1.03	0.09			
N2566		2	1.49	0.19			
N2565		4	1.28	0.33			
N2578		-0.5	1.38	0.23	13.40	13.24	
N2551		0.5	1.28	0.15	13.05	12.95	
N2598		1	1.11	0.39	14.70		
A0911+16		2	1.33	0.00			
A0911+47		5	1.08	0.25			
A0913+74		5	1.17	0.26			
N2811		1	1.43	0.41	12.25	11.92	
N2798		-1	1.44	0.38	13.00	12.70	
N2805		7	1.80	0.10	11.78	11.40	
N3166		0.5	1.72	0.29	11.50	11.30	
N3144		-1	1.15	0.19			
N3169	3	-1	1.68	0.18	11.25	11.11	
N3175		1	1.68	0.45	12.20	11.84	
N3147		4	1.60	0.05	11.45	11.41	
N3177		3	1.22	0.09	13.00	12.72	
A1109+51		5	0.61	0.42			
A1110+53		9	1.28	0.05			
N3557		1	1.23	0.01			
N3593		0.5	1.76	0.37	11.70	11.44	
N3611		-1	1.38	0.07	12.80	12.74	

Table 3-6
(continued)

Name	AGN	t	log D ₂₅	log R ₂₅	B _T	B _{0T}	Virgo
N3623		1	2.00	0.48	10.17	9.59	
N4108		5	1.28	0.07			
N4109		1	0.92	0.06			
A1204+17		3	0.83	0.00			
N4116		8	1.58	0.20	12.40	12.24	
N4123		5	1.65	0.11	11.85	11.76	
N4129		2	1.41	0.52	13.20		
N4492		1	1.31	0.03	13.20	12.95	
N4487		6	1.61	0.13			Virgo
I3453		8	1.09	0.47			
N4501	2	3	1.84	0.25	10.28	9.86	Virgo
I3483		-3	0.67	0.10	15.80	15.52	
N4519		7	1.49	0.14	12.36	12.03	Virgo
N4527		4	1.80	0.44	11.31	10.73	Virgo
N4532		10	1.46	0.36	12.32	11.76	Virgo
N4535		5	1.83	0.13	10.67	10.56	Virgo
N4533		7	1.30	0.67			
N4536		4	1.87	0.33	11.00	10.73	Virgo
N4548		3	1.73	0.09	10.99	10.91	Virgo
N4567		4	1.47	0.15	12.09	11.97	Virgo
N4568		4	1.66	0.33	11.68	11.19	Virgo
I850		5	0.89	0.58			
N4981		4	1.44	0.10			Virgo
N4980		0.5	1.34	0.27			
N4995		3	1.39	0.15	11.90	11.78	Virgo
N5005	2	4	1.73	0.30	10.65	10.41	
A1310+36		10	1.39	0.05	13.60	13.36	
I983		4	1.74	0.05			
N5490C		4	1.03	0.13			
N5492		-3	1.26	0.58			
N5533		2	1.51	0.18	12.65	12.51	
N5548	1	0.5	1.28	0.06	13.15	13.11	
N5560		-3	1.59	0.64	13.20		
N5916A		-5	1.13	0.46			
N5915		-2	1.21	0.13			
N5921		4	1.69	0.07	11.45	11.39	
N5936		3	1.19	0.03	13.00	12.98	
N5962		5	1.45	0.13	12.05	11.95	
N5970		5	1.47	0.15	12.15	11.69	

Table 3-7
Average Optical Properties

		Seyfert	Peculiar	D ₂₅	R ₂₅	B _T
IBGS	mean	20.0%	31.4%	1.49	0.23	12.08
	sigma			0.29	0.16	1.31
	error	5.3%	6.7%	0.03	0.02	0.16
Control	mean	6.3%	12.5%	1.40	0.21	12.22
	sigma			0.28	0.18	1.05
	error	2.8%	4.0%	0.03	0.02	0.16

IV. IRAS Satellite Data

We have obtained high quality color corrected total monochromatic fluxes at the nominal wavelength of each of the four IRAS bands for all objects in the IBGS using one dimensional coadds of IRAS survey data performed at the Infrared Processing and Analysis Center. Great care has been taken to avoid underestimating the shorter wavelength emission from partly resolved galaxies, without which, serious underestimation can occur, as we shall demonstrate. The color corrected total fluxes are given in Table 3-8, and the details of their derivation are discussed below.

Table 3-8
Color Corrected Total IRAS Fluxes for the
Infrared Bright Galaxy Sample

Name	F ₁₂	F ₂₅	F ₆₀	F ₁₀₀	$\alpha_{12,25}$	$\alpha_{25,60}$	$\alpha_{60,100}$
NGC 34	0.38	2.83	17.01	17.86	-2.72	-2.05	-0.09
NGC 157	1.75	3.03	19.83	47.88	-0.75	-2.15	-1.73
IC 1623	1.28	4.48	24.83	33.53	-1.71	-1.96	-0.59
NGC 520	0.99	3.64	34.13	50.45	-1.78	-2.56	-0.77
NGC 828	0.56	0.88	12.75	26.16	-0.62	-3.05	-1.41
NGC 972	2.21	4.33	35.47	67.33	-0.92	-2.40	-1.25
NGC 1022	0.90	4.23	21.10	28.83	-2.11	-1.84	-0.61
NGC 1055	2.29	3.46	23.62	69.49	-0.56	-2.19	-2.11
NGC 1068	45.22	101.97	207.36	262.35	-1.11	-0.81	-0.46
NGC 1084	2.08	3.70	31.53	61.69	-0.79	-2.45	-1.31
NGC 1222	0.68	3.04	13.51	15.78	-2.03	-1.71	-0.30
NGC 1614	1.66	8.79	33.56	35.89	-2.27	-1.53	-0.13
NGC 2623	0.23	1.91	24.61	28.33	-2.88	-2.92	-0.28
NGC 2964	0.86	2.25	12.81	26.54	-1.31	-1.99	-1.43
NGC 3079	2.98	4.46	54.97	109.51	-0.55	-2.87	-1.35
NGC 3094	0.85	3.26	11.64	15.31	-1.84	-1.45	-0.54
NGC 3077	0.87	2.56	14.96	28.26	-1.48	-2.02	-1.25
NGC 3310	1.94	6.35	35.83	48.40	-1.62	-1.98	-0.59
NGC 3351	1.28	3.40	21.32	40.81	-1.33	-2.10	-1.27
NGC 3437	0.89	1.30	12.72	21.66	-0.51	-2.61	-1.04
NGC 3504	1.30	4.95	23.18	36.67	-1.82	-1.76	-0.90
NGC 3593	1.58	2.44	20.51	39.73	-0.59	-2.43	-1.29
NGC 3683	1.01	1.86	14.61	32.42	-0.83	-2.35	-1.56
NGC 3810	1.44	2.18	15.25	41.29	-0.57	-2.22	-1.95
NGC 3893	1.72	2.07	17.39	40.68	-0.25	-2.43	-1.66
NGC 3949	0.95	1.64	12.17	27.56	-0.74	-2.29	-1.60
NGC 4027	0.97	1.54	12.59	30.31	-0.64	-2.40	-1.72
NGC 4030	1.62	2.47	21.98	60.20	-0.58	-2.50	-1.97
NGC 4038	2.68	8.04	52.85	91.86	-1.50	-2.15	-1.08
NGC 4041	1.24	2.01	15.84	35.89	-0.66	-2.36	-1.60
NGC 4088	2.35	4.29	30.37	65.31	-0.82	-2.24	-1.50
NGC 4102	2.09	8.46	48.82	77.38	-1.91	-2.00	-0.90
NGC 4157	2.22	3.15	21.36	56.91	-0.48	-2.19	-1.92
NGC 4194	0.90	5.38	24.16	26.94	-2.43	-1.72	-0.21
NGC 4214	0.62	2.82	19.13	30.85	-2.06	-2.19	-0.94
NGC 4254	4.02	5.49	42.18	105.32	-0.42	-2.33	-1.79
NGC 4303	3.74	6.11	38.40	77.40	-0.67	-2.10	-1.37
NGC 4321	2.51	3.85	26.79	74.56	-0.58	-2.22	-2.00
NGC 4388	1.11	4.31	11.40	19.37	-1.85	-1.11	-1.04
NGC 4414	3.15	4.41	32.49	80.54	-0.46	-2.28	-1.78

Table 3-8
(continued)

Name	F ₁₂	F ₂₅	F ₆₀	F ₁₀₀	$\alpha_{12,25}$	$\alpha_{25,60}$	$\alpha_{60,100}$
NGC 4418	0.77	10.89	39.90	32.27	-3.60	-1.48	0.42
NGC 4433	0.47	2.27	13.78	23.73	-2.14	-2.06	-1.06
NGC 4501	2.19	3.41	18.96	67.50	-0.60	-1.96	-2.49
NGC 4527	2.75	4.69	33.86	72.08	-0.73	-2.26	-1.48
NGC 4536	1.85	5.16	32.87	49.21	-1.39	-2.11	-0.79
NGC 4605	0.86	1.57	15.18	33.20	-0.83	-2.59	-1.53
NGC 4654	1.17	2.61	15.43	42.47	-1.10	-2.03	-1.98
NGC 4666	3.32	4.18	39.37	90.48	-0.31	-2.56	-1.63
NGC 4691	0.95	3.65	15.64	22.90	-1.83	-1.66	-0.75
NGC 4793	0.74	1.87	13.41	29.96	-1.26	-2.25	-1.57
Mkn 231	2.26	9.70	33.21	32.46	-1.99	-1.41	0.04
NGC 4818	0.84	5.08	19.95	27.37	-2.46	-1.56	-0.62
NGC 4984	0.98	1.79	11.68	17.38	-0.82	-2.14	-0.78
NGC 5005	1.86	2.81	23.97	68.49	-0.57	-2.45	-2.06
IC 860	<.20	1.98	17.52	19.29	...	-2.49	-0.19
NGC 5054	1.10	1.97	13.74	30.28	-0.79	-2.22	-1.55
NGC 883	0.31	1.77	14.40	27.38	-2.36	-2.39	-1.26
NGC 5248	2.03	3.33	22.33	57.58	-0.67	-2.17	-1.85
Mkn 273	0.22	2.84	23.24	23.87	-3.48	-2.40	-0.05
NGC 5506	1.32	4.96	8.27	9.39	-1.80	-0.58	-0.25
NGC 5653	0.87	1.76	12.15	22.92	-0.96	-2.20	-1.24
NGC 5676	1.22	1.95	13.38	35.23	-0.64	-2.20	-1.90
NGC 5713	1.46	3.64	22.63	38.92	-1.25	-2.09	-1.06
NGC 5775	2.10	3.39	27.05	57.61	-0.65	-2.37	-1.48
ZG 1510+07	<.20	1.07	22.13	32.83	-3.79	-3.46	-0.77
NGC 4553	0.67	10.43	111.09	126.73	-3.73	-2.70	-0.26
NGC 6240	0.65	4.38	23.34	29.27	-2.59	-1.91	-0.44
NGC 7469	1.44	6.20	28.83	39.27	-1.99	-1.76	-0.61
NGC 7479	1.61	5.03	16.53	28.47	-1.55	-1.36	-1.06
Mkn 331	0.65	3.25	18.39	22.64	-2.18	-1.98	-0.41

A. Processing of IRAS Data

Coadds were performed at source positions given in the PSC. All detector tracks from within 1!7 of the source position were included. The noise in each detector track was estimated from a quadratic fit to the

baseline after exclusion of large deviations. The noise estimates were then used to produce an inverse-variance-weighted mean coadd. For about half the sources an unweighted mean was used, since the weighted mean option was not available when the coadds were performed. In a few cases the median of the coadded data streams was used to avoid spikes or other spurious features in the weighted mean coadd.

Photometry within an aperture of fixed size for each IRAS band was used to estimate flux, since this procedure is less likely than others to introduce a bias based on source size, provided the aperture is large enough. Standard aperture sizes of 4', 4', 5', and 8' were used in bands 1, 2, 3, and 4 respectively, unless emission outside of these limits was visible on any plot of the coadded detector tracks, in which case an appropriately larger aperture was used. After performing the coadd, each of the input detector tracks was inspected for excessive noise levels, radiation hits, asteroid passage, or other serious defects. Defective scans were thrown out, and a new coadd was performed, except when the problems were clearly absent in the median coadd.

Finally, the size of the observed infrared source was used to determine whether the standard cross-scan distance tolerance of 1!7 was adequate to measure all of the flux from the source. In 27 cases, the above procedure was considered to be potentially inadequate for this reason. For these sources the cross-scan tolerance was reduced by an amount determined from the full width at half maximum of the band 1 source, W50(1); and a note to this effect has been entered in Table 3-8.

In seven cases where $W50(1) > 1.5$ the maximum allowable cross-scan distance was reduced to 1.0. These sources are marked with an "a" under Notes in Table 3-8. When $1.5 > W50(1) > 1.0$ the cross-scan tolerance was usually reduced to 1.2. Fifteen sources processed in this way have a "b" under Notes in Table 3-8. Five sources with $1.5 > W50(1) > 1.0$ were processed with the standard 1.7 tolerance and have a "c" under Notes in Table 3-8.

Because the best value for the cross-scan tolerance used to measure an extended source cannot be determined a priori, modelling of the infrared source was used as a check on the values chosen here and to estimate the amount of flux errors resulting from (1) the finite cross-scan width of the IRAS detectors, which is comparable to the source size in these cases; and (2) the inclusion of off-center scans in the average, which exacerbates condition (1). The modelling procedure, which was applied to 27 sources, served to verify that the amount of missing flux is almost always less than 10% with the cross-scan limits chosen here and, further, provided a demonstrably improved flux estimate for a few of these sources.

The source in the IRAS focal plane was modeled by convolving a representation of the intrinsic IR source with a circular gaussian having the same full width at 80% encircled energy as the IRAS optics (Beichman et al. 1985a). The position angle and axis ratio of the intrinsic infrared source was taken to be the same as the optical source. These data were obtained from Table 3-4, from the UGC, and, in a few cases from measurements on the POSS using a 10x reticle with 0.1 mm markings. The

major axis of the intrinsic IR source was determined by requiring the full width at half maximum of the focal plane source to match the value measured on the coadded IRAS data.

The position angle and minimum cross-scan distance (from source center to detector center), z_0 , of each IRAS detector track were then used to compute the fraction of the total source flux measured by that detector. For an elliptical gaussian source model scanned by a detector of width w , one can show that the fraction of the total flux crossing the detector,

$$c = \frac{1}{2} \left\{ \operatorname{erf} \left[\frac{|z_0| + w/2}{\sqrt{2(b^2 \sin^2 \theta + a^2 \cos^2 \theta)}} \right] - \operatorname{erf} \left[\frac{|z_0| - w/2}{\sqrt{2(b^2 \sin^2 \theta + a^2 \cos^2 \theta)}} \right] \right\} \quad (2)$$

where θ is the angle between the major axis of the source and the detector track, and a and b are the semimajor and semiminor axes of the focal plane source.

This computation was performed separately for each detector track used in the coadd, and the average value of c was used to correct the flux. For simplicity, w was set to the mode of the detector size distribution in each band (Beichman et al. 1985a). For sources with $W50(1) > 1.5$ (those with Note a in Table 3-8) the correction factor ranged from 0 to 20% but was less than 4% in all but two cases. For the sources with $1.5 > W50(1) > 1.0$ the correction factor ranged from 0 to 12% and was less than 3% in all but one case. The uncorrected fluxes, full widths at half maximum, source parameters and correction factors are given in Table 3-9.

The validity of this modelling procedure was checked by computing corrected fluxes for the seven largest sources using all scans which passed within $1'7$ of the source position and comparing these results with those obtained with a $1'0$ limit. These data are also included in Table 3-9. Two independent tests confirm the validity and usefulness of the models. First, the average ratio of the $1'0$ to $1'7$ corrected flux was $.989 \pm .016$, which is consistent with the ideal value of unity. Second, the model-dependent ratio of the two correction factors agrees with the independently measured ratio of uncorrected fluxes. The average $1'0$ to $1'7$ uncorrected flux ratio is $1.030 \pm .017$, and the average correction factor ratio is $1.042 \pm .006$. Since any inconsistency between the model and the data (for flux extrapolations on the order of 10%) is much smaller than the correction being applied, the corrected fluxes were used in preparing Table 3-8. Although many of the sources for which this correction was performed are in the IRAS Small Scale Structure Catalog (Helou and Walker 1986; hereafter SSSC), the corrected coadd fluxes were deemed superior to the SSSC estimates, which are only good to about 30%.

The coadded fluxes in Table 3-8 were color corrected using spectral indices ($F_{\nu} \propto \nu^{\alpha}$) according to the prescription in the IRAS Explanatory Supplement (Beichman et al. 1985a). After the first correction, new spectral indices were computed using the corrected fluxes; and the process was iterated to convergence, which was rapid.

Table 3-9
IR Source Models for Extended Sources

Name	Max	Band	Raw	Corrected		Focal Plane Source	
	z0		Flux	c	Flux	a	b
NGC 157	1.0	1	1.77	0.997	1.78	0.75	0.51
		2	2.77	0.992	2.79	0.84	0.57
		3	19.55	0.996	19.63	0.77	0.52
		4	47.41	0.990	47.88	0.74	0.50
NGC 3521	1.0	1	5.23	0.962	5.44	1.10	0.58
		2	5.87	0.975	6.02	1.15	0.60
		3	50.43	0.969	52.05	1.09	0.57
		4	135.35	0.981	137.92	1.08	0.57
NGC 3556	1.0	1	2.73	0.826	3.30	1.88	0.57
		2	4.84	0.998	4.85	0.85	0.26
		3	35.68	0.966	36.92	1.03	0.31
		4	86.01	0.977	88.02	1.23	0.37
NGC 4088	1.0	1	2.30	0.973	2.37	1.20	0.52
		2	3.93	0.999	3.94	1.24	0.54
		3	29.49	0.981	30.07	1.32	0.58
		4	63.95	0.979	65.31	1.03	0.45
NGC 4157	1.0	1	1.93	0.835	2.31	2.35	0.56
		2	2.34	0.805	2.91	2.22	0.53
		3	18.96	0.897	21.15	2.00	0.48
		4	55.15	0.969	56.91	1.16	0.28
NGC 4254	1.0	1	4.17	0.997	4.18	0.61	0.61
		2	5.01	0.998	5.02	0.64	0.64
		3	41.16	0.986	41.76	0.75	0.75
		4	103.77	0.985	105.32	0.83	0.83
NGC 4303	1.0	1	3.67	0.959	3.83	0.95	0.95
		2	5.44	0.966	5.63	0.94	0.94
		3	36.83	0.967	38.09	0.91	0.91
		4	75.74	0.978	77.40	0.83	0.83
NGC 157	1.7	1	1.58	0.962	1.64	0.71	0.48
		2	2.56	0.960	2.67	0.83	0.56
		3	18.14	0.960	18.91	0.77	0.52
		4	47.16	0.974	48.41	0.70	0.47

Table 3-9
(continued)

Name	Max z0	Band	Raw Flux	Corrected c Flux	Focal Plane a	Source b	
NGC 3521	1.7	1	6.05	0.934	6.48	1.18	0.62
		2	6.73	0.932	7.22	1.28	0.67
		3	52.09	0.950	54.83	1.13	0.59
		4	130.06	0.943	137.98	1.03	0.54
NGC 3556	1.7	1	2.75	0.873	3.15	1.62	0.49
		2	4.90	0.992	4.94	0.82	0.25
		3	35.52	0.943	37.68	1.20	0.36
		4	86.83	0.936	92.74	1.45	0.44
NGC 4088	1.7	1	2.24	0.894	2.51	1.01	0.44
		2	3.91	0.904	4.32	1.03	0.45
		3	28.00	0.912	30.70	1.06	0.46
		4	66.13	0.934	70.82	0.90	0.39
NGC 4157	1.7	1	1.99	0.759	2.62	2.55	0.61
		2	2.51	0.774	3.24	2.12	0.51
		3	19.09	0.856	22.30	1.94	0.46
		4	54.68	0.937	58.35	1.12	0.27
NGC 4254	1.7	1	4.16	0.951	4.38	0.61	0.61
		2	5.01	0.970	5.16	0.57	0.57
		3	36.62	0.938	39.05	0.73	0.73
		4	95.85	0.921	104.09	0.86	0.86
NGC 4303	1.7	1	3.18	0.932	3.41	0.89	0.89
		2	4.21	0.923	4.56	0.95	0.95
		3	32.36	0.929	34.84	0.92	0.92
		4	70.01	0.932	75.08	0.82	0.82
NGC 972	1.2	1	2.21	1.000	2.21	0.54	0.29
		2	3.96	1.000	3.96	0.53	0.29
		3	35.27	0.999	35.30	0.70	0.38
		4	67.33				
NGC 1084	1.2	1	2.11	1.000	2.11	0.42	0.23
		2	3.37	1.000	3.37	0.40	0.21
		3	31.20	0.997	31.28	0.56	0.30
		4	61.69				

Table 3-9
(continued)

Name	Max z0	Band	Raw Flux	Corrected c Flux	Focal Plane a	Source b
NGC 3810	1.2	1	1.47	0.992	1.48	0.54
		2	2.00	0.999	2.00	0.45
		3	14.90	0.987	15.10	0.62
		4	40.87	0.990	41.29	0.66
NGC 3893	1.2	1	1.83	1.000	1.83	0.50
		2	1.88	0.999	1.88	0.42
		3	17.20	0.999	17.21	0.55
		4	40.68			0.35
NGC 4030	1.2	1	1.67	1.000	1.67	0.52
		2	2.25	1.000	2.25	0.52
		3	21.76	1.000	21.76	0.56
		4	60.20			0.42
NGC 4038	1.2	1	2.60	1.000	2.60	0.50
		2	7.41	1.000	7.41	0.46
		3	52.57	0.997	52.75	0.56
		4	91.39	0.995	91.86	0.64
NGC 4041	1.2	1	1.27	1.000	1.27	0.25
		2	1.84	1.000	1.84	0.22
		3	15.66	0.999	15.68	0.41
		4	35.89			0.41
NGC 4321	1.2	1	2.58	0.996	2.59	0.65
		2	3.53	1.000	3.53	0.37
		3	26.43	0.994	26.58	0.67
		4	73.30	0.981	74.71	0.92
NGC 4414	1.2	1	3.27	1.000	3.27	0.46
		2	4.05	1.000	4.05	0.59
		3	32.07	0.997	32.16	0.56
		4	80.54			0.34
NGC 4501	1.2	1	2.23	0.984	2.27	0.91
		2	3.12	0.984	3.17	1.01
		3	18.69	0.986	18.96	0.92
		4	68.18			0.52

Table 3-9
(continued)

Name	Max z0	Band	Raw Flux	Corrected c	Flux	Focal Plane a	Source b
NGC 4527	1.2	1	2.73	0.978	2.79	0.96	0.35
		2	4.29	0.997	4.30	0.69	0.25
		3	33.02	0.985	33.52	0.81	0.29
		4	70.34	0.976	72.08	0.90	0.33
NGC 4654	1.2	1	1.16	1.000	1.16	0.53	0.33
		2	2.42	1.000	2.42	0.41	0.26
		3	15.26	0.999	15.28	0.58	0.37
		4	42.47				
NGC 4666	1.2	1	3.46	0.992	3.49	1.40	0.47
		2	3.78	0.999	3.79	1.21	0.41
		3	38.36	0.984	38.98	1.53	0.52
		4	89.47	0.989	90.48	1.51	0.51
NGC 5054	1.2	1	1.11	1.000	1.11	0.38	0.24
		2	1.81	1.000	1.81	0.37	0.23
		3	13.57	0.998	13.60	0.52	0.32
		4	30.28				
NGC 5248	1.2	1	2.08	1.000	2.08	0.41	0.31
		2	3.07	1.000	3.07	0.37	0.28
		3	22.09	0.999	22.11	0.46	0.35
		4	57.58				
NGC 5676	1.2	1	1.25	0.999	1.25	0.58	0.31
		2	1.78	0.995	1.79	0.61	0.32
		3	13.20	0.997	13.24	0.67	0.35
		4	35.23				
NGC 5775	1.2	1	2.01	0.935	2.15	1.45	0.41
		2	2.71	0.875	3.10	1.89	0.53
		3	24.96	0.932	26.78	1.47	0.41
		4	57.61				
NGC 1055	1.2	1	2.36	1.000	2.36	0.80	0.32
		2	3.19	0.999	3.19	0.80	0.32
		3	23.45	0.999	23.48	0.81	0.32
		4	69.77				

Table 3-9
(continued)

Name	Max z0	Band	Raw Flux	Corrected c Flux	Focal Plane a	Source b	
NGC 3079	1.2	1	2.82	0.916	3.08	1.17	0.26
		2	3.92	0.983	3.99	0.91	0.20
		3	52.83	0.969	54.53	0.82	0.18
		4	109.51				
NGC 4605	1.2	1	0.86	0.994	0.87	0.44	0.18
		2	1.41	0.989	1.43	0.59	0.25
		3	14.74	0.981	15.03	0.55	0.23
		4	33.20				
NGC 5005	1.2	1	1.85	0.966	1.92	0.89	0.45
		2	2.53	0.990	2.56	0.62	0.31
		3	23.11	0.972	23.77	0.69	0.35
		4	67.42	0.982	68.62	0.85	0.43
NGC 7479	1.2	1	1.55	0.997	1.56	0.40	0.32
		2	4.87	1.000	4.87	0.25	0.19
		3	16.42	0.995	16.50	0.50	0.40
		4	28.47				

B. Comparison with PSC Fluxes

It is useful to compare the total fluxes in the various IRAS bands (before color correction) with the corresponding PSC values as a function of optical diameter. This serves as a direct demonstration of the importance of extended emission in the infrared and also as a needed guideline for when PSC fluxes of bright galaxies may confidently be used. Figure 1a plots the ratio of total flux to PSC flux at 12 and 25 μm versus optical diameter for IBGS sources which are not in the SSSC. Figure 1b is the same for the 60 and 100 μm fluxes. At 12 and 25 μm extended

emission induces errors of $\geq 20\%$ in the PSC fluxes of galaxies with diameters in excess of $2''.5$. We therefore recommend that 1-d coadds be used to study such sources. At $60\text{ }\mu\text{m}$ errors in PSC fluxes due to extended emission do not become severe ($\geq 20\%$) until an optical diameter of $5''.0$, while at $100\text{ }\mu\text{m}$ the PSC is reliable to the $8''$ optical diameter limit of our sample.

Figure 3-1a
Total/PSC Flux vs. Optical Diameter
Non-SSSC Sources, Bands 1 and 2

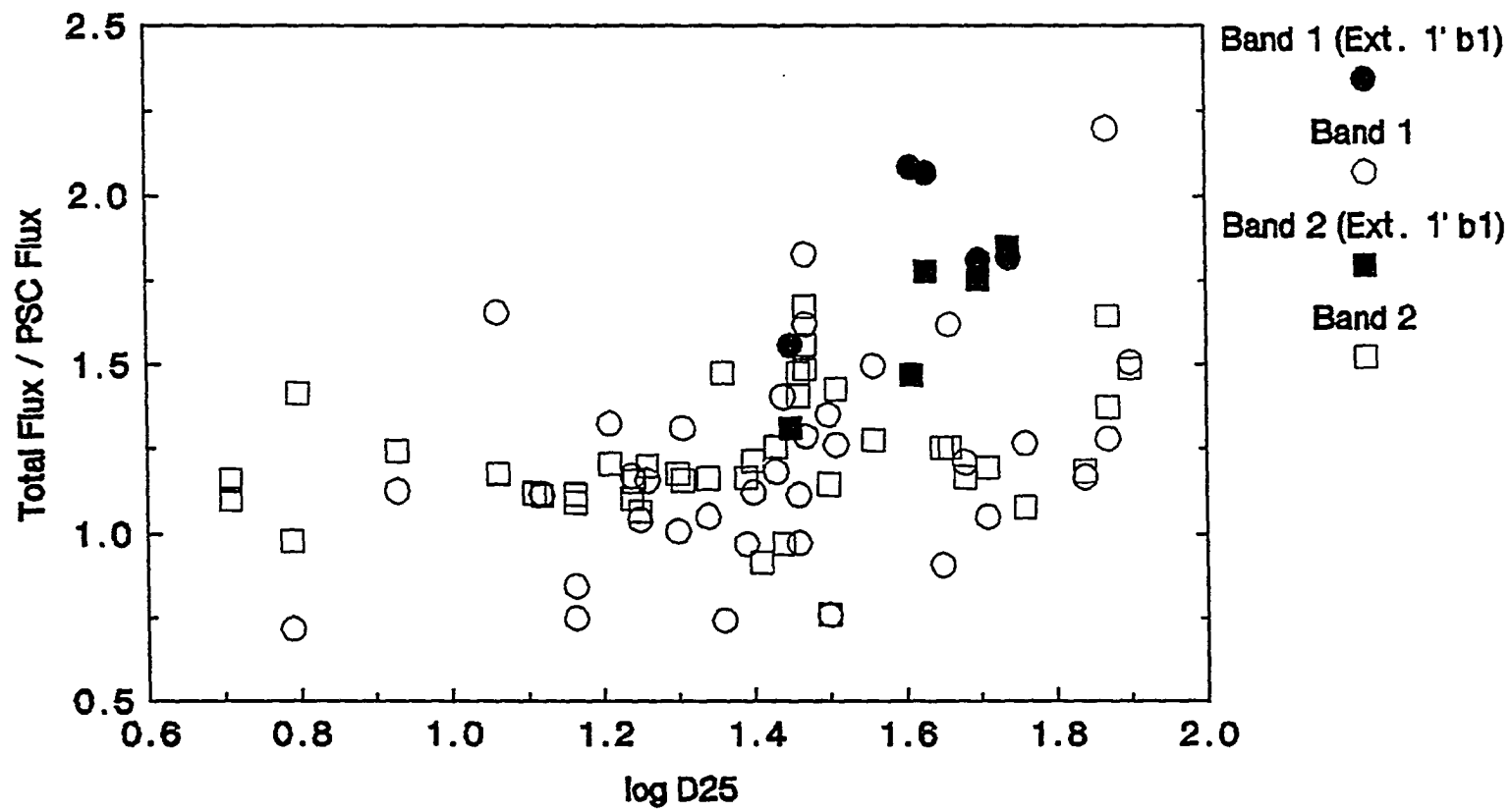
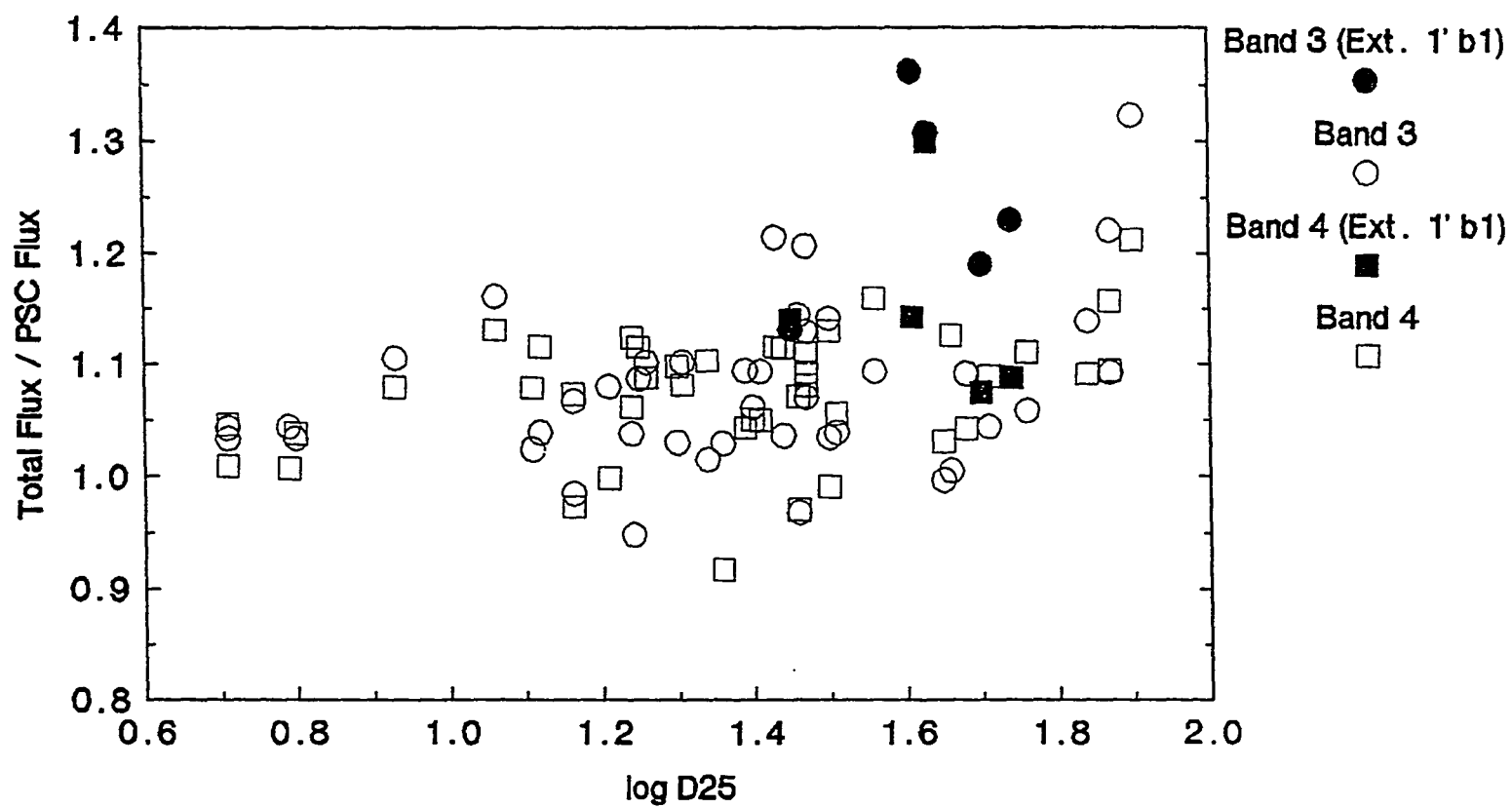


Figure 3-1b
Total/PSC Flux vs. Optical Diameter
Non-SSSC Sources, Bands 3 and 4



V. Discussion

A. IR Color-Color and Color-Luminosity Relations

Figures 3-2, 3-3, and 3-4 show the well known IRAS color-color (Helou 1986) and color-luminosity relations (e.g. Soifer et al. 1987) for objects in the IBGS. Total, color corrected IRAS measurements taken from Table 3-8 were used to prepare these figures. Galaxies with peculiar or irregular morphology ($t \leq 0$) and possible, probable, or definite Seyfert galaxies are plotted with special symbols in the figures.

Figure 3-2 is a plot of $12/25 \mu\text{m}$ versus $60/100 \mu\text{m}$ color, which Helou (1986) has termed the IRAS color-color diagram. All IBGS galaxies lie in a single broad band in this diagram, along which $12/25 \mu\text{m}$ color is anticorrelated with $60/100 \mu\text{m}$ color. Helou (1986) has obtained a similar result for a large sample of galaxies detected in all four IRAS bands and selected so as to avoid extremely warm $25/60 \mu\text{m}$ colors. Helou has noted that estimated star formation rates, IR luminosities, and IR/blue luminosity ratios all increase from right to left along the galaxy band. It is readily apparent from Figure 3-2 that the incidence of Seyfert nuclei and peculiar optical morphology also increase from right to left. The increasing prevalence of peculiar optical morphology in the region of this diagram associated with high star formation rates is consistent with the results of evolutionary galaxy modeling by Larson and Tinsley (1978), which indicate that the aberrant UBV colors of galaxies displaying

disturbed morphology can be explained using a rapid burst of star formation. There is a possible tendency for Seyfert galaxies to lie above non-Seyfert galaxies with peculiar morphology in this diagram, but the general behavior of both types of object in the figure is the same.

We interpret Figure 3-2 as evidence that all of the galaxies in the IBGS are dust-dominated in the infrared. The locus of power laws is shown as a solid line in Figure 3-2, and it can be seen that these sources deviate strongly from power law spectra. Furthermore, Désert (1986) has shown that the most obvious feature of Figure 3-2, the anticorrelation of 12/25 μm color with 60/100 μm color, is characteristic of emission by dust grains with compositions and size distributions similar to interstellar dust when exposed to varying levels of UV flux.

At low flux levels line and continuum emission from small grains and polycyclic aromatic hydrocarbons dominates the IRAS 12 μm band. As the flux level increases, destruction of the smallest particles and increasing radiation from the smallest surviving graphite grains at 25 μm decreases the 12/25 μm flux ratio. Meanwhile, the hotter average temperature of the energetically most important grains of intermediate size increases the 60/100 μm flux ratio. This gives rise to a one-parameter family of points (i.e. a curve) in the 12/25-60/100 μm plane when the input spectrum and grain population are held fixed. A superposition of components lying along this curve, as well as variations in grain properties and (to a lesser extent) the input spectrum, cause galaxies dominated by dust emission to spread out in a band, as seen in

Figure 3-2.

This interpretation of Figure 3-2 is supported by a wealth of observational evidence. Helou's (1986) finding that galaxies thought to have high star formation rates are found near the top left side of the band (which we shall term the "active" side), while galaxies with normal star formation rates and no IR excess are found near the lower right side of the band (the "quiescent" side) is consistent with the idea that the mean intensity of the UV radiation field to which dust in a galaxy is exposed increases from right to left along the band. The colors of infrared cirrus lie at the extreme edge of the quiescent region, as expected (Helou 1986). Furthermore, galaxies with H II region nuclei, which constitute the majority of those in the active region of Figure 3-2 have curved, steeply rising IR spectra characteristic of dust radiation and invariably show IR spectral features (notably $9.7\ \mu\text{m}$ silicate absorption) associated with warm dust grains (Phillips, Aitken, and Roche 1984).

The second most common nuclear spectrum of galaxies in the active region of Figure 3-2 is that of a type 2 Seyfert. These objects also show steeply rising, curved IR spectra and have $10\ \mu\text{m}$ excesses which increase toward redder U-B colors (Rieke 1978). These objects also display $9.7\ \mu\text{m}$ silicate absorption quite frequently, though not as strong as that seen in H II region nuclei (Lebofsky and Rieke 1979). Finally, their optical spectra are invariably reddened by $A_V \geq 1$ mag (Koski 1978; Malkan 1983, 1986; Edelson and Malkan 1986; Kailey and Lebofsky 1988).

Finally, the two type 1 Seyferts in the IBGS (Mkn 231, NGC 7469) are not representative of this class of objects, but there is good evidence that the IR excess of both is due to dust (Aitken, Roche, and Phillips 1981; Cutri et al. 1984; Rieke 1976; Cutri, Rieke, and Lebofsky 1984; Roche, Aitken, and Whitmore 1983).

Further insight into the physical processes occurring in both the active and quiescent galaxies in the IBGS can be gained by considering Figures 3-3 and 3-4. These figures show plots of integrated IR luminosity, L_{IR} , against 60/100 μ m color and IR excess (i.e. IR/blue flux ratio) respectively. The appearance of bimodal behavior alluded to in Section I is quite pronounced in these plots. Over a wide range of $L_{IR} \leq 10^{10} L_{\odot}$, the galaxies show a narrow range of colors and IR excesses, which is uncorrelated with L_{IR} . At higher IR luminosities, L_{IR} becomes loosely correlated with L_{IR}/L_B^2 and increasingly well correlated with F_{60}/F_{100} . Moreover, the parameter controlling this bimodal behavior appears to be the presence or absence of peculiar morphology and/or a Seyfert nucleus. That is, the correlations in question appear to exist only for the Seyfert and peculiar galaxies in the sample.

The behavior exhibited by the normal galaxies in Figure 3-3 and Figure 3-4 is in fact what one would expect from dust heated by ambient starlight and H II regions within galactic disks if the ratio of present to past star formation varies little among them. In that case, one would

² In this work L_B is defined as $\nu f_{\nu}(0.44 \mu\text{m})$ computed using B_{OT} from Table 2-4 and the zero point flux given by Allen (1976).

expect luminosity to be proportional to galaxy mass and color to be independent of mass, since 10^5 Orion complexes have, after all, the same spectral energy distribution as one Orion complex. The proposition that the ratio of present to past star formation rates is the same in most normal spirals is consistent with both Galactic (Miller and Scalo 1979; Twarog 1980) and extragalactic (Kennicutt 1983; Searle, Sargent, and Bagnuolo 1970; Larson and Tinsley 1978) studies.

Given the fact that the Seyfert and peculiar IBGS galaxies, like the normal galaxies are dominated by dust emission, the observed correlation of 60/100 μm color temperature with IR luminosity among them implies that variations in average dust temperature are more important than variations in the mass of emitting dust in explaining the large range of IR luminosities which they occupy. This could come about in one of two ways. First, it is conceivable that the IR luminosity of both the Seyfert galaxies and those with peculiar morphology is dominated by an enhanced rate of star formation in their disks. Regions of active star formation are characterized by a warm 60/100 μm color, high IR/blue flux ratio, and high LIR to mass ratios. Thus, if the Seyfert and peculiar galaxies have a relatively narrow range of gas masses, the fraction of that mass which lies in active star formation regions would be correlated with 60/100 μm color, IR/blue flux ratio, and IR luminosity. This can be tested by comparing the observed 60/100 μm colors and IR excesses of star formation regions with those of Seyfert and peculiar galaxies in Figures 3-3 and 3-4. A study of the integrated 60 μm , 100 μm , and blue fluxes of star

formation regions in the Galaxy and in nearby galaxies such as M31 and M33 is needed for this purpose. In the mean time, however, the hypothesis of enhanced disk star formation appears unlikely based on information to be adduced shortly.

The other possibility is that both the Seyfert and peculiar galaxies are dominated by a single power source whose IR colors and luminosity are related to variations in one or more physical parameters, such that the 60/100 μm flux ratio increases with luminosity.

For example, consider a spherical shell of gas and dust surrounding a source of UV and optical radiation. The power source could consist of recently formed stars in a cavity of ionized gas or a Seyfert nucleus and associated emission line regions. The emergent IR spectrum of the dust shell depends on the run of grain properties and grain number density with radius, as well as the luminosity of the central source. It is insensitive to the shape of the input spectrum, since (1) the grain cross section is approximately independent of wavelength in the short wavelength limit, and (2) much of the ionizing radiation is converted to a standard spectrum by the intervening ionized nebula. The destruction of grains in the ionized central region of the shell and the balance between gravitational forces and radiation pressure on the dust grains (in the case of Eddington accretion) will regulate the grain properties and grain density as a function of distance from the central source in a way that depends on the luminosity of the source, nuclear mass, and the dominant grain destruction process. Detailed construction of a model such as this

is outside the scope of this work but might explain the observed correlations.

A plot of 12/100 μm color versus 25/60 μm color is useful in deciding between the two alternatives just discussed. Figure 3-5 shows such a plot for galaxies in the IBGS. The behavior of normal galaxies in this figure, which we shall call the second IRAS color-color diagram, is quite different from that of the Seyfert and peculiar galaxies. The former occupy a very narrow range of colors on both axes, showing no correlation, while the latter seem to spread out in a band with both colors well-correlated. The fact that the Seyfert/peculiar galaxy band extends well outside the range of normal galaxy colors in both directions is highly significant.

This behavior is very difficult to account for in the first of the two scenarios just described. If we assign fixed 12/100 μm and 25/60 μm colors to regions of active star formation, no combination of those colors with the normal galaxy colors could reproduce the behavior of the Seyfert and peculiar galaxies in the second IRAS color-color diagram. On the other hand, if we suppose that regions of active star formation form a one-parameter sequence in the 12/100-25/60 μm plane, then the wide range of integrated galaxy colors observed suggests that the controlling parameter is a global property of a galaxy. This would be difficult to arrange without resorting to a single, centrally located region of star formation, which is tantamount to adopting the second scenario described above, rather than the first.

The number of non-Seyfert galaxies which are well separated from the locus of normal galaxies in Figure 3-5 is small, and none of them lie in the upper right corner of the active galaxy sequence. It is therefore necessary to examine non-IBGS galaxies which show signs of interaction and/or nuclear starbursts in order to determine whether their behavior is well represented by this figure.

For this purpose we have assembled data on a heterogenous sample of IR-luminous, non-Seyfert galaxies thought to be undergoing nuclear starbursts which covers a wide range of 25/60 μm colors. These include

1. Four non-Seyfert "Warm IRAS Galaxies" (Chapter 2)--galaxies having $F_{60}/F_{25} \geq 3$, for which coadded IRAS data are available in Table 2-3 (Chapter 2). Warm IRAS galaxies invariably have high infrared luminosities and optical emission lines in their nuclear spectra (see Chapter 2 and references therein).
2. Galaxies in Bushouse's (1986) optically selected sample of interacting galaxies which Bushouse, Lamb, and Werner (1988; hereafter BLW88) have determined to be undergoing high L_{IR} nuclear starbursts. These objects, which include the IBGS galaxy NGC 1614, are listed in Table 5 of BLW88; and coadded IRAS fluxes are given in Table 1 of that work.
3. A subset of Armus, Heckman, and Miley's (AHM87) IR-flux-limited sample of "Far-IR Galaxies"--these objects are selected for cold 25/60 μm colors and warm 60/100 μm colors and are characterized by highly peculiar optical morphology,

large infrared luminosities, and LINER or H II region/LINER transition spectra (AHM87; Heckman, Armus, and Miley 1987). Our subset was chosen for extremely cold 25/60 μm colors ($\alpha_{25,60} \leq -2.6$), and--after excluding the type 2 Seyferts Mkn 273 and IC 4553--includes two IBGS galaxies (NGC 2623, IC 860). IRAS fluxes were taken from Table 3-8 or the PSC.

4. Rieke, Lebofsky, and Walker's (1988; hereafter RLW88) prototype nuclear starburst galaxies--NGC 5253, NGC 253, M82, NGC 4736. These authors have proposed a four-stage evolutionary sequence for nuclear starbursts, which is exemplified by these four galaxies. IRAS fluxes were taken from the PSC despite the large angular diameters, since the colors of the nuclear regions undergoing the starburst are of interest.
5. The well studied super-luminous starburst/LINER IBGS galaxy NGC 6240 (e.g. Rieke et al. 1985; AHM87).
6. The irregular IBGS galaxy, ZG 1510+07, which has extremely cold 25/60 μm color, $L_{\text{IR}} = 1.5 \times 10^{11} L_{\odot}$ and is not a known Seyfert.

These galaxies are listed in Table 3-10 and are plotted on the Second IRAS color-color plane in Figure 3-6. The figure shows that the second IRAS color-color relation does indeed hold for objects generally considered starburst galaxies (as well as dusty Seyfert galaxies) over a very wide range of 25/60 μm colors. Further study of the objects in Table 3-10 is

needed to test the starburst hypothesis and, if it is found to be correct, to determine what physical property of the starburst corresponds to its position along this sequence.

Table 3-10
Starburst Galaxy Sample

Name	Source ^a
UGC 7905	BLW88
Arp 248	BLW88
UGC 10033	BLW88
Arp 252	BLW88
UGC 2992	BLW88
UGC 10267	BLW88
UGC 8335	BLW88
UGC 12699	BLW88
NGC 1614	BLW88, IBGS
UGC 6471/2	BLW88
3 Zw 35	AHM87
IC 860	AHM87, IBGS
ES507-G70	AHM87
ZG1510+07	IBGS
IRAS1056+25	AHM87
NGC 2623	AHM87, IBGS
ES320-G30	AHM87
NGC 6240	IBGS
ZG0229+02	Chapter 2
IRAS0425-07	Chapter 2
IRAS0425-04	Chapter 2
IRAS0428-09	Chapter 2
NGC 5253	RLW88
NGC 253	RLW88
NGC 3034	RLW88
NGC 4736	RLW88

Notes to Table 3-10

a. This column gives a reference to the work in which the galaxy is identified as a probable starburst galaxy (see text). IBGS refers to this work.

The behavior of the Seyfert and peculiar galaxies in Figures 3-3 through 3-6 is surprisingly similar and suggests a similar phenomenology in both. As we have seen, the second IRAS color-color relation is most easily explained on the supposition that all of these galaxies are dominated by a single, centrally located power source, such as a Seyfert nucleus or nuclear starburst enclosed in a dust shell which is optically thick in the UV. The similar IR spectral properties of these sources may result from the presence of intense nuclear starbursts in the Seyfert galaxies, or dust-embedded active nuclei in the peculiar galaxies; or they may merely result from a similar dust shell structure, which is insensitive to the nature of the heating source. Detailed theoretical models of dust-embedded active nuclei and nuclear starbursts may be useful in eliminating one or more of these possibilities.

Infrared imaging at 10 μm and longer wavelengths is also capable of placing useful constraints on the size of the source which heats the dust. For example, Telesco, Becklin, and Wynn-Williams (1980) found 20 μm emission in NGC 1068 to be extended over 3", from which they inferred the presence of an extended heating source not associated with the Seyfert nucleus. Further observations of this kind, along with careful modelling of them, would be extremely useful in determining the heating source for the dust in type 2 Seyfert nuclei, as well as the objects listed in 3-10.

Figure 3-2
IRAS Color-Color Diagram
Infrared Bright Galaxy Sample

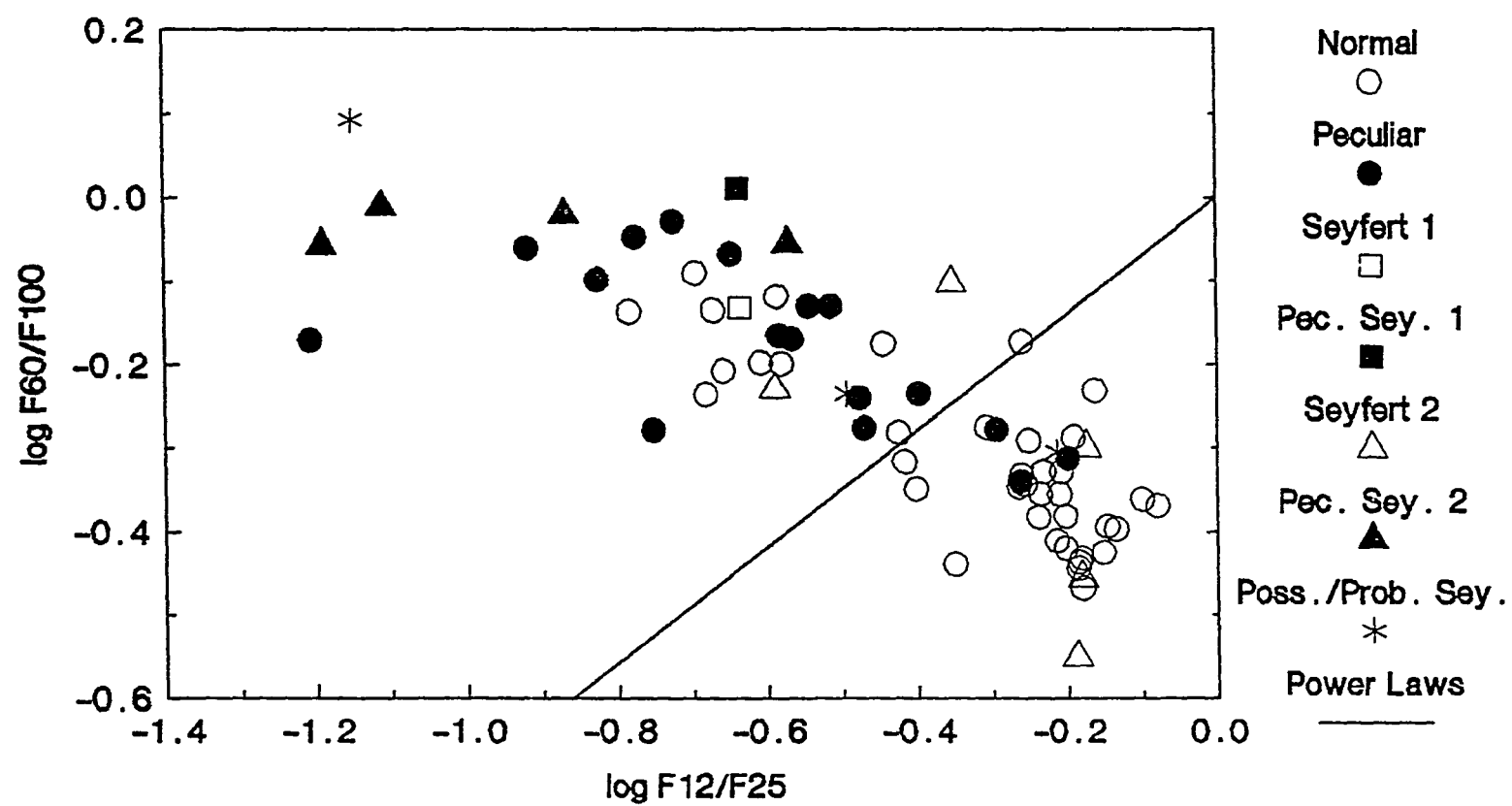


Figure 3-3
IR Color-Luminosity Diagram
Infrared Bright Galaxy Sample

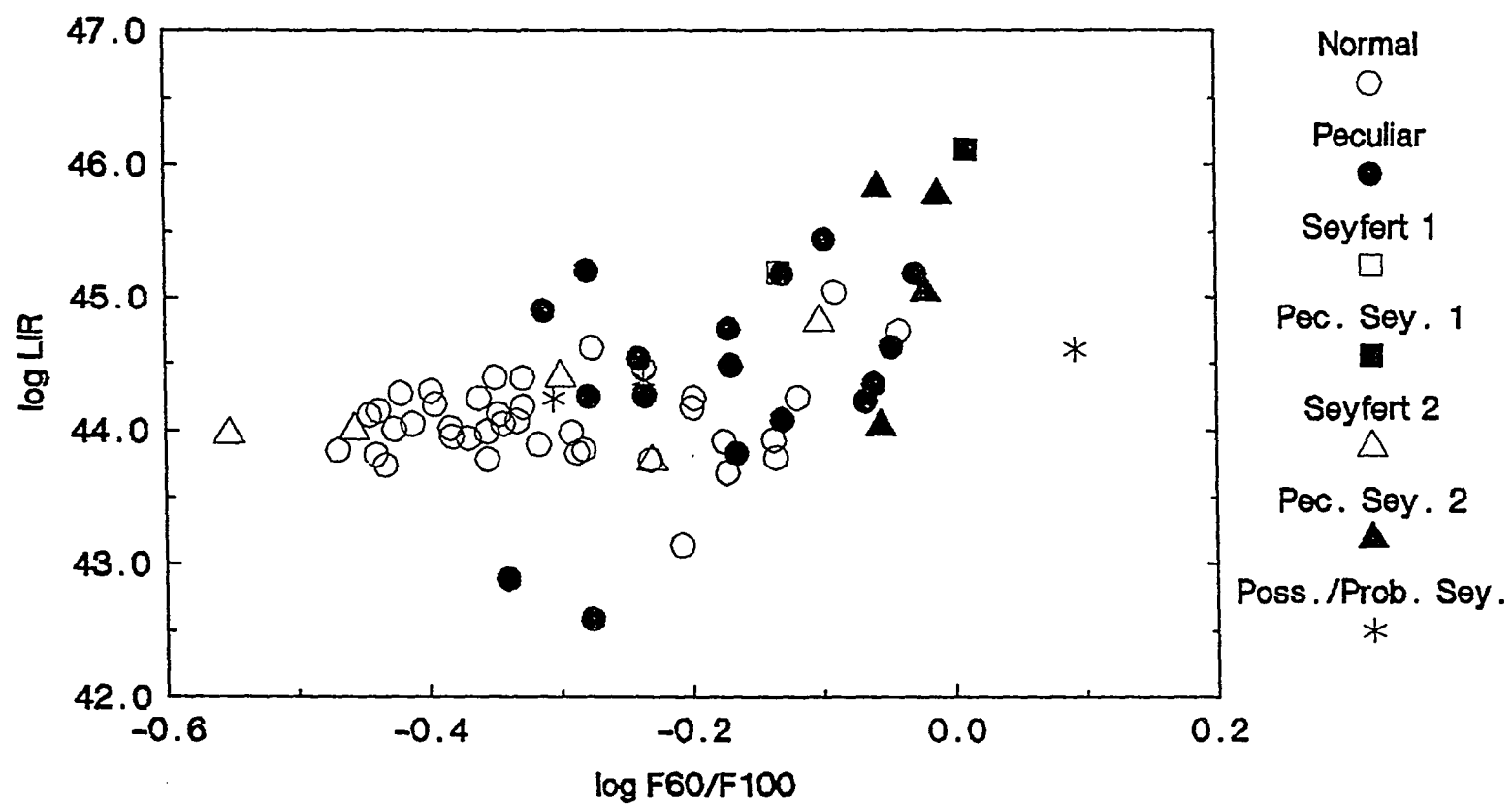


Figure 3-4
IR/Blue Color-Luminosity Diagram
Infrared Bright Galaxy Sample

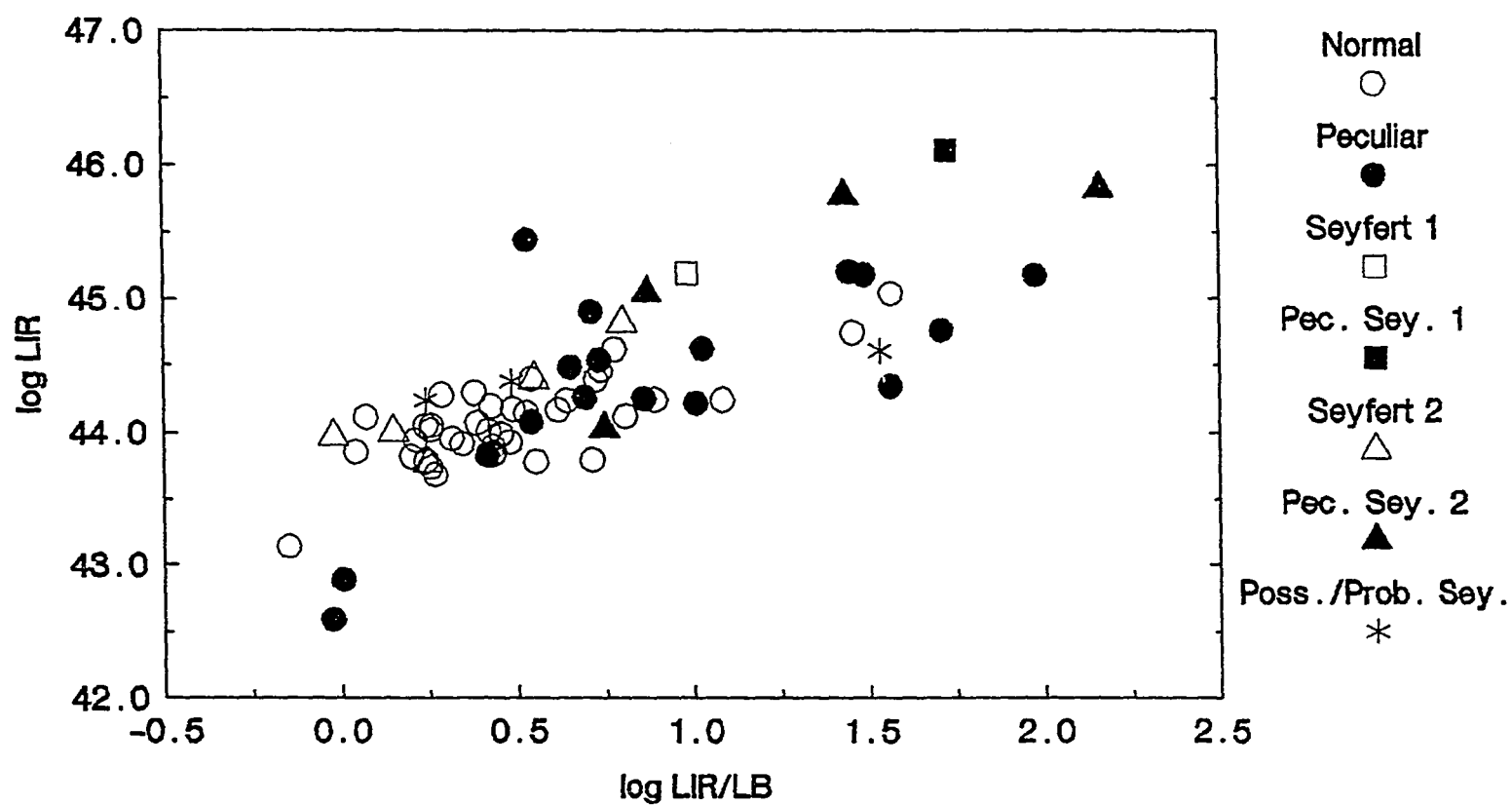


Figure 3-5
Second IRAS Color-Color Diagram
Infrared Bright Galaxy Sample

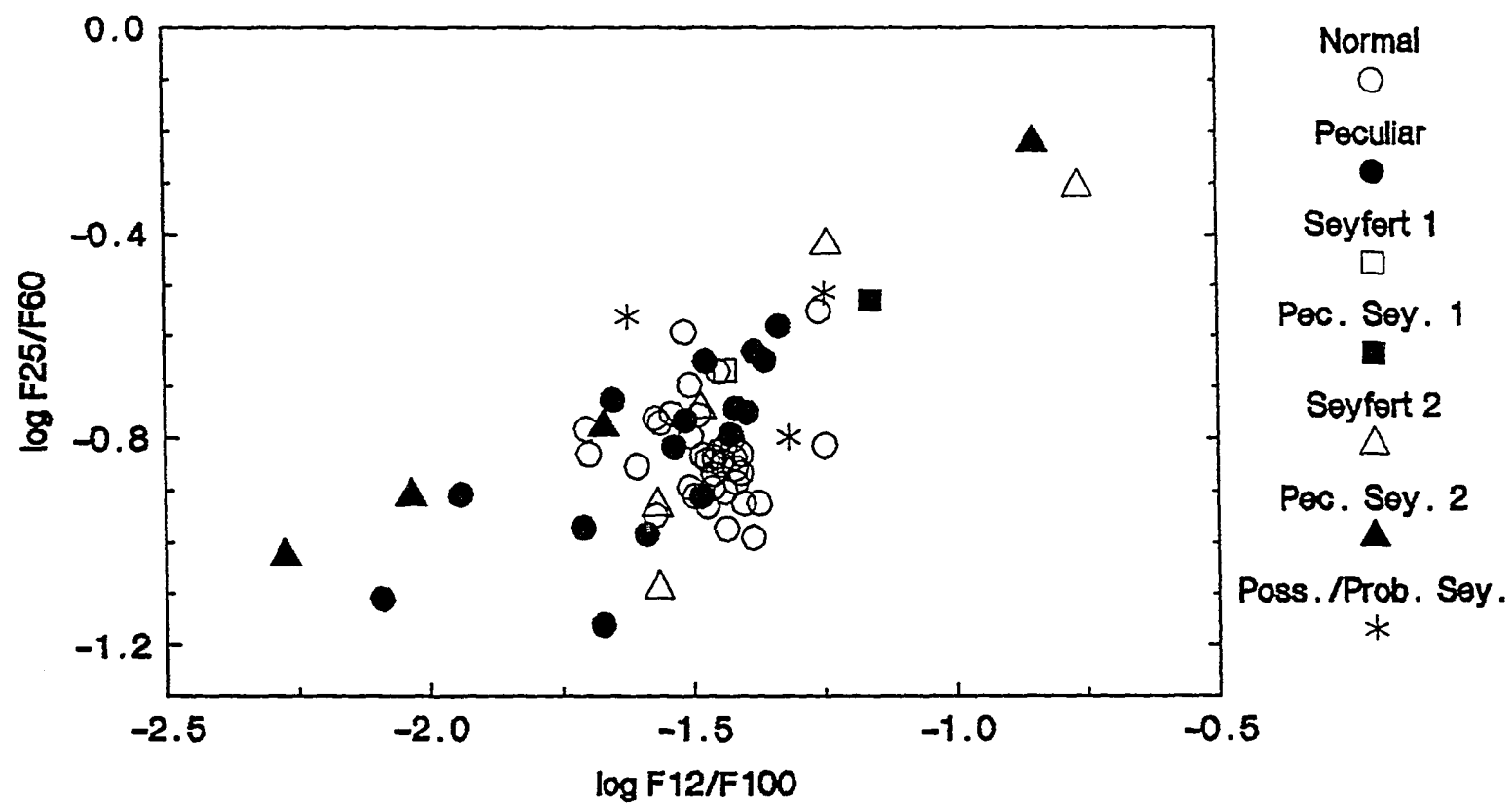
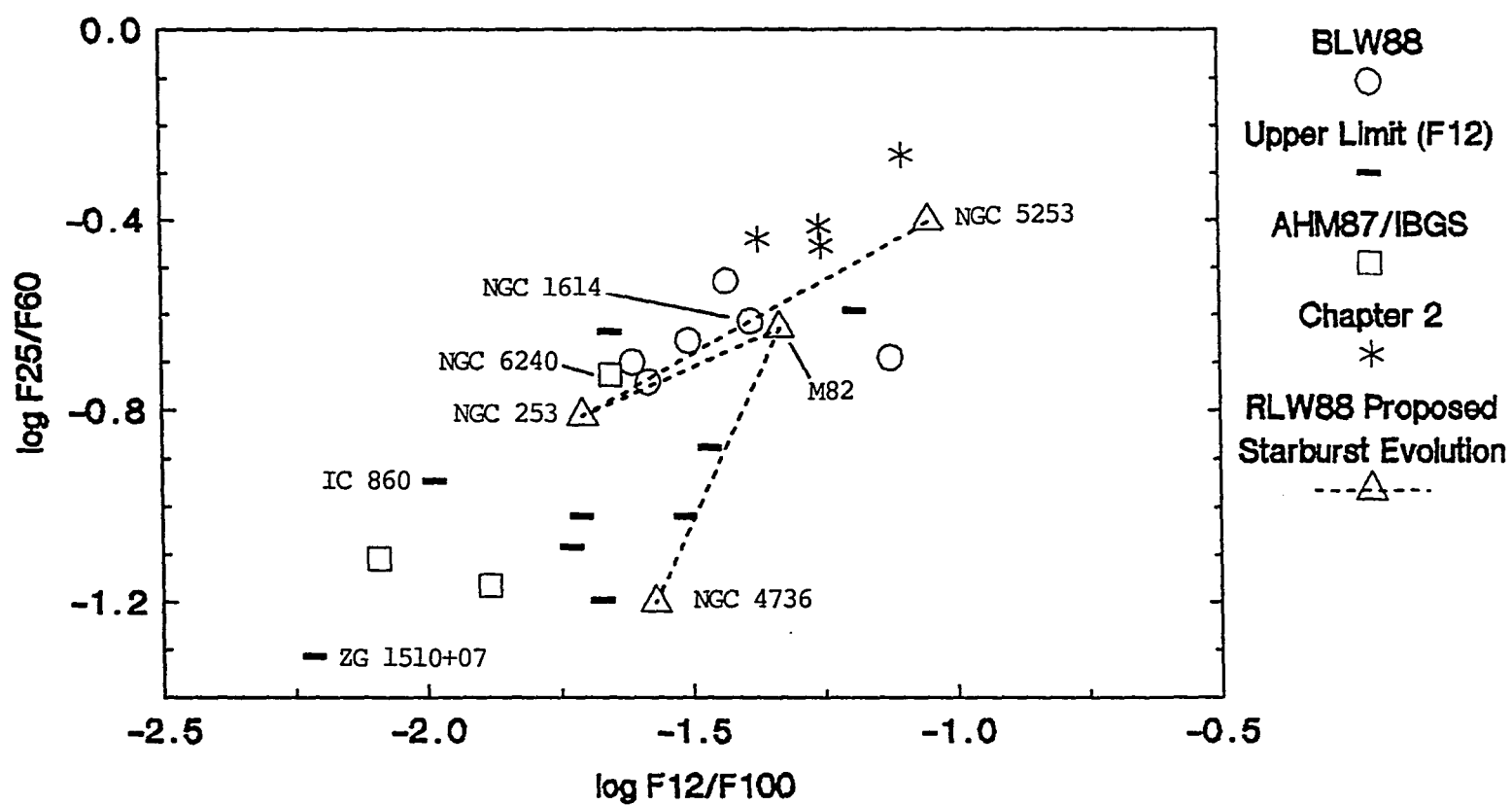


Figure 3-6
Second IRAS Color-Color Diagram
High LIR Starburst Galaxies



B. Single Band Luminosities

Table 3-11 lists the average fraction of integrated IR luminosity, L_{IR} , measured in the four IRAS bands (i.e. $\delta\nu F_\nu$, where $\delta\nu$ is the approximate frequency width of the filter as given in Table 3-1). The 60 μm band is dominant, followed by 100 μm , which is not surprising, considering that the 60/100 μm flux ratio is the best indicator of luminosity among all of the IRAS colors.

Table 3-11
Fraction of L_{IR} in IRAS Bands

Band	12 μm	25 μm	60 μm	100 μm
Mean Fraction	12.8%	13.1%	51.6%	22.4%
Sigma	4.9%	5.3%	7.1%	5.5%

A more interesting question is, Assuming that the IR spectra of galaxies arise from a quiescent component (i.e. infrared cirrus and normal levels of disk star formation) and an "active" component, which of the single band luminosities contains the largest relative contribution from the active regions of a galaxy? We have seen that galaxy activity (as operationally defined here) increases as 12/25 μm flux ratio decreases and as 60/100 μm flux ratio increases. The "active" IR component may also be thought of as an IR component which contributes little or no blue flux to a galaxy, which accounts for the increase of IR/B luminosity ratio with L_{IR} at the right hand side of Figure 3-4.

Table 3-12 gives the squared linear correlation coefficients for the regression of the various single IRAS band luminosities on L_B , on $\log(F_{12}/F_{25})$, and on $\log(F_{60}/F_{100})$. IC 860 and ZG 1510+07, for which we were unable to measure a 12 μm flux, were excluded in all cases, so that all the regressions have 68 points; and the 99% confidence level is 0.10. The important result, however, is not the significance of the correlations but that L_{25} is least correlated with L_B , best anticorrelated with $\log(F_{12}/F_{25})$, and best correlated with $\log(F_{60}/F_{100})$. Assuming, then, that the IR spectra of galaxies are composed of an active component and a quiescent component, we are able to conclude that the ratio of active to quiescent contributions is highest in the IRAS 25 μm band. It follows that this band is optimum for selecting flux limited samples of IR-active galaxies.

We hypothesize, based on this result and on the foregoing section, that the active component of the IR spectra of galaxies is associated with their nuclei, while the quiescent component is contributed to both by star formation regions and infrared cirrus, with the dominant contributor at 25 μm being star formation regions. Our finding that the active component is most visible at 25 μm is thus consistent with Devereaux's (1987) finding that the presence of compact nuclear sources in early type spirals is associated with strong 25 μm excess. It is also consistent with theoretical models of IR emission from the dust grains (Jura 1982) and polycyclic aromatic molecules (Puget, Léger, and Boulanger 1985) comprising infrared cirrus. These models predict substantial amounts of

emission from the former particles at 60 μm and 100 μm and from the latter at 12 μm but negligible emission at 25 μm .

Table 3-12
Squared Linear Correlation Coefficients

Luminosity in Band	versus L_B	versus $\log (F_{12}/F_{25})$	versus $\log (F_{60}/F_{100})$
12 μm	0.486	0.027	0.105
25 μm	0.291	0.323	0.386
60 μm	0.295	0.293	0.286
100 μm	0.387	0.160	0.121
L_{IR}	0.333	0.247	0.253

VI. Summary

We have presented a large body of observational data on a sample of galaxies selected for brightness integrated over the IRAS spectral range (7 μm to 130 μm) and limited to an optical diameter of less than 8'. The sample is biased against galaxies with low surface brightness due to selection using the IRAS PSC and is therefore not useful for comparing space densities of various classes of objects. However, the flux measurements presented here are not biased against extended emission in any of the IRAS bands. These are the first such measurements to be published for most of the galaxies in our sample and represent a substantial improvement over PSC fluxes (for estimating total galaxy flux), especially at shorter wavelengths.

Our IR-selected sample is significantly higher in Seyfert galaxies and galaxies with peculiar or irregular morphology than an optically selected control. This supports the argument of AHM87 that IR samples appear less edge-on than optical samples (cf. Burstein and Lebofsky 1986) because of disturbed morphologies that are less intrinsically flat. At the 84% confidence level, we find that the peculiar and irregular objects in our sample have a mean axial ratio nearer unity than the optical sample, while the non-peculiar/irregular IR-selected objects are more nearly face on. This also tends to support the AHM87 hypothesis.

Total, color corrected IR fluxes in all of the IRAS bands have been measured for all 70 objects using one-dimensional aperture photometry. The objects are completely detected in all bands, except for two not detected at 12 μm . Substantial care has been taken not to exclude extended emission from the galaxy disks at short wavelengths. An estimate of morphological type, total B magnitude, and distance was obtained for all objects in the sample. For galaxies with optical diameters over 3' (after excluding SSSC galaxies), the total flux commonly exceeds the PSC estimate by ~20-100% at 12 μm and 25 μm and by ~10-30% at 60 μm . PSC estimates are increasingly accurate at lower diameters, as expected.

The 14 possible, probable, or definite Seyfert galaxies in our sample (mostly of type 2) have spectra which are likely to be dominated by dust emission. This conclusion is based on work by other authors and on their location in the 12/25-60/100 μm color-color plane (the IRAS color-color diagram), which is similar to that of other IR active

(starburst, LINER) galaxies. Seyfert galaxies and galaxies with peculiar or irregular morphology are concentrated toward the upper-left, "active" region of this diagram, while normal galaxies are found in the lower-right, "quiescent" region.

The IR active Seyfert/peculiar/irregular galaxies, unlike the quiescent (normal) galaxies, obey a second IRAS color-color relation and have infrared luminosities correlated with their 60/100 μm colors. Any differences between the Seyfert and non-Seyfert galaxies with respect to this behavior are fairly subtle. Thus, to a first approximation, the broad band infrared spectral energy distribution and infrared luminosity of IR active galaxies consists of four measurable quantities with two independent relationships among them and can therefore be modeled with just two parameters. If we choose bolometric luminosity of the source which heats the dust as one parameter, the other parameter determines the spectral energy distribution of the emergent IR power. If the dust is distributed isotropically about the source, this second parameter might then be the average optical depth of the dust shell.

If the distinctive IR spectral characteristics of Seyferts in our sample arise because the dust is heated primarily by a central UV/optical source rather than independent regions of star formation distributed over a gaseous disk, the similar behavior of the morphologically peculiar and irregular objects would tend to suggest a similar source geometry. Possibilities include dust-enshrouded active nuclei (e.g. Sanders, Soifer, and Neugebauer 1988) or a starburst confined to a central cavity of

ionized gas within a large molecular cloud complex (e.g. RLW88). Further theoretical and observational studies are needed to clarify this situation.

Chapter 4

IR SPECTRAL PROPERTIES OF NORMAL AND ACTIVE GALAXIES:

2. THE EFFECT OF NUCLEAR ACTIVITY ON THE INFRARED COLORS OF GALAXIES

Abstract

We have performed small aperture 10.6 μm photometry and nuclear spectroscopy on a large subset of an infrared bright galaxy sample, for which total, color corrected IRAS fluxes, morphological types, optical diameters, and distance estimates were presented and discussed in the previous chapter. In the last chapter it was argued that the infrared power emitted by galaxies in this sample is contributed to by two components exhibiting distinct spectral behavior: a quiescent component contributed to by both star formation and infrared cirrus in galactic disks, and an active component. Further, it was suggested that the distinctive spectral properties of the active component are most easily explained by hypothesizing a dust-embedded active nucleus or nuclear starburst in the active galaxies. Our observations (combined with data in the literature) of the nuclei of many of these galaxies strongly confirm this suggestion. Two observational measures of the importance of nuclear activity in the infrared are derived and discussed. Possible selection effects are examined and eliminated. It is shown that (1) infrared nuclear activity is more common in galaxies with peculiar or irregular optical morphology, Seyfert galaxies, and early type spirals, than among late type spirals. (2) Concentration of IR emission toward

the center of galaxies is associated with the presence of large amounts of ionized gas in the nucleus. (3) Nuclear sources are the predominant cause giving rise to IR luminosities above $10^{11} L_{\odot}$. (4) The nuclear fraction of the IR luminosity is well correlated with galactic 60/100 μm colors. The correlation has potential application as a standard candle, especially if far-IR imaging can be used to refine it. (5) Available observational data are consistent with the hypothesis that the 12/100-25/60 μm color-color relation obeyed by Seyfert and peculiar galaxies (Chapter 3) is a unique property of compact nuclear infrared sources. It is suggested that galaxy interactions commonly result in gas transport toward galactic nuclei, followed by a starburst proceeding from the center outward and/or formation of a Seyfert nucleus. Theoretical models of dust-enshrouded starbursts and active nuclei are needed to determine whether such a model can reproduce the behavior of nuclear IR sources in the 12/100-25/60 μm color-color plane and the 60/100 μm color-IR luminosity relationship.

I. Introduction

In the previous chapter we presented catalog containing total, color corrected IRAS fluxes and other observational data for a sample of infrared bright galaxies or galaxy mergers, the Infrared Bright Galaxy Sample (IBGS), along with a discussion of the basic observational properties of galaxies in the sample. Aside from the complete absence of elliptical galaxies in the sample--an indication of the importance of a

supply of gas and dust for producing IR emission--its most striking observational characteristics are the high incidence of morphological disturbances (often unambiguously the result of interactions) and the high rate of Seyfert activity.

A basic result of the discussion in Chapter 3 is that the infrared emission of galaxies in the IBGS consists of an "active" and "quiescent" contribution, where both components are powered by thermal emission from dust grains; and the active component displays a wide range of IR spectral shapes, which can be modelled to a first approximation with two parameters. The dissimilar behavior of the two components in infrared color-color and color-luminosity diagrams is quite striking. The active component is associated with high infrared ($\gtrsim 10^{10} L_{\odot}$) luminosities, a wide range of 25/60 μm and 12/100 μm colors, cold 12/25 μm and warm 60/100 μm colors, 60/100 μm color correlated with infrared luminosity, and infrared luminosity uncorrelated with blue luminosity. The quiescent component has lower infrared luminosity, a narrow range of 25/60 μm and 12/100 μm colors, warm 12/25 μm and cold, almost cirrus-like 60/100 μm colors, 60/100 μm color uncorrelated with infrared luminosity, and infrared luminosity correlated with blue luminosity.

The quiescent constituent is readily explained as the infrared emission arising from processes normally occurring in the disks of spiral galaxies: the heating of dust by ambient starlight, which gives rise to infrared cirrus emission, and star formation in spiral arms, which causes the warmer emission from dust in and around H II regions. The small range

of IR and IR/blue colors displayed by these objects is a consequence of relatively minor variations in the ratio of recent to current star formation rates among most normal spirals (Kennicutt 1983).

The nature of the IR-active component may differ from one galaxy to the next, and further study of individual objects is needed to clarify this point (see Chapter 3, Section V.A). However, the overall similarity of the behavior of Seyfert and morphologically peculiar galaxies in a variety of color-color and color-luminosity diagrams suggests a certain amount of common phenomenology, e.g. a common source geometry consisting of a centrally heated dust shell. Furthermore, the existence of an IR color-color (Figure 3-5) and IR color-luminosity relation (Figure 3-3), which spans a broad range of spectral shapes and is similar for the Seyfert and peculiar galaxies (and apparently unique to them), favors a single source with a range of physical parameters, rather than the superposition of many identical sources, i.e. star formation complexes such as those seen in normal galactic disks.

It is therefore reassuring to note that the super-luminous IR source is confined to the close vicinity of the nucleus in many well-studied galaxies which are dominated by an "active" IR component (e.g. NGC 1068, NGC 7469, Mkn 231, NGC 6240, IC 4553 [Telesco, Becklin, and Wynn-Williams 1980; Cutri et al. 1984; Matthews et al. 1987; Rieke et al. 1985; Becklin and Wynn-Williams 1987])). This trend is not confined to Seyfert galaxies and LINERs but also manifests itself in interacting galaxies which do not contain active nuclei per se as well. Bushouse (1987) studied a sample

of non-Seyfert spiral galaxies selected for optically disturbed morphology indicative of interactions and concluded that "interaction-induced star formation activity is concentrated near the nuclei of galaxies, and the disk regions usually experience only modest enhancements in the level of star formation activity."

These factors lead us to consider in more detail the role played by nuclear activity in determining the infrared spectral characteristics of galaxies. We use the term nuclear activity¹ to mean any process which is confined to a small (compared to the galaxy disk) central region of a galaxy but which produces greater or comparable luminous power to the galaxy itself. The usefulness of the concept of nuclear activity, thus broadly defined, for explaining the infrared spectral properties of galaxies will become apparent as we proceed.

In Section II we present observations carried out on a large subset of the IBGS, which we will use in conjunction with the data presented in Chapter 3 to examine the role of nuclear activity in IBGS galaxies. In Section III we derive and discuss two parameters used to quantify nuclear activity, the compactness parameter, R' , and the concentration parameter, k . In Section IV we present various relationships between these parameters and other measurables and discuss their physical implications. Our conclusions are summarized in Section V.

¹The terms active nucleus and nuclear starburst are used to delineate different types of nuclear activity, more than one of which may be present in a given galaxy).

II. Observations

A. 10 μm Photometry

The Steward Observatory 61" telescope in the Catalina Mountains was used to observe 16 objects in the IBGS at 10 μm . Aperture diameters of 5"5 or 8"5 were used with chopper throws of 10" to 13". A lock-in amplifier with a chopper frequency of 15 Hz was employed, and the telescope was wobbled every 15 seconds during the observations. Instrumental magnitudes were reduced to flux densities at 10.6 μm using the calibration of Rieke, Lebofsky, and Low (1985). Photometry for 33 additional objects, which was performed using the same or similar instrumentation either at Steward Observatory or at the NASA Infrared Telescope Facility on Mauna Kea was obtained from the literature. The data are summarized in Table 4-1.

All of the ground based measurements summarized in Table 4-1 were performed with apertures between 5" and 8"5 using either the Steward Observatory or the IRTF N filter. These filters are virtually identical, having an effective wavelength of 10.6 μm and a width at 50% transmission of 2.8 μm (Rieke, Lebofsky, and Low 1985). Thus differences in calibration are expected to be insignificant compared to the sources of error discussed below. The errors given in Table 4-1 are the standard error in the mean based on the root mean square deviation of samples which entered into the average. For 21 objects with multiple measurements, Table 4-1 lists the inverse-variance weighted mean and its associated error. However, agreement among various authors on measurements of the

same object is not always what it should be, despite the claim of Devereaux (1987) to the contrary.

Figure 4-1 is a histogram of differences among various $10\ \mu\text{m}$ measurements cited in this work normalized by the formal error in the difference. Nearly one third of those objects with multiple measurements have discrepancies between 2 and 5 times the computed errors. The seriousness of the disagreements can be judged from Figure 4-2, which shows them as a percentage of the weighted mean flux estimate. Sources of the discrepant measurements are shown beneath the object names in the figure. Only 2σ detected sources with discrepancies of 1.5σ or larger are included in the plot, which reveals non-negligible systematic errors from 50% to 200% of the weighted mean flux estimates in seven sources. This fact is discouraging but hardly surprising in view of the extreme difficulty with which N band photometry is obtained.

We have considered the possibility that different aperture sizes might account for some of the discrepancies shown in Figure 4-2. Over the small range of aperture sizes considered here, we would expect a $10\ \mu\text{m}$ nuclear source to obey $F_{10} \sim A^\gamma$ with $0 \leq \gamma \leq 2$. This will hold for the value of γ derived from any pair of apertures, A_1 and A_2 , provided only that the azimuthally averaged radial flux distribution is monotonically decreasing, point-like, or uniform. We have computed values of $\gamma = \log(F_1/F_2)/\log(A_1/A_2)$ for all seven of the flux discrepancies exceeding 1.5σ , and we find that two of them are within the allowable range of 0 to 2. These are NGC 1614 ($\gamma=1.1$) and NGC 3079 ($\gamma=1.9$). In light of the

remaining five discrepancies, for which γ is either negative or significantly greater than 2, the possibility that the values of γ for NGC 1614 and NGC 3079 are ascribable to coincidence cannot be discounted.

Ten Micron variability is extremely unlikely to explain these disagreements among various authors. Four of the seven objects plotted in Figure 4-2 have unambiguous H II region nuclei (see below), while NGC 5005 and NGC 3079 are type 2 Seyferts, and NGC 4654 has not been classified. H II region nuclei tend to have very similar spectra near 10 μm , including features at 8.65 μm , 9.7 μm , and 11.25 μm due to dust (Phillips, Aitken, and Roche 1984). A source consisting of dust grains warmed by early type stars would not be expected to vary appreciably in less than a few million years. Because of their cold, curved infrared spectra, type 2 Seyferts are also believed to be powered by dust near 10 μm (e.g. Rieke 1978; Edelson and Malkan 1986; Rieke and Lebofsky 1979). A dust grain with a typical Planck averaged emissivity of 0.1 heated by a $10^{44} \text{ erg s}^{-1}$ UV power source attains a temperature of 300 K at a distance of $\sim 2 \text{ pc}$ and thus a source of this kind could not vary on timescales of less than $\sim 6 \text{ years}$. This consideration is sufficient to eliminate variability as the explanation for the discrepancy in measurements of NGC 3079 by Edelson, Malkan, and Rieke (1987) and Devereaux, Becklin, and Scoville (1987). Furthermore, Edelson and Malkan (1987), in a search for far-infrared variability among active galactic nuclei, found no cases of variability at 12 μm during the course of the IRAS mission in any type 2 Seyfert.

The errors are probably caused by differences in telescope pointing and optical alignment errors within the photometers. These observations are almost always carried out during bright time, making visual acquisition of the object exceedingly difficult, even for galaxies as bright as $B_T \sim 12$. Furthermore, both the Steward and IRTF germanium bolometers are subject to flexure, which necessitates adjusting the optical alignment each time the telescope is slewed a significant distance (this work; Devereaux 1987). Finally, there is always the possibility that the $10 \mu\text{m}$ nuclear source does not coincide with the optically brightest point due to internal extinction.

These sources of error are much more likely to affect the observations of the objects than the standard stars, which provides a means of testing the hypothesis that they explain the discrepancies we are discussing. This test was carried out by means of a comparison of the sensitivity deduced from various standard stars observed on the same night during the course of this work. The rms deviations of the instrumental sensitivity² for each observing night are given as a percentage of the mean sensitivity in Table 4-2. The differences are always $\lesssim 20\%$ and can be plausibly attributed to differences in airmass and background level, leading to actual variations in sensitivity.

Unassailable nuclear $10 \mu\text{m}$ photometry for the galaxies in Table 4-1 will probably not exist until $10 \mu\text{m}$ imagery becomes more widely available,

²Instrumental sensitivity is defined as net counts per second due to a zero N magnitude source observed with unit amplifier gain.

or until a new generation photometers free from flexure can be used with object coordinates and telescope pointing that are in sub-arcsecond agreement. In the mean time, the accuracy of the data in Table 4-1, while not all that we could wish for, is sufficient for our purpose, which is to distinguish those objects containing compact nuclear infrared sources whose luminosity is greater than or comparable to the infrared luminosity of the host galaxy.

Since pointing and alignment errors are most likely to affect the objects rather than the standard stars and since we are interested in the strongest compact infrared source in the galaxy, regardless of its location, the higher measurement is likely to be best for our purpose in most cases of disagreement. Nonetheless we have used a weighted average of the fluxes cited in all cases. This was done in order to avoid biasing the results toward exaggerated nuclear infrared sources. The aperture and chopper throw listed for weighted average measurements are also weighted averages. Since two thirds of the objects in Figure 4-1 have discrepancies of less than twice the formal errors, we shall use twice the formal error given in Table 4-1 as a rough approximation to the uncertainty in the nuclear $10\ \mu\text{m}$ fluxes in what follows.

Figure 4-1
Discrepancies in Ten Micron Flux Measurements

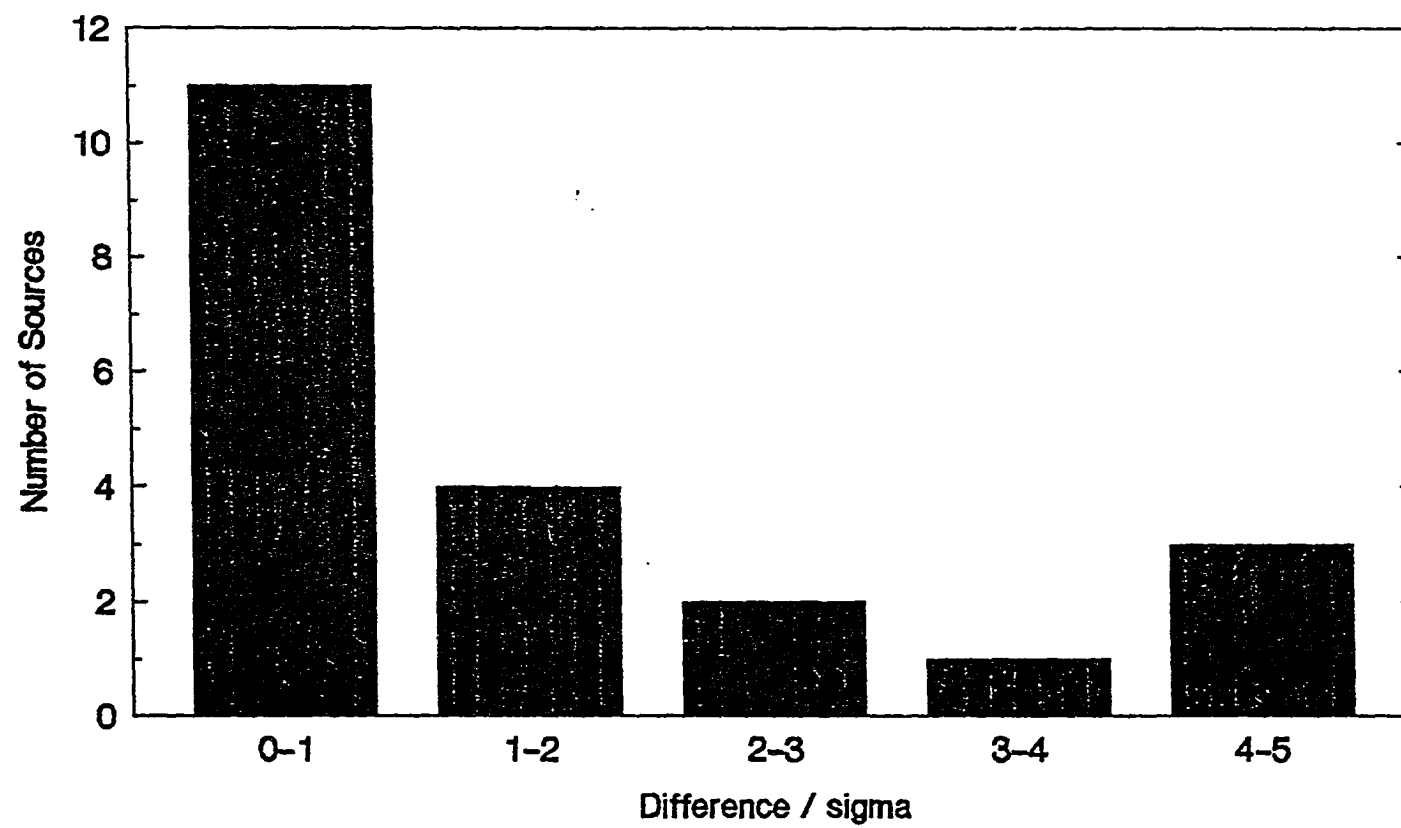


Figure 4-2
Percentage Error Due to
Ten Micron Flux Discrepancies

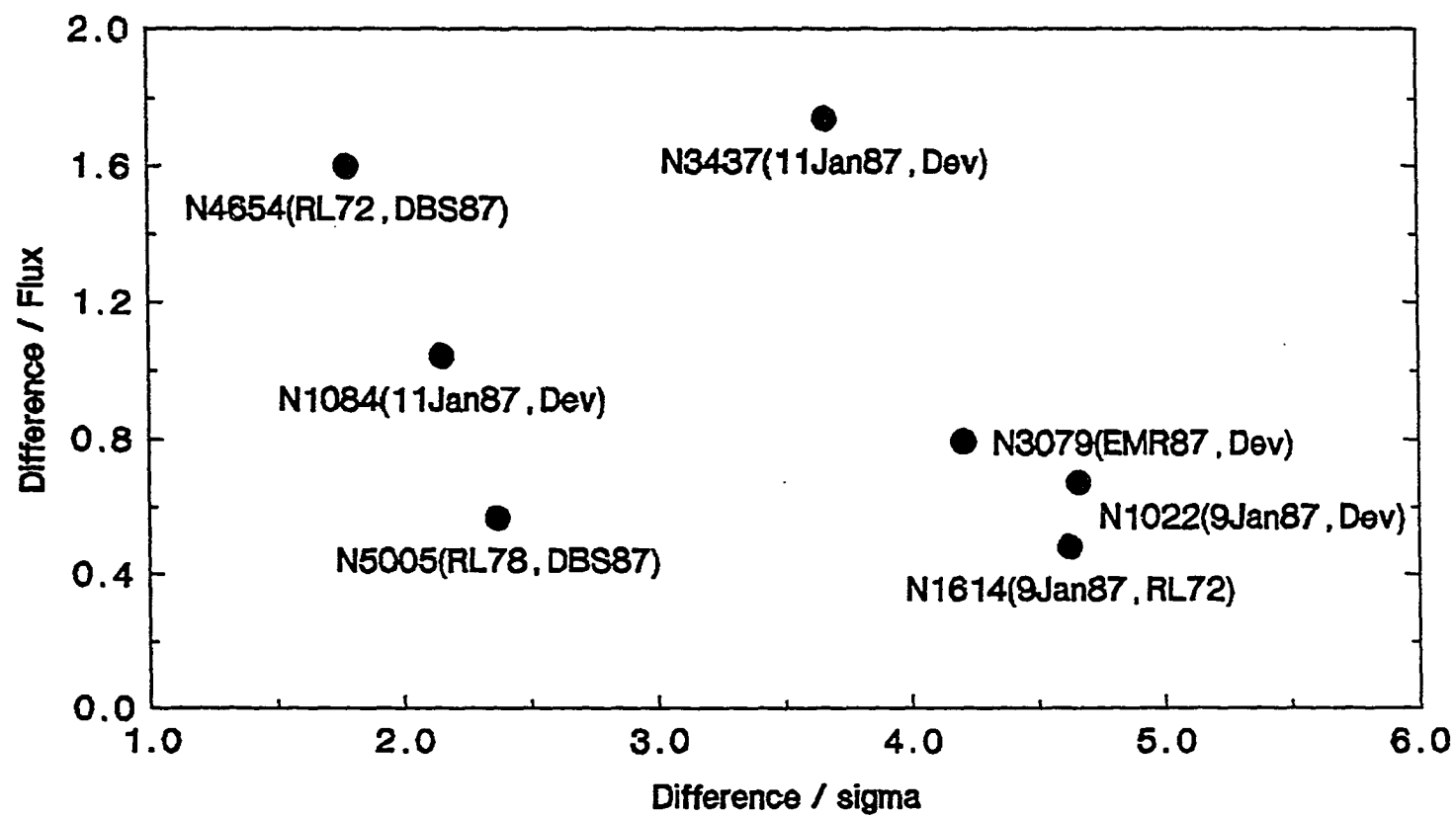


Table 4-1
10 Micron Nuclear Measurements of IBGS Objects

Name	F_{10}^a	σ_{10}^{bc}	Ap	Throw	References ^{de}
NGC 157	0.017	0.024	5"5	30"0	Dev
NGC 828	0.215	0.061	8.5	10.0	20Oct85
NGC 972	0.139	0.029	8.5	13.0	10Jan87
NGC 1022	0.321	0.020	6.2	25.8	9Jan87, Dev
NGC 1055	0.071	0.044	8.5	13.0	11Jan87
NGC 1068	18.000	2.700	5.7	8.6	R78
NGC 1084	0.059	0.014	6.9	22.3	11Jan87, Dev
NGC 1222	0.110	0.031	8.5	13.0	8, 10, 13Jan87
NGC 1614	0.761	0.033	6.3	2.8	9Jan87, RL72
NGC 2964	0.127	0.012	6.5	24.6	11Jan87, Dev
NGC 3079	0.151	0.014	7.0	20.0	EMR87, Dev
NGC 3094	0.113	0.026	8.5	13.0	11Jan87
NGC 3437	0.070	0.011	6.1	26.6	8, 11Jan87, Dev
NGC 3504	0.402	0.012	5.5		RL72, Dev
NGC 3593	0.154	0.053	8.5	12.0	30Mar87
NGC 3683	0.057	0.022	5.5	30.0	Dev
NGC 3810	-0.001	0.015	5.5		DBS87
NGC 3893	0.034	0.013	6.1	26.4	10Jan87, Dev
NGC 4030	0.042	0.014	6.0	27.3	11Jan87, 31Mar87, Dev
NGC 4038	0.217	0.061	8.5	12.0	1Apr87
NGC 4041	0.023	0.019	5.7	28.8	29Mar87, Dev
NGC 4088	0.023	0.017	5.5	30.0	Dev
NGC 4102	0.744	0.024	5.5	30.0	Dev
NGC 4157	0.010	0.025	5.5	30.0	Dev
NGC 4194	0.376	0.028	5.5	30.0	Dev
NGC 4214	0.000	0.043	5.7	8.0	RL78
NGC 4254	-0.003	0.015	5.5		RL78, DBS87
NGC 4303	0.079	0.011	5.6		RL78, DBS87
NGC 4321	0.034	0.010	5.5		RL78, DBS87
NGC 4388	0.404	0.016	5.5		DBS87
NGC 4501	0.012	0.014	5.6		RL78, DBS87
NGC 4527	0.126	0.019	5.5	30.0	Dev
NGC 4536	0.222	0.012	5.6		RL78, DBS87
NGC 4654	0.035	0.014	5.6		RL72, DBS87
NGC 4691	0.113	0.015	5.5	30.0	Dev
NGC 4793	0.028	0.012	5.5	30.0	Dev
Mkn 231	1.420	0.213	5.7		R78
NGC 4818	0.544	0.020	5.5	30.0	Dev
NGC 4984	0.310	0.023	5.5	30.0	Dev
NGC 5005	0.092	0.011	5.6		RL78, DBS87
NGC 5054	0.069	0.014	5.5	30.0	Dev

Table 4-1
(continued)

Name	F_{10}	σ_{10}	Ap	Throw	References
Mkn 273	0.098	0.023	5.7	8.6	R78
NGC 5676	-0.013	0.017	5.5	30.0	Dev
NGC 5775	0.030	0.012	5.5	30.0	Dev
IC 4553	0.198	0.010	5.8	10.0	Retal85
NGC 6240	0.252	0.010	5.8	10.0	Retal85
NGC 7469	0.600	0.090	5.7	8.6	R78
NGC 7479	0.305	0.028	5.5	30.0	Dev
Mkn 331	0.046	0.107	8.5	13.0	20Oct85

Notes to Table 4-1

a. Weighted mean fluxes and flux errors are given in Janskys. Rieke and Lebofsky (1978; RL78) 2σ upper limits have been arbitrarily replaced by a measured value of zero and an error of one half the limit value.

b. This is the formal 1σ error in the weighted mean of all measurements and does not include systematic differences between them. Actual uncertainties are on average about twice this value; see the text.

c. $10.6 \mu\text{m}$ fluxes from Rieke (1978; R78) have been assigned a nominal error of 15% as recommended therein.

d. Dates are the dates of my own observations using the Steward Observatory 61" Catalina telescope. Other measurements are as follows: DBS87: Devereaux, Becklin, and Scoville (1987); Dev: Devereaux (1987); EMR87: Edelson, Malkan, and Rieke (1987); Retal85: Rieke et al. (1985); R78: Rieke (1978); RL72: Rieke and Low (1972); RL78: Rieke and Lebofsky (1978).

e. Rieke and Low (1972; RL72) measurements were corrected to the $10 \mu\text{m}$ calibration of Low and Rieke (1974) by multiplication by 0.74 as recommended by Low and Rieke (1974). The Low and Rieke zero point of 36.4 Jy is in reasonable agreement with the Rieke, Lebofsky, and Low (1986) value of 36.0, although differences in assumed standard star magnitudes render the exact relationship between various authors problematic and standard star dependent. The correction factor of 0.74 was applied to the RL72 data because (as noted by Rieke and Lebofsky [1978; RL78]) it agrees well with the average ratio of ten common measurements between RL78 and RL72. That ratio is 0.71 ± 0.07 . One galaxy, NGC 5457 was thrown out before taking the average due to flux estimates which were discrepant by 3.7σ .

Table 4-2
Nightly 10.6 μm Sensitivity Variations

Date	Percent Variation	Number of stars
20Oct85	3.7%	2
30Sep85	19.9%	2
9Jan87	10.8%	4
10Jan87	0.01%	2
11Jan87	22.5%	4
13Jan87	...	1
29Mar87	...	1
30Mar87	...	1
31Mar87	...	1
1Apr87	2.1%	2

B. Optical Spectroscopy

Optical spectra of 28 IBGS galaxies for which 10 μm photometry is given in Table 4-1 were obtained on the nights of 12 and 23 October 1985, 7-8 December 1985, and 22-23 April 1987. The Steward Observatory 90" telescope was used with the Boller and Chivens spectrograph. A 600 mm^{-1} grating and two 5" circular apertures with 25" separation were used giving a resolution of approximately 7 Å. The telescope was wobbled between the two apertures every four minutes during the observations, which lasted from 16 to 64 minutes. The detector consisted of a blue sensitive Carnegie image tube, gain stage, and two 1024 element Reticon pulse counting arrays. Filters having 50% transmission at 3600 Å (1985 observations) and 3800 Å (1987) were used to block second order light.

The objects observed, date of observation, and whether or not the data were obtained under photometric conditions are given in Table 4-3.

Table 4-3
Spectroscopy of IBGS Galaxies

Name	Date	Conditions
NGC 157	23Oct85	Photometric
NGC 828	23Oct85	Photometric
NGC 972	23Oct85	Photometric
NGC 1022	12Oct85	Photometric
NGC 1055	23Oct85	Photometric
NGC 1084	23Oct85	Photometric
NGC 1222	12Oct85	Photometric
NGC 1614	23Oct85	Photometric
NGC 2964	7Dec85	Photometric
NGC 3079	8Dec85, 22Apr87	Variable Clouds
NGC 3094	8Dec85	Variable Clouds
NGC 3437	8Dec85	Photometric
NGC 3504	22Apr87	Photometric
NGC 3683	22Apr87	Photometric
NGC 3810	23Apr87	Variable Clouds
NGC 3893	22Apr87	Photometric
NGC 4030	23Apr87	Variable Clouds
NGC 4038	23Apr87	Variable Clouds
NGC 4041	23Apr87	Photometric
NGC 4088	23Apr87	Photometric
NGC 4157	22Apr87	Photometric
NGC 4194	23Apr87	Photometric
NGC 4793	23Apr87	Photometric
Mkn 273	23Apr87	Photometric
NGC 5676	22Apr87	Photometric
NGC 5775	22Apr87	Photometric
IC 4553	23Apr87	Photometric
NGC 6240	22, 23Apr87	Photometric

The emission line fluxes and H α equivalent width for those objects with measurable emission are given in Table 4-4. Eight objects from Table 4-3 not appearing in this table had no measurable emission features due to

spectra dominated by stellar absorption. Weak H α emission was discernable in most cases.

The spectroscopic data were reduced except for flux calibration and measurement of emission lines using Steward's Interactive Reduction System. Flux calibration and emission line measurement were carried out on version 2.6 of the National Optical Astronomy Observatory's Image Reduction and Analysis Facility at Steward Observatory.

Table 4-4
Emission Line Fluxes for IBGS Galaxies

Name	[O II] λ 3727.3	H γ 4340.5	H δ 4861.3	[O III] 4958.9	[O III] 5006.8	He I 5875.6	[N II] 6548.1	H α 6562.8	[N II] 6583.4	W_{λ} (H α)
NGC 972	7.03-15	...	9.14-15	6.00-15	1.22-14	...	1.87-14	1.09-13	5.11-14	25
NGC 1022	2.80-14	7.17-15	3.72-14	...	8.91-15	...	4.23-14	3.07-13	1.47-13	68
NGC 1084	1.19-14	...	1.55-14	1.58-14	1.14-13	7.18-14	28
NGC 1222	3.01-13	...	1.98-13	1.78-13	5.35-13	3.62-14	7.54-14	1.14-12	2.59-13	173
NGC 1614	6.51-14	3.29-14	1.07-13	2.83-14	7.77-14	...	1.88-13	9.51-13	6.16-13	199
NGC 2964	1.67-14	8.20-15	2.40-14	...	6.14-15	...	2.76-14	1.56-13	6.20-14	56
NGC 3079	8.54-15	1.43-15	...	3.26-15	7.63-15	1.29-14	5
NGC 3094	1.16-14	...	7.38-15	1.05-15	3.47-15	...	1.01-14	4.83-14	2.46-14	20
NGC 3437	1.27-14	7.14-15	2.25-14	1.95-14	1.03-13	4.96-14	36
NGC 3504	6.88-14	3.60-14	1.28-13	3.68-14	8.39-14	...	1.70-13	7.38-13	4.48-13	54
NGC 3683	1.06-14	3.31-14	1.15-14	...	13
NGC 3893	5.65-15	2.93-14	1.40-14	...	9
NGC 4038	...	7.56-15	1.36-14	...	3.77-15	...	2.34-14	1.68-13	7.12-14	105
NGC 4041	3.59-15	6.45-15	3.99-14	1.67-14	16
NGC 4088	1.89-15	1.97-15	5.07-15	2.93-14	7.70-15	31
NGC 4157	1.26-15	2.04-14	7.38-15	12
NGC 4194	8.80-14	2.96-14	9.92-14	3.36-14	1.17-13	1.65-14	1.44-13	8.05-13	4.03-13	138
Mkn 273	2.40-14	2.20-15	8.51-15	1.15-14	3.04-14	43
IC 4553	7.60-15	1.37-14	9
NGC 6240	1.78-14	1.59-15	1.03-14	6.73-15	1.77-14	...	8.09-14	2.03-13	2.43-13	111

The blue [O III] $\lambda\lambda 4959, 5007$ and red [N II] $\lambda\lambda 6548, 6583$ lines provide a convenient measure of the accuracy of the data in Table 4-4, since their measured ratio can be compared to the intrinsic ratio, which is fixed independent of physical conditions in the nebula. This is because both pairs of lines arise from radiative decay of a single upper level, which gives rise to a flux ratio equal to the ratio of their Einstein A values. Based on these line ratios, we assign an uncertainty of 10% to lines with $\lambda < 6000$ Å and flux greater than 4.5×10^{-14} erg cm $^{-2}$ s $^{-1}$ and 20% to lines with $\lambda > 6000$ Å and flux greater than 1.0×10^{-13} erg cm $^{-2}$ s $^{-1}$. Lines fainter than these limits should be assigned errors of 20% ($\lambda < 6000$ Å) and 40% ($\lambda > 6000$ Å).

These data have been used to classify the nuclear spectra of many IBGS galaxies for which 10 μ m photometry is available. Galaxies with measurable emission lines have been classified on the system of Veilleux and Osterbrock (1987) using the $\lambda 5007/H\beta$, $\lambda 6583/H\alpha$, and $(\lambda 6716 + \lambda 6731)/H\alpha$ emission line ratios. The classifications are listed in Table 4-5; and Figure 4-3, which is similar to Figure 1 of Veilleux and Osterbrock, plots the two line ratios used for most of the classifications. Data for NGC 1068 is taken from Koski (1978), and data for Mkn 273 has been averaged with Koski's data. The solid curve in Figure 4-3 separates regions of the diagram populated by active nuclei and by H II regions (Veilleux and Osterbrock 1987). The meaning of the symbols in Table 4-5 is as follows. H: H II region nucleus photoionized by young stars; L: low ionization nuclear emission region (LINER [Heckman 1980]); T: transition between

types H and L; 1: type 1 Seyfert; 2: type 2 Seyfert; A: absorption features dominate the nuclear spectrum. A few of the individual classifications are discussed below.

Table 4-5
Classification of the Nuclear Spectrum of IBGS Galaxies

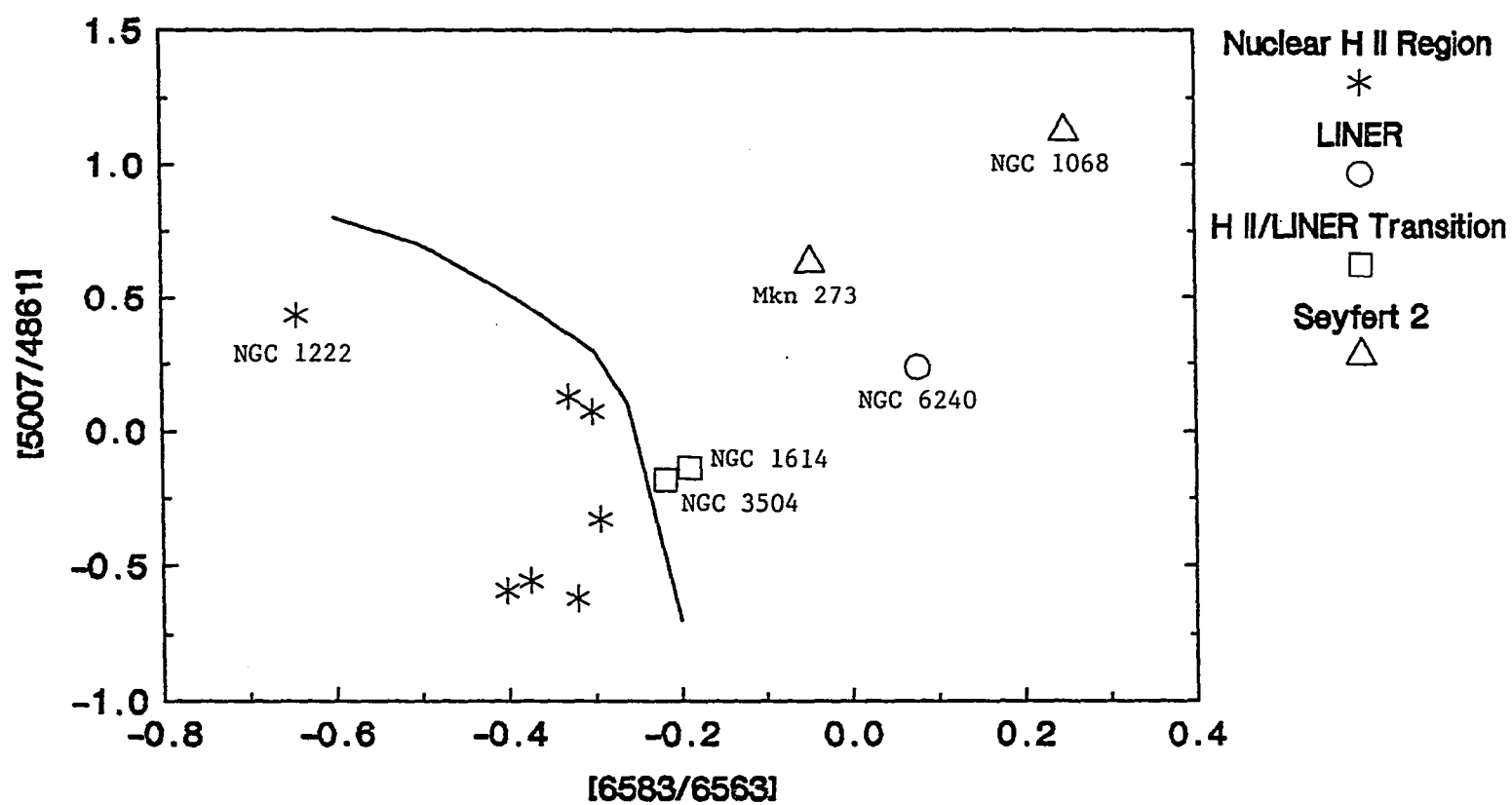
Name	Classification
NGC 157	A
NGC 828	A
NGC 972	H
NGC 1022	H
NGC 1055	A
NGC 1068	2
NGC 1084	H
NGC 1222	H
NGC 1614	T
NGC 2964	H
NGC 3079	2
NGC 3094	H
NGC 3437	H
NGC 3504	T
NGC 3683	H
NGC 3810	A
NGC 3893	H
NGC 4030	A
NGC 4038	H
NGC 4041	H
NGC 4088	H
NGC 4157	H
NGC 4194	H
NGC 4793	A
Mkn 231	1
Mkn 273	2
NGC 5676	A
NGC 5775	A
IC 4553	2
NGC 6240	L
NGC 7469	1

Mkn 273 lies in a portion of Figure 4-3 populated sparsely by both type 2 Seyferts and LINERs. My classification of it as a Seyfert is based on detection of He II $\lambda 4686$ emission by myself and Koski (1978). Detection of this line requires a significant flux of photons more energetic than 4 Ry from the ionizing source, which is strongly indicative of Seyfert activity. The line is never seen in LINERs or H II region nuclei.

The classification of NGC 3079 as a type 2 Seyfert is taken from Edelson, Malkan, and Rieke (1987) and is consistent with the $\lambda 6583/H\alpha$ ratio and $\lambda 5007/H\beta$ lower limit from my spectrum. Note, however, that this object shows the weakest emission of any object not classified as type A and that both its IRAS color and its 11 μm compactness parameter indicate that the host galaxy's disk dominates nuclear emission in the infrared (Edelson, Malkan, and Rieke; Section IV).

The classification of IC 4553 (Arp 220) as a type 2 Seyfert is taken from Rieke et al. (1985) and is consistent with the $\lambda 6583/H\alpha$ ratio and $\lambda 5007/H\beta$ lower limit from my spectrum. The classification of NGC 1084 is taken from Keel (1983). The uncontroversial classifications of Mkn 231 and NGC 7469 are taken from Chapter 3.

Figure 4-3
Nuclear Emission Line Classification



III. The Compactness Parameter

A. Derivation

The N filters used for 10.6 μm photometry are broad enough (2.8 μm) to provide a reasonable estimate of the average continuum in the 9-12 μm region, despite the complexity of galaxy spectra there. The full width at 50% transmission of the IRAS 12 μm filter is 7.1 μm , wide enough to completely contain the N bandpass. Thus it is reasonable, after applying a suitable correction factor to both fluxes, to treat them as measures of flux density at a single wavelength taken through unequal apertures.

In order to convert the N photometry to a monochromatic flux at 11 μm , it is necessary to multiply by 1.22 (Edelson, Malkan, and Rieke 1987). For comparison, the color corrected total 12 μm and 25 μm fluxes given for IBGS galaxies in Chapter 3 were extrapolated to 11 μm using a power law with the source's average spectral index between 12 μm and 25 μm ($\alpha_{12,25}$). The ratio, R , of the small aperture 11 μm flux to the total 11 μm flux thus derived is referred to below as the compactness parameter. Compactness parameters and error estimates are given for 49 of the 70 IBGS galaxies in Table 4-6. The error in R has been computed assuming a 15% uncertainty in the total IRAS fluxes from Chapter 3 and using twice the errors in Table 4-1 as an estimate of the uncertainty in the 10 μm flux. Values of R less than twice the corresponding error estimate have been replaced with a 2σ upper limit.

Galaxies with compactness parameters near 1 are dominated in the 9-12 μm region by a compact nuclear source, while those with compactness parameter near 0 are dominated by disk emission at these wavelengths. This inference is based on the fact that the apertures used for the 10 μm measurement (5"-8") are much smaller than the galaxy diameters, which range from 1' to 8'. Sensitivity to disk emission in the N photometry is further reduced by the small chopper throws (10"-30").

B. Biases in the Compactness Parameter

The compactness parameter is subject to two sources of systematic error. First, the 9.7 μm silicate absorption feature seen in the spectra of most galaxies with H II region nuclei removes a greater percentage of the total flux from the smaller bandpass N filter than it does from the IRAS 12 μm feature. This problem has been discussed by Devereaux (1987), who notes that, for a typical galaxy having an H II region nucleus, the value of R will be underestimated by $\lesssim 28\%$, while in the worst case an error of a factor of two may result. Seyfert galaxies generally show silicate absorption less than or comparable to that in galaxies with H II region nuclei (Roche et al. 1984). Thus the compactness parameters given in Table 4-6 cover a much larger range than could be explainable by varying amounts of silicate absorption. Furthermore, extreme cases of silicate absorption may cause us to classify a galaxy containing a moderate nuclear source as disk-dominated but cannot cause the opposite error. Since galaxies that are not nuclear-dominated at 11 μm are known

to be rather common (Rice et al. 1988; Chapter 3 Sections IV. A and B), we are confident that the comparisons below between galaxies with compact nuclear sources and those without are well-founded.

A further check on the effect of silicate absorptions on the compactness parameter can be made using the emission line fluxes in Table 4-4. One would expect the depth of the silicate feature to be correlated with the reddening of nuclear emission lines. In that case, a plot of the compactness parameter against the dust optical depth determined from the optical emission lines should reveal any bias toward lower compactness parameters in highly reddened sources. Dust optical depths at 4861.3 Å, $\tau_{H\beta}$, are derived for several of the galaxies appearing in Table 4-1 in Appendix A using data from Table 4-4. These values are plotted against the compactness parameter, R , in Figure 4-7. There is no evidence of a correlation. Plainly the intrinsic variations in small to large aperture flux are large enough to overwhelm the comparatively small variations in flux removed by silicate absorption in these objects.

The second systematic error in the compactness parameter is that use of a fixed aperture size to measure the nuclear flux results in a bias toward higher compactness parameters for sources of small angular diameter, which tend to be those with higher redshifts and luminosities. Figure 4-7 is a graph of the compactness parameter versus A/D , the ratio of the aperture size used in the N measurement to the total galaxy diameter. The 25th magnitude B isophotal diameter, D_{25} , from Table 3-4 was used for this purpose. An apparent bias exists in the form of a

progressively larger minimum compactness parameter at larger values of A/D . This is the sort of bias that would be expected from the superposition of a compact nuclear source and a source the size of the host galaxy's disk viewed at varying values of A/D . The minimum compactness parameter at any value of A/D is simply the fraction of the disk source flux contained in the aperture, while positive deviations by various amounts result from nuclear sources of varying strength.

We have corrected for this effect in the following manner. The observed compactness parameter may be written

$$\begin{aligned} R &= \frac{L_{\text{disk}}(A/D) + L_{\text{nucleus}}}{L_{\text{total}}} \\ &= \frac{L_{\text{disk}}(A/D)}{L_{\text{total}}} + R' \end{aligned}$$

where $R' = L_{\text{nucleus}}/L_{\text{total}}$ is the corrected compactness parameter. Using $L_{\text{total}} = L_{\text{nucleus}} + L_{\text{disk}}(A/D=1)$, this becomes

$$R = \frac{L_{\text{disk}}(A/D)}{L_{\text{disk}}(A/D=1)} (1 - R') + R' \quad (1)$$

To estimate R' it is necessary to assume a functional form for $L_{\text{disk}}(A/D)/L_{\text{disk}}(1)$. To do this, the lower envelope of Figure 4-7 may be taken to represent the condition $R'=0$ and a suitable function fit to it. Assuming an exponential surface brightness law, such as that obeyed by the optical disks of galaxies (Mihalis and Binney 1981) leads to

$$\begin{aligned}
\frac{L_{\text{disk}}(A/D)}{L_{\text{disk}}(A/D=1)} &= \frac{\int_0^{A/D} 2\pi x \sigma e^{-kx} dx}{\int_0^1 2\pi x \sigma e^{-kx} dx} \\
&= \frac{1 - e^{-kx}(kx+1)}{1 - e^{-k}(k+1)} \quad (2)
\end{aligned}$$

where $x=A/D$, and σ and k parameterize the $11 \mu\text{m}$ surface brightness profile. Note that the final result does not depend on σ , the central surface brightness of the disk.

Reasonable agreement between equation (2) and the lower envelope of points in Figure 4-7 is obtained for values of k between 6 and 10. The value we have adopted, $k=8$, is the solid curve in Figure 4-7. The corrected compactness parameters, R' , thus derived are given in the last column of Table 4-6 and are plotted against A/D in Figure 4-7. In order to avoid any luminosity bias in our compactness parameters, the corrected value R' is used exclusively throughout the remainder of this chapter.

The parameter k in equation (2) represents the central concentration of an exponential disk model. It may be written as $D_{25}(\underline{B})/2r_0(11 \mu\text{m})$, where $D_{25}(\underline{B})$ is the 25th magnitude \underline{B} isophotal diameter and $r_0(11 \mu\text{m})$ is the scale length of the exponential disk at $11 \mu\text{m}$. Thus higher values of k yield disk models which are more centrally concentrated. Based on the bulge/disk \underline{V} band decompositions of spiral galaxies by Kodaira, Watanabe, and Okamura (1986), $\langle D_{25}(\underline{B})/2r_0(\underline{V}) \rangle = 3.73 \pm .25$. Boroson's (1981) \underline{B} band decompositions of spirals yield $\langle D_{25}(\underline{B})/2r_0(\underline{B}) \rangle = 3.26 \pm .27$, and his scale lengths agree well with those determined by Kent (1985) at \underline{r} . Cornell's

(private communication) \underline{B} decompositions yield $\langle D_{25}(\underline{B})/2r_0(\underline{B}) \rangle = 3.1 \pm 1$, consistent with an overall average of $k=3.5$ for optical spiral disks. A dashed line representing equation (2) with $k=3.5$ has been drawn on Figure 4-7 for comparison with the adopted ($k=8$) curve. It demonstrates that (1) spiral galaxies are significantly more compact in the infrared than in the optical, as noted by Rice et al. (1988); and/or (2) the correction to the compactness parameter adopted here probably overestimates the disk contribution to R , i.e. the corrected compactness parameters, R' , will be on average underestimated. The latter circumstance is easily understood if there is a genuine correlation between infrared luminosity and the presence of a compact nuclear infrared source, which, as we shall see, is actually the case. We adopt the value $k=8$ nonetheless, since the overly conservative correction will not significantly affect any of our conclusions.

Use of the corrected compactness parameter, R' , is somewhat unsatisfying, as it relies on a pair of unrealistic assumptions: (1) that all spiral galaxies possess an infrared exponential disk; and (2) that the concentration parameters, k , is the same in all cases. An alternative approach is to relax assumption (2) by recognizing the fact that two flux measurements of one object taken through different apertures are sufficient to determine a unique concentration parameter for that object. Trends with infrared compactness can then be detected by examining the relationship of other measurables to k .

This approach is also lacking in realism, as it ignores the fact that many infrared bright spirals (i.e. Seyfert galaxies and galaxies with compact nuclear starbursts) contain two distinct sources, one much more centrally concentrated and the other much less than a single value of k would indicate. For such sources R' , which assumes a small nuclear source superimposed on an exponential disk source, is a better indicator of the true nuclear source strength. However, use of the concentration parameter, k , represents a complementary approach in the sense that it suffers from the opposite bias to that which affects R' . Since the apertures used to measure the $10\ \mu\text{m}$ flux are a larger percentage of the total galaxy diameter, D_{25} , for the high redshift, luminous sources, a nuclear source containing a fixed fraction of the total infrared luminosity will result in a smaller value of k when seen at greater distance. This bias is demonstrated in Figure 4-7, which is a plot of k versus A/D for the galaxies listed in Table 4-6. The concentration parameters in Figure 4-7 were computed by setting the observed $11\ \mu\text{m}$ flux ratio, R , equal to the right hand side of equation (2) and solving for k by iteration. The concentration parameters are included in the last column of Table 4-6 and will be used as a check on the results obtained using R' in the next section.

Figure 4-4
Compactness Parameter vs. Nuclear Reddening

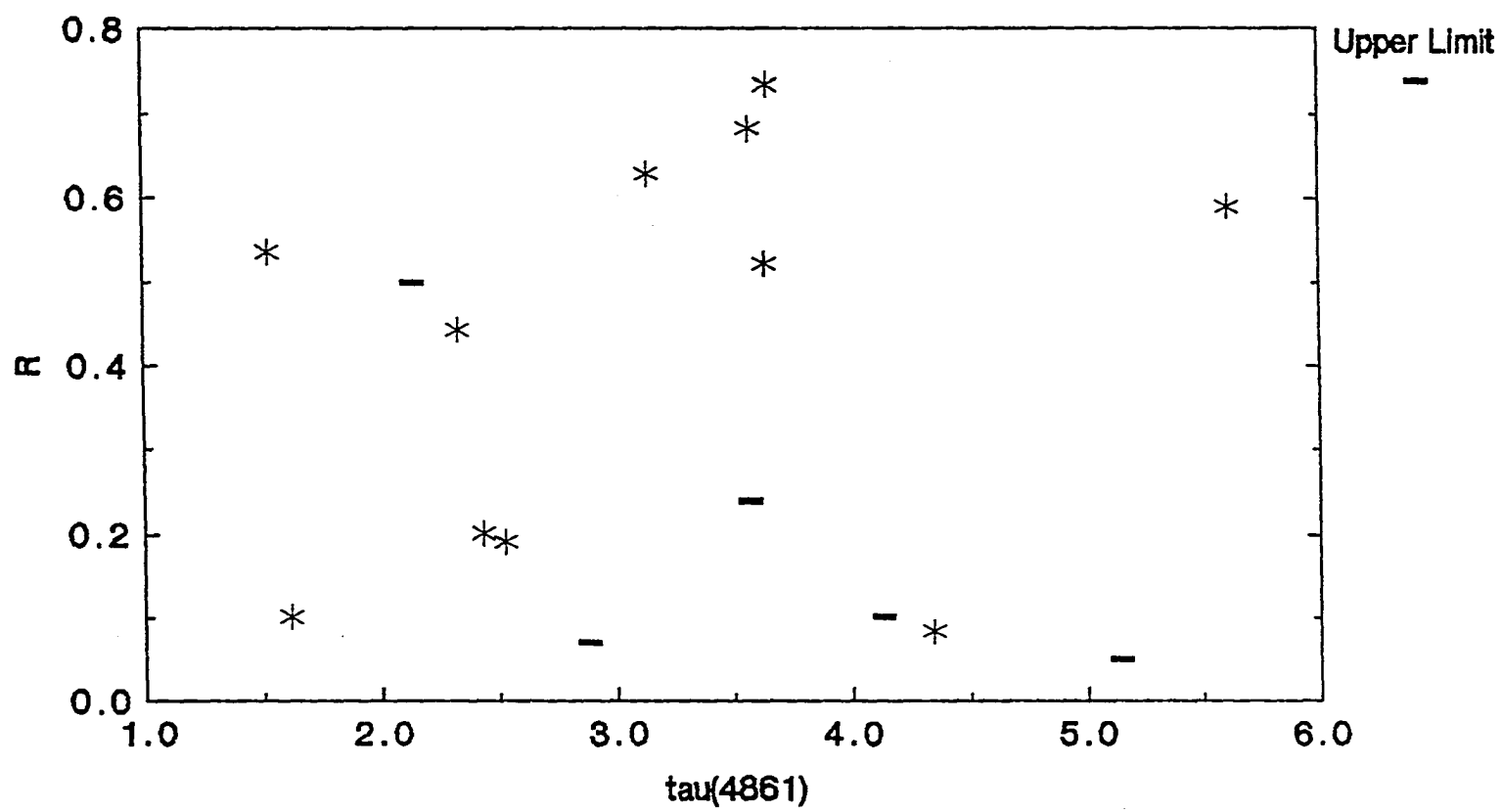


Figure 4-5
Compactness Paramter vs. Aperture/Diameter

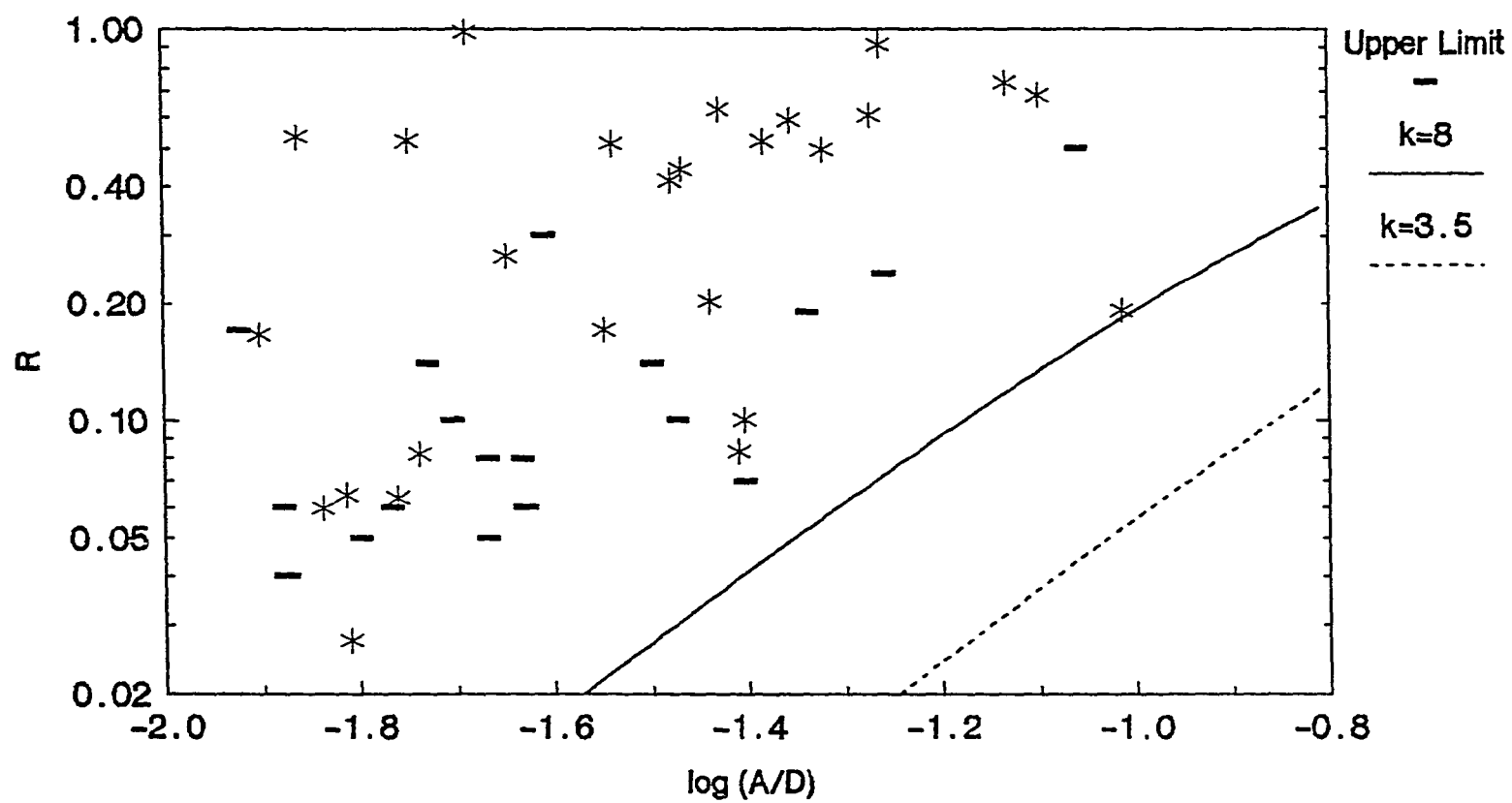


Figure 4-6
Corrected Compactness Parameter vs. A/D

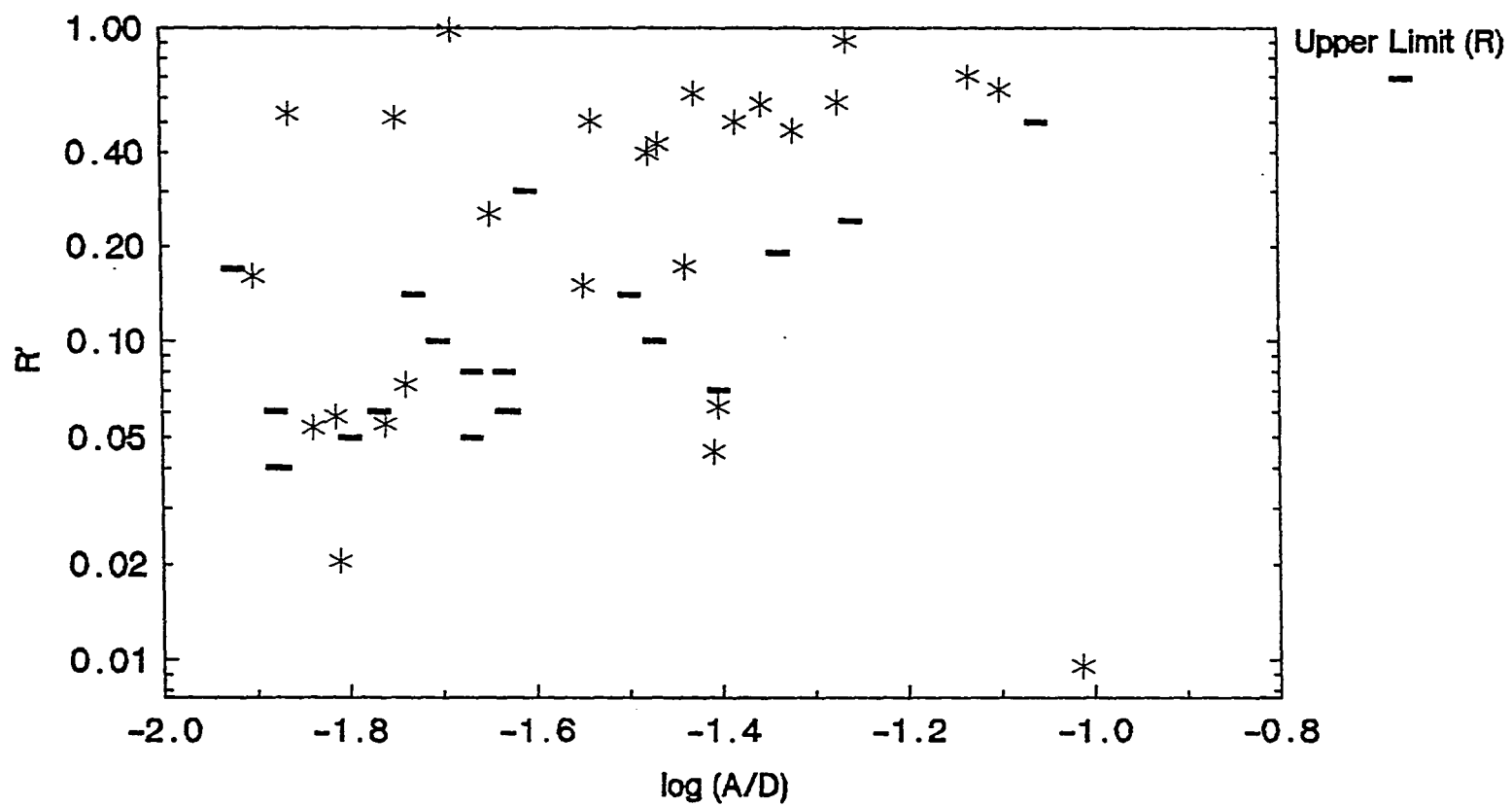


Figure 4-7
Concentration Paramter vs. Aperture/Diameter

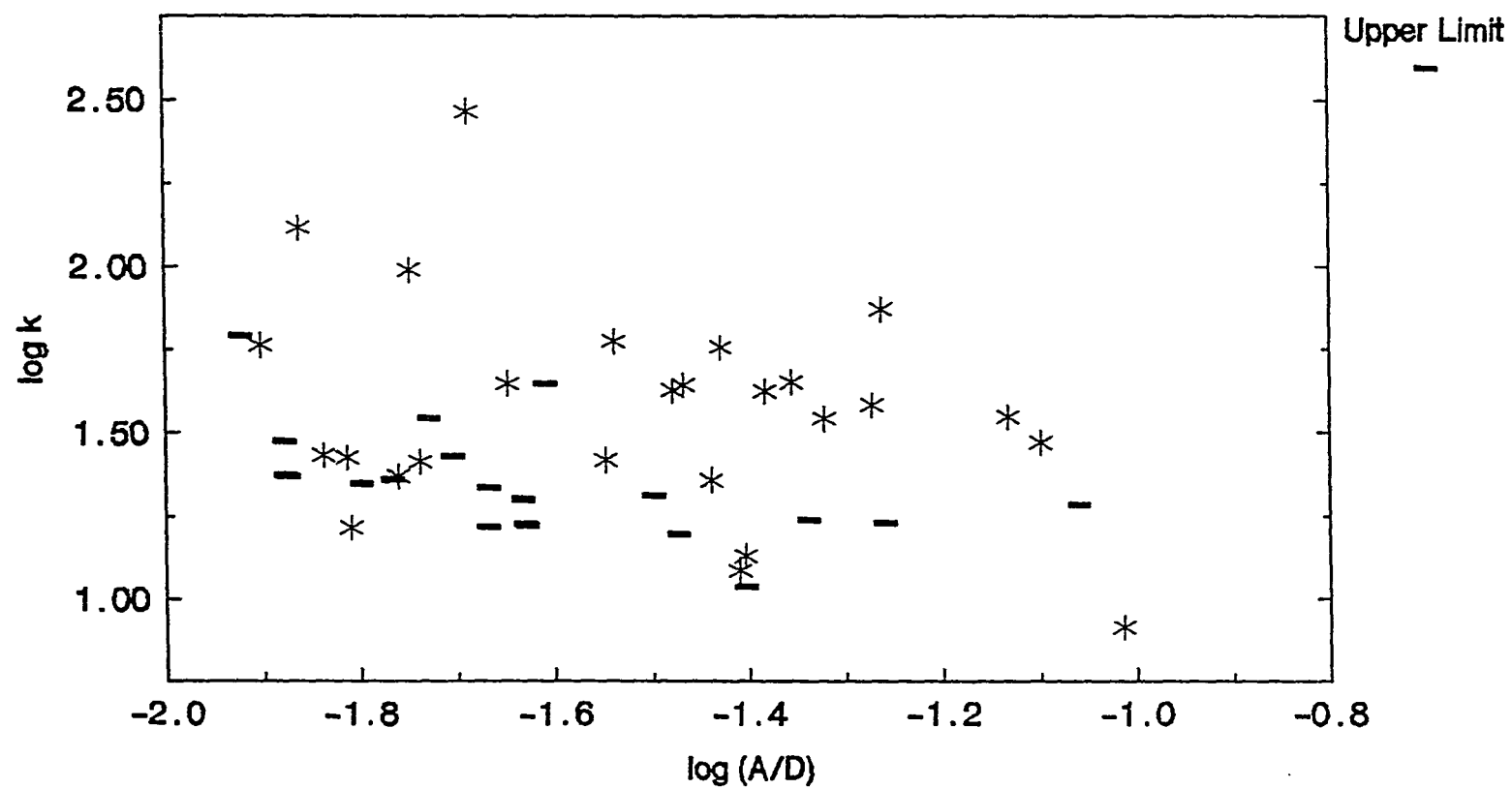


Table 4-6
Compactness Parameters for IBGS Galaxies

Name	R	σ_R	log A/D	R'	k
NGC 157	<0.08		-1.67		<21.7
NGC 828	<1.08		-1.35		
NGC 972	0.08	0.04	-1.41	0.05	12.2
NGC 1022	0.52	0.10	-1.38	0.50	42.2
NGC 1055	<0.14		-1.73		<35.0
NGC 1068	0.53	0.18	-1.86	0.53	130.5
NGC 1084	<0.07		-1.40		<10.9
NGC 1222	<0.50		-1.06		<19.2
NGC 1614	0.68	0.12	-1.10	0.63	29.5
NGC 2964	0.20	0.05	-1.44	0.17	22.8
NGC 3079	0.06	0.02	-1.81	0.06	26.7
NGC 3094	0.19	0.09	-1.01	0.01	8.1
NGC 3437	0.10	0.03	-1.40	0.06	13.4
NGC 3504	0.44	0.07	-1.47	0.42	43.9
NGC 3593	<0.30		-1.61		<44.6
NGC 3683	<0.19		-1.34		<17.3
NGC 3810	<0.05		-1.67		<16.5
NGC 3893	<0.06		-1.63		<16.8
NGC 4030	<0.08		-1.63		<19.9
NGC 4038	<0.24		-1.26		<16.9
NGC 4041	<0.10		-1.47		<15.8
NGC 4088	<0.05		-1.80		<22.3
NGC 4102	0.51	0.08	-1.54	0.50	59.4
NGC 4157	<0.06		-1.88		<29.8
NGC 4194	0.63	0.13	-1.43	0.61	57.1
NGC 4214	<0.17	0.09	-1.92		<61.9
NGC 4254	<0.06		-1.77		<22.9
NGC 4303	0.03	0.01	-1.81	0.02	16.4
NGC 4321	<0.04		-1.88		<23.6
NGC 4388	0.52	0.09	-1.75	0.52	97.8
NGC 4501	<0.04		-1.87		<23.4
NGC 4527	0.06	0.02	-1.84	0.05	27.0
NGC 4536	0.17	0.03	-1.90	0.16	57.9
NGC 4654	<0.10		-1.70		<26.9
NGC 4691	0.17	0.05	-1.55	0.15	26.1
NGC 4793	<0.14		-1.50		<20.6
Mkn 231	0.91	0.31	-1.26	0.91	74.4
NGC 4818	0.98	0.16	-1.69	0.98	290.4
NGC 4984	0.41	0.09	-1.48	0.40	42.5
NGC 5005	0.06	0.02	-1.76	0.05	23.4
NGC 5054	0.08	0.04	-1.74	0.07	25.8

Table 4-6
(continued)

Name	R	σ_R	log A/D	R'	k
Mkn 273	0.73	0.36	-1.13	0.70	35.3
NGC 5676	<0.06		-1.63		<16.7
NGC 5775	<0.05		-1.67		<16.5
IC 4553	0.50	0.09	-1.32	0.47	34.9
NGC 6240	0.59	0.10	-1.35	0.57	44.8
NGC 7469	0.61	0.20	-1.27	0.58	38.3
NGC 7479	0.26	0.06	-1.65	0.25	44.4
Mkn 331	<1.07		-0.78		

IV. Discussion

A. Relationship of R' to Optical Galaxy Properties

Perhaps the most convincing evidence that the infrared compactness parameter, R', is truly indicative of the presence or absence of a compact nuclear source in the infrared comes from a comparison of the nuclear spectral classifications of sources with high and low compactness parameters. Of 22 sources with $R' < 0.3$ which have spectral classifications in Table 4-5, 7 were classified as type A (no measurable optical emission lines), while none of the 14 classified sources with $R' > 0.3$ were type A. Conversely, only 3 of 22 low-R' sources were classified as Seyferts, LINERs, or H II region-LINER transition objects, while 12 of 14 high-R' sources were so classified.

The 10 μ m detection rates and average compactness parameters of the various classes show a similar trend. None of the 8 type A objects were

detected at 10 μm , and the average of their R upper limits is $0.13 \pm .07$. Six of 14 type H objects were detected with an average R' or R upper limit of $0.18 \pm .05$, and 11 of 12 type 1, 2, L, or T objects were detected with an average R' or upper limit of $0.46 \pm .08$. The corresponding figures for the concentration parameter, k are type A: $\langle k \rangle = 21 \pm 4$, type H: $\langle k \rangle = 20 \pm 4$, others: $\langle k \rangle = 50 \pm 10$.

The compactness parameter is also correlated with optical morphology, as demonstrated in Figure 4-8. Here we have plotted the corrected compactness parameter, R', against the modified Hubble type parameter, t, defined in Chapter 3. Figure 4-9 is the same as Figure 4-8, except that the concentration parameter, k, is plotted instead of R'. Recall that t is essentially identical to the Second Reference Catalog of Bright Galaxies (RC2) parameter T, except that negative numbers represent spirals with peculiar morphology rather than elliptical galaxies.

Figures 4-8 and 4-9 verify Devereaux's (1987) finding that compact nuclear infrared sources are more common among early type spirals (S0/a-Sab) than among later types. A similar trend has also been seen in optical. Kodaira, Watanabe, and Okamura (1987) performed bulge/disk decompositions on 167 spiral galaxies and found that "several early-type galaxies are best approximated with our method by models in which compact exponential components are buried in the central region of dominant spheroids."

Although the existence of compact sources at the centers of many early type spirals is established, the high fraction of early type spirals

in this infrared-bright sample displaying IR nuclear activity is undoubtedly a selection effect. Since there is less gas, dust, and star formation activity in early type spirals than in later types, fewer of these galaxies will be included in an IR-bright sample, unless they happen to contain active nuclei.

Figures 4-8 and 4-9 also provide evidence for more compact nuclear sources among galaxies with peculiar or irregular morphology than among normal late type spirals. The association of a compact IR nucleus with morphological peculiarities is interesting in light of the results of Chapter 3, which indicate that morphological peculiarity results in high infrared luminosity and distinctive IR spectral behavior similar to that seen in dust dominated Seyfert galaxies. The association of the IR activity in these objects with their nuclear regions is consistent with the results of Bushouse (1987) based on H α imaging of interacting galaxies with disturbed morphology, which have already been mentioned. In a subsequent study, Bushouse, Lamb, and Werner (1988) demonstrated that these same galaxies have significantly greater infrared luminosity and infrared to blue luminosity ratios than a control sample of isolated spirals.

The demonstration that morphological peculiarity is frequently associated with the presence of a compact nuclear infrared source, which in turn is associated with a strong nuclear emission line spectrum, completes the picture. Clearly a large number of infrared luminous galaxies are the result of dynamical disturbances, which give rise to a

powerful, dust-embedded (see Chapter 3) source of ionizing photons. This could take the form of a type 2 Seyfert, a nuclear starburst, a LINER, or a dust-embedded type 1 Seyfert.

Figure 4-8
Compactness Parameter vs. Optical Morphology

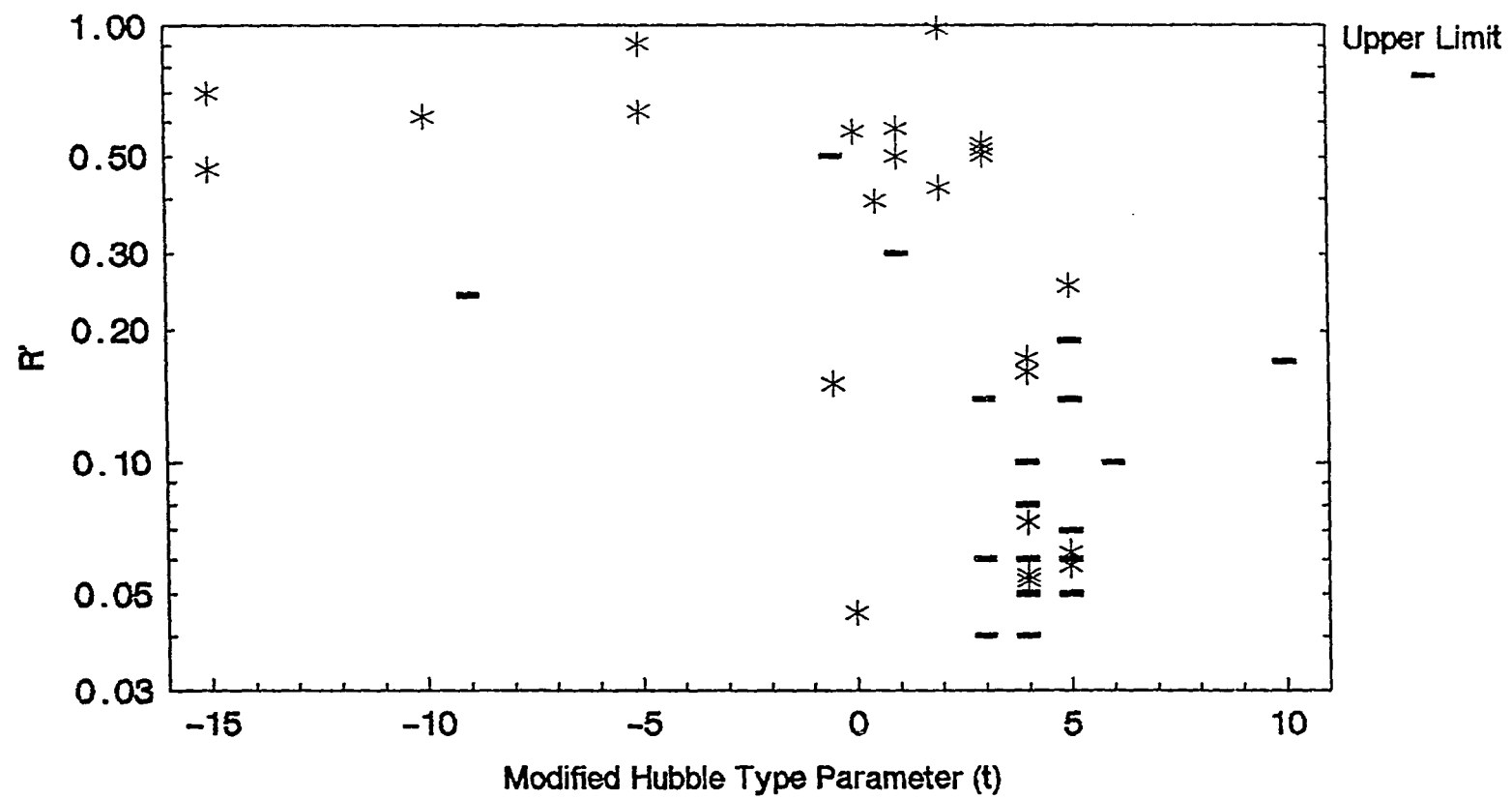
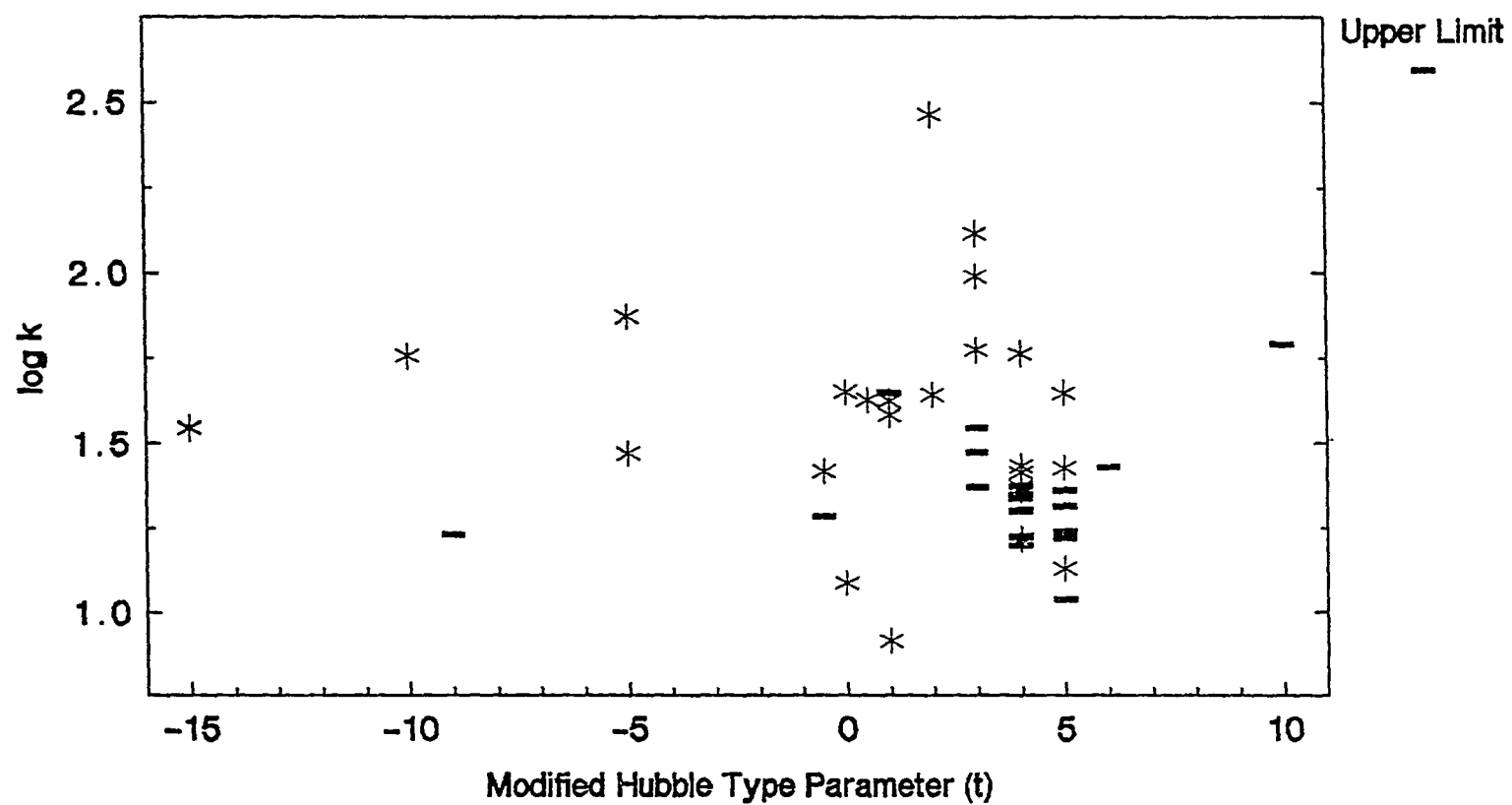


Figure 4-9
Concentration Parameter vs. Optical Morphology



B. Relationship of R' to Infrared Galaxy Properties

In the last chapter it was shown that all of the galaxies in the IBGS obey the well known IRAS color-color relation between $\log(F_{12}/F_{25})$ and $\log(F_{60}/F_{100})$, which probably indicates that their IR spectra are dominated by similar mixtures of dust grains at various average temperatures. Another color-color relation between $\log(F_{12}/F_{100})$ and $\log(F_{25}/F_{60})$, which seems to apply primarily to galaxies with active nuclei or peculiar morphology, the "second IRAS color-color relation", was also demonstrated. What effect does the presence of a compact nuclear source have on this IR spectral behavior?

To explore this question, we have divided the IBGS into a high R' sample--those with $R' > 0.3$, and a low R' sample--those with $R' < 0.3$. The boundary value of 0.3 was chosen in order to give a reasonable number of objects in the high R' sample, while attempting to insure that the nuclear contribution to their spectra would be large enough to have a discernable effect. The high R' sample contains 17 objects, and the low R' sample contains 33.

Figure 4-10 shows the second IRAS color-color relation for objects with high R' ($R' > 0.3$) and low R' ($R' < 0.3$). Sources with R upper limits greater than the cutoff value of 0.3 and sources without small aperture measurements are also plotted for comparison. The difference between the galaxies with significant compact infrared nuclear sources and those without is dramatic. This confirms the hypothesis put forward in Chapter

3 that the distinctive IR spectral behavior of Seyfert and peculiar galaxies, that which we term the "active" IR component, is associated with the presence of a nuclear IR source.

Figure 4-10 does not definitively establish that compactness at $11\ \mu\text{m}$, in the absence of a Seyfert nucleus, is necessary and sufficient for the existence of the second IRAS ($12/100\text{--}25/60\ \mu\text{m}$) color-color relation, though it certainly points in that direction. The single caveat is that the small number of non-Seyfert galaxies in the figure, for which R' has been measured, are all found toward the center of the sequence formed by the Seyferts; and none are on the edges. However, it was shown in the previous chapter that galaxies thought to be undergoing nuclear starbursts behave in a manner identical to the compact sources in Figure 4-10 over a very wide range of $25/60\ \mu\text{m}$ colors. Small aperture $10\ \mu\text{m}$ observations of a large sample of starburst galaxies (such as those listed in Table 3-10 of Chapter 3) are needed to verify the importance of a compact IR nucleus in causing the sort of behavior depicted in Figure 4-10. If the hypothesis that the second IRAS color-color relation characterizes compact nuclear infrared sources is correct, all of these objects which conform to that relation should show compact nuclei at $11\ \mu\text{m}$. Observational data available so far are consistent with this hypothesis.

The relationship between $11\ \mu\text{m}$ compactness and infrared luminosity is depicted in Figures 4-11 and 4-12. Compact infrared sources become increasingly prevalent at infrared luminosities, $L_{\text{IR}} \gtrsim 10^{10} L_{\odot}$ and are dominant above $10^{11} L_{\odot}$. A similar luminosity threshold separates galaxies

with 60/100 μm and IR/blue flux ratios correlated with L_{IR} from those which do not show any such correlation, as noted in Chapter 3. This suggests that these infrared color-luminosity relations may apply uniquely to the compact nuclear sources present in many of these objects.

An estimate of the fraction of total IR luminosity contained in the nuclear source is $R'L_{\text{IR}}$. If our hypothesis that only the nuclear source obeys the IR color-luminosity relations (Figures 3-3 and 3-4) is correct, then substantially better correlations should be obtained when $R'L_{\text{IR}}$ is plotted against F_{60}/F_{100} or when $R'L_{\text{IR}}$ is plotted against $R'L_{\text{IR}}/L_{\text{B}}$. These plots are shown in Figures 4-14 and 4-14. Comparison with Figures 3-3 and 3-4 from Chapter 3 shows that in both plots, the correlations are greatly improved and extended to lower IR luminosities as expected. Once again, the behavior of the Seyfert and non-Seyfert galaxies is quite similar. There is perhaps a slight tendency for the type 2 Seyfert to lie above the non-Seyfert galaxies in Figure 4-14. A similar tendency for Seyferts to lie above non-Seyfert galaxies with peculiar morphology in the IRAS (12/25-60/100 μm) color-color diagram was noted in Chapter 3. If this is confirmed, it would strongly suggest that the Seyfert nucleus (possibly in addition to a nuclear starburst) is an important contributor to heating the dust in these objects.

Figure 4-10
 Second IRAS Color-Color Diagram
 Infrared Bright Galaxy Sample

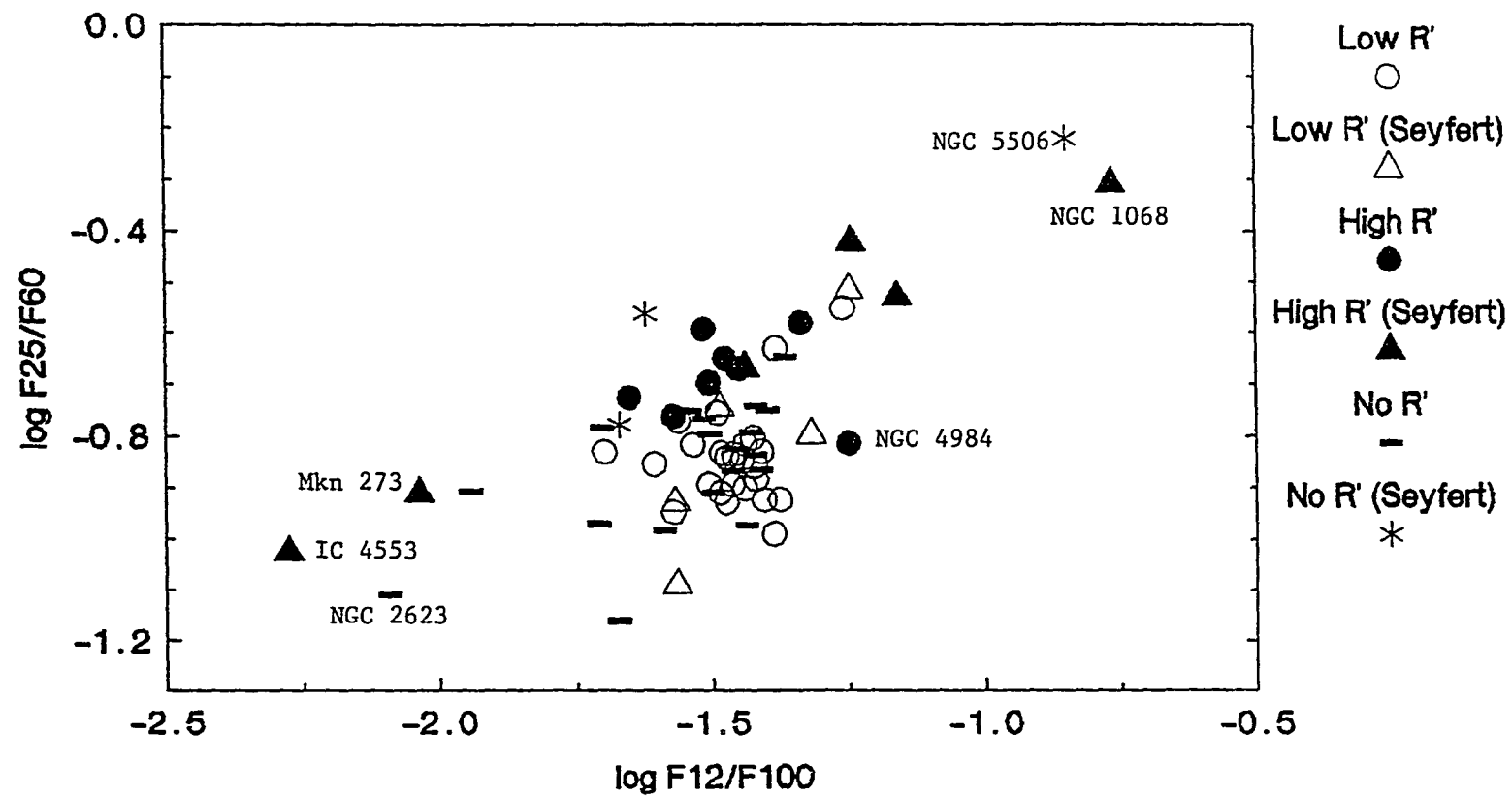


Figure 4-11
Compactness Paramter vs. IR Luminosity

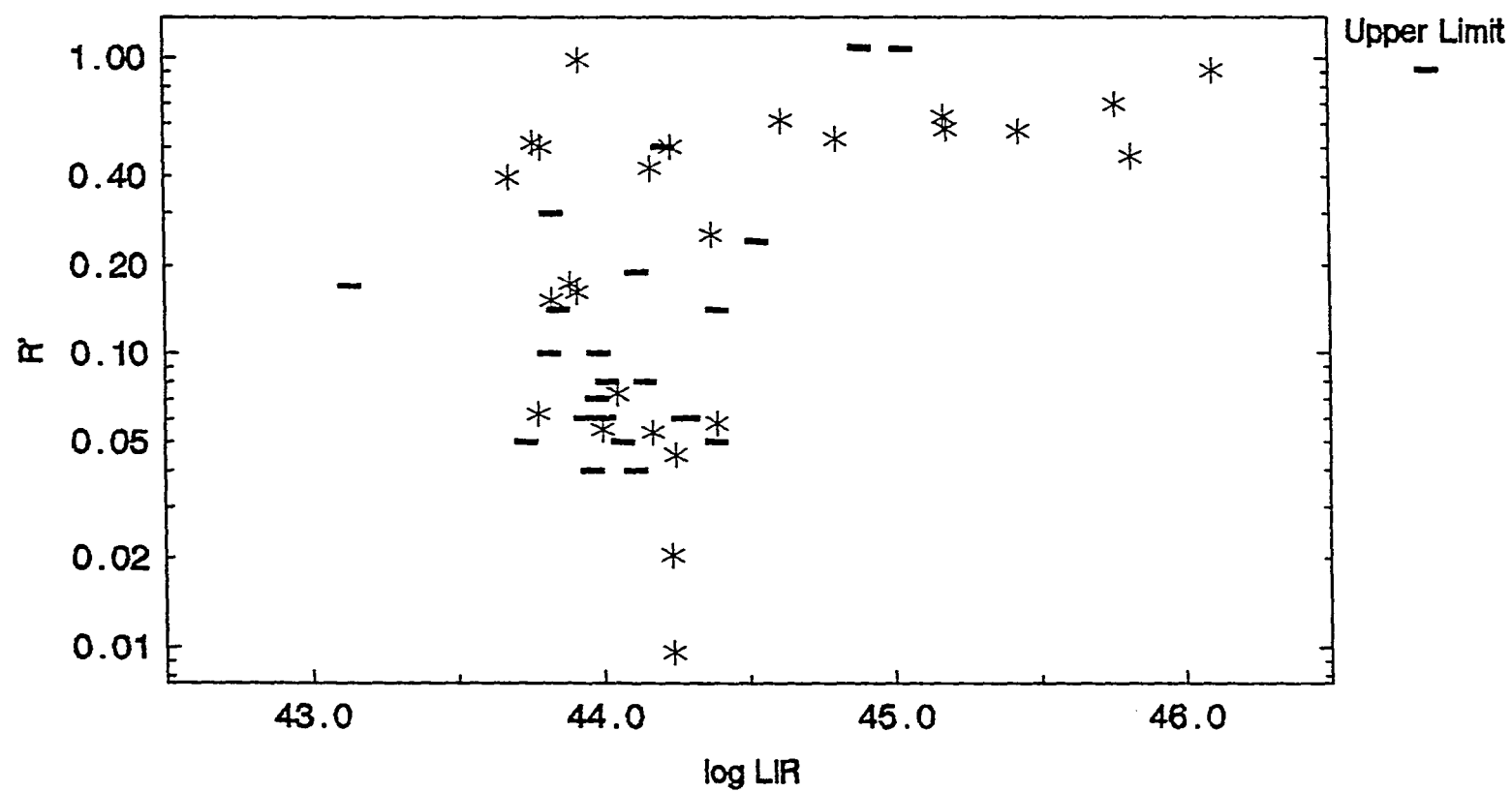


Figure 4-12
Concentration Paramter vs. IR Luminosity

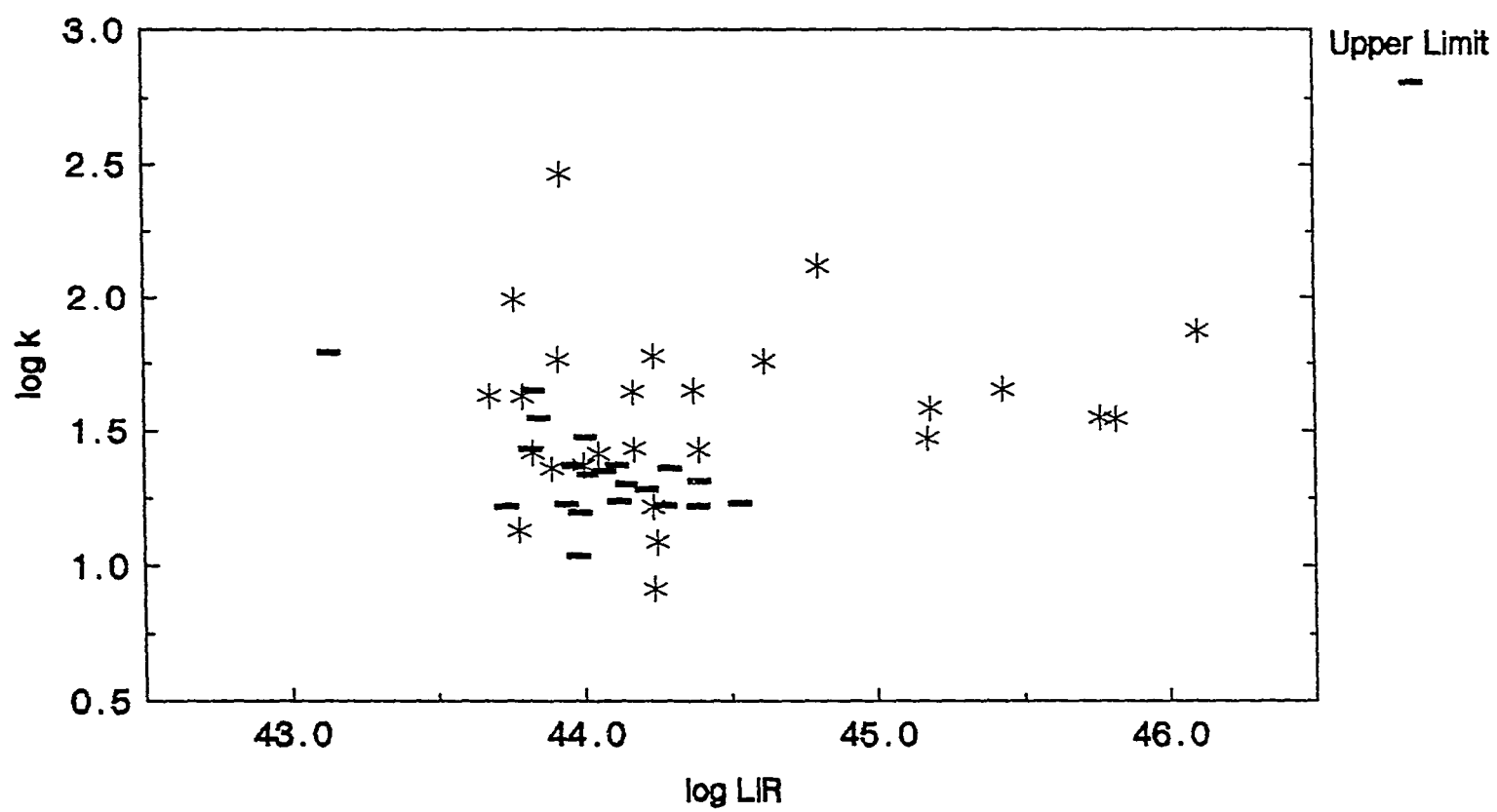


Figure 4-13
F60/F100 versus Nuclear Luminosity

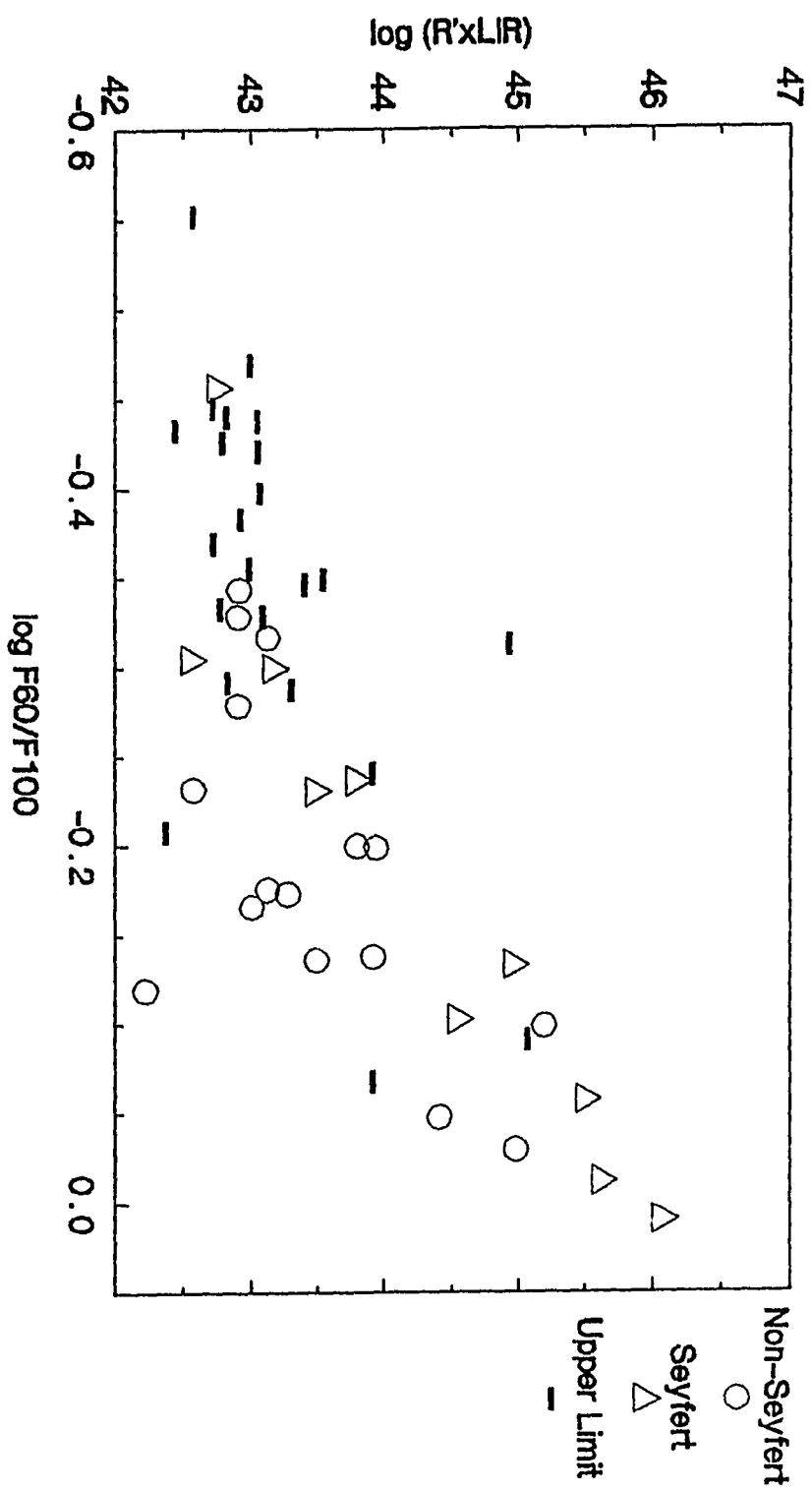
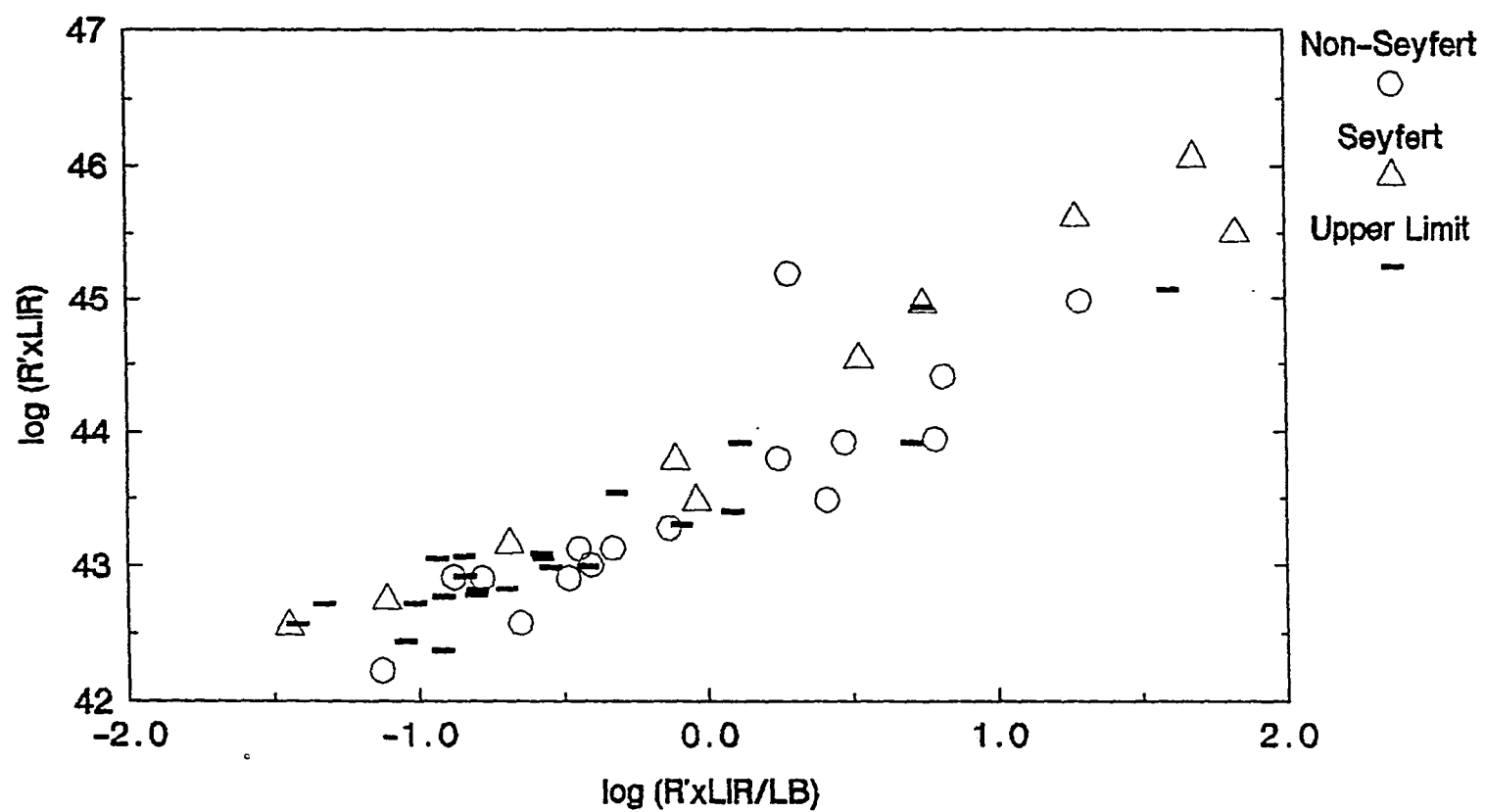


Figure 4-14
R'xLIR vs. (Nuclear IR / Total Blue) Luminosity



V. Conclusion

On the basis of the foregoing discussion and that in Chapter 3, we hypothesize that infrared excess (higher than normal IR/optical flux ratios) in galaxies is nearly always the result of activity confined to a galaxy's nuclear regions and associated with strong nuclear emission lines. The infrared emission associated with IR nuclear activity in the brightest infrared sources (including all IBGS sources) is dominated by thermal emission from dust grains and obeys infrared color-color and color-luminosity relationships not seen in disk-dominated ("quiescent") galaxies. The nuclear source exhibits similar behavior, regardless of whether it is associated with a known dust-embedded Seyfert nucleus or not. This is highly suggestive of some sort of phenomenology which is common to all of these sources.

There is little or no correlation between the total blue luminosity of the galaxy and the luminosity of the central source, which suggests the presence of a dust shell that is optically thick at $.44 \mu\text{m}$. This suggestion is consistent with the reddening indicated by nuclear Balmer line ratios (see Appendix A).

The frequent association of compact nuclear sources with peculiar optical morphology provides a natural explanation of these facts, since theoretical models of galaxy interactions which give rise to disturbed morphologies (e.g. Toomre and Toomre 1972) frequently predict dissipation of angular momentum and gas transport to the central regions of galaxies

(e.g. Eneev, Kozlov, and Sunyaev 1973; Steiman-Cameron and Durisen 1984; Icke 1985).

Once a large quantity of gas and dust is concentrated in the center of a spiral galaxy, either a nuclear starburst, a Seyfert nucleus, or both may result. Further theoretical and observational work is needed to clarify the physical conditions which decide among these possibilities and to determine whether a Seyfert nucleus will be formed as the result of a starburst after $\leq 10^8$ years, as suggested by Weedman (1983).

The correlation of 12/100 μm color with 25/60 μm color, which is present among Seyfert and peculiar galaxies is probably due to the presence of a compact nuclear source in the infrared. Similarly, the correlation 60/100 μm color and infrared luminosity results from the presence of a compact source and is seen most clearly when the luminosity of the compact source is plotted against 60/100 μm color. Galaxies without compact IR nuclei do not obey these relationships and exhibit a narrow range of 12/100 μm , 25/60 μm , and 60/100 μm colors.

The IR color-color and color-luminosity relations obeyed by galaxies showing compact nuclear sources in the infrared are difficult to explain using star formation, unless the star formation proceeds from the center outward inside a dense nuclear molecular cloud complex, as suggested by Rieke, Lebofsky, and Walker (1988). This is because star formation regions such as those seen in galactic disks, which are independently forming stars over an area much larger than their individual size would not be expected to display large variations in their integrated infrared

colors and infrared to blue luminosity ratio, nor would they obey an infrared color-luminosity relation over three decades in luminosity.

Detailed theoretical models of starbursts and/or active galactic nuclei embedded in optically thick dust clouds are needed to determine whether or not they can reproduce the behavior of Seyfert and peculiar galaxies in the F_{12}/F_{100} - F_{25}/F_{60} and F_{60}/F_{100} - L_{IR} planes and, if so, under what conditions. These IR color-color and color-luminosity relations represent the best available constraints on theories of dust-embedded nuclear starbursts and/or active galactic nuclei.

There is also a great need for careful and extensive small aperture 10 μ m observations of galaxies, to test whether the existence of a compact IR nucleus is both necessary and sufficient to explain the second IRAS color-color relationship (Figure 4-10) and the IR color-luminosity relationship (Figure 4-14). The latter could be extremely useful as a standard candle, especially after the advent of far-IR imaging with SIRTf when detailed observations of galactic nuclei at 60 μ m and 100 μ m become more widely available. Detailed optical and IR nuclear spectroscopy of galaxies containing compact infrared sources is needed to clarify the role played by Seyfert nuclei and/or starbursts in these sources. Infrared imaging at various wavelengths would also be useful for determining the temperature structure of the hypothesized dust shell in these sources and whether the dust is heated by a point-like or small extended source.

Chapter 5

CONCLUSIONS

I. Summary of Results

We have studied the relationship between the infrared spectral properties of galaxies, as measured by IRAS, and various forms of galaxy activity. The brightest extragalactic objects at mid- to far-IR wavelengths are (in order of frequency) nearby, normal spirals; morphologically peculiar or irregular galaxies or galaxy mergers; type 2 Seyferts; and dusty type 1 Seyferts. All of these objects are dominated by dust at varying temperatures based on their behavior in the 12/25-60/100 μm color-color plane, which is characteristic of emission from realistic mixtures of interstellar dust grain sizes and compositions.

Absent a Seyfert nucleus or morphological peculiarities, late type spirals occupy a narrow range of IRAS colors, which probably results predominantly from cirrus emission at 12 μm and 100 μm and from star formation complexes in their disks at 25 μm and 60 μm . The narrow range of far-IR colors and IR/blue luminosity ratios resulting from this mixture of star formation and interstellar dust warmed by the ambient UV/optical radiation field is explainable by hypothesizing a ratio of current to past star formation which varies little from one spiral galaxy to the next. This idea is consistent with the results of optical studies.

Among IR-bright galaxies the presence of a compact nuclear infrared source is associated with the presence of significant quantities of

ionized gas in the nucleus surrounded by a dust shell which is optically thick at visual wavelengths. This occurs most frequently in Seyfert galaxies, galaxies with peculiar or irregular optical morphology, and IR-bright early type spirals. The dust in this shell is exposed to significantly higher UV photon intensities on average than the dust in spiral disks, which accounts for the tendency of these sources to lie toward the upper left-hand side of the 12/25-60/100 μm color-color plane. Sources of this kind are common above infrared luminosities of $10^{10} L_{\odot}$ and appear to be the predominant cause of infrared luminosities above $\sim 10^{11} L_{\odot}$ in galaxies.

These dust-dominated, compact nuclear IR sources exhibit an extremely broad range of well-correlated 25/60 μm and 12/100 μm colors, which may be either colder or warmer than the colors of quiescent galaxies. This 12/100-25/60 μm color-color relation exists in both Seyfert and non-Seyfert galaxies over a wide range of colors and is also seen in galaxies thought to be undergoing nuclear starbursts. The probability of finding an optically visible Seyfert nucleus probably increases monotonically toward warmer 12/100 and 25/60 μm colors; it is certain that objects displaying the warmest 25/60 μm colors are mostly Seyferts (though it is not true that most Seyferts display such colors).

Many nearby Seyferts with weak nuclei (especially those of type 2) have substantial or even dominant contributions to their IR spectra from the host galaxy disk. Their IR emission is not strongly concentrated toward their nuclei, and their behavior in IR color-color diagrams is thus

similar to that of quiescent galaxies (see e.g. Figures 3-2 and 3-5).

There is some evidence that Seyfert galaxies with extremely cold 25/60 μm colors may be experiencing intense bursts of star formation in the immediate vicinity of their nuclei. Both spectroscopy and imaging at optical and infrared wavelengths are needed to clarify this matter. It is possible that the 12/100-25/60 μm color-color relation seen in dust-dominated, compact nuclear infrared sources results from a blend of cold starburst and warm Seyfert components, but such an interpretation is difficult to reconcile with the existence of non-Seyfert warm IRAS galaxies and indications that the most highly obscured Seyfert nuclei exhibit the coldest IR colors (Kailey and Lebofsky 1988; Edelson and Malkan 1986).

The weak correlation between the 60/100 μm colors and far-IR luminosities of the more luminous IRAS galaxies results entirely from the presence of dust-dominated, compact nuclear IR sources of varying strengths in many IR-bright galaxies. When an estimate of the nuclear fraction of the IR luminosity of bright IRAS galaxies is plotted against 60/100 μm color, the correlation is dramatically improved and is seen to extend to much lower luminosities. This remarkable relationship seems to be valid for nuclear IR sources which are dominated by thermal emission from dust over about three decades in luminosity, encompassing sources from galaxy-like ($10^9 L_{\odot}$) to quasar-like ($10^{12} L_{\odot}$) strength.

There is a possible tendency for Seyferts to lie at higher IR luminosities for a given 60/100 μm color, but the overall behavior of

dusty Seyferts and non-Seyfert galaxies possessing compact nuclear IR sources is remarkably similar. The existence in these sources of both a color-color and a color-luminosity relation among the four IRAS bands implies that, to a first approximation, they can be modelled with just two parameters. If the similar IR spectral behavior shown by these sources results from similar source geometry involving a centrally heated dust shell, the luminosity of the central source and the optical depth of the dust shell are likely choices for the parameters. Alternative possibilities for the second parameter include the relative contribution of a nuclear starburst and an active nucleus or the age of a nuclear starburst. Further observations and theoretical work are needed to clarify this.

II. Suggestions for Future Work

The most interesting result to emerge from the large body of observational data assembled here is the frequent occurrence and distinctive spectral characteristics of dust-dominated, compact nuclear infrared sources, which is, to first order, independent of whether they are associated with an optically visible Seyfert nucleus, disturbed morphology indicative of an interaction, a nuclear starburst, or some combination of these.

Detailed observations of the central regions of galaxies exhibiting the full range of 25/60 μm colors are needed to understand (at each infrared color) (1) what fraction of the ionizing flux is supplied by star

formation and what fraction by a nonthermal source? (2) what is the scale length of the source which heats the dust? (3) what is the space density of these sources, and what fraction of them have disturbed morphology? and (4) is the dust associated with ionized or neutral gas, and what is its configuration and optical depth?

Spectroscopy of the ionized gas in the nuclei of these objects can help to address several of these questions. By observing lines from atomic species of greatly differing ionization energies and concentrating on the red and infrared spectra, which are less susceptible to dust reddening, it will be possible to constrain the nature of the ionizing source, the surrounding nebula, and the dust shell.

The 2.35 μm CO bandhead has much potential as a gauge of star formation rates in the nuclei of these galaxies. This stellar absorption feature is sensitive to luminosity and thus constrains the supergiant/giant/dwarf mixture. Furthermore, measurement of this feature entails flux comparison over a very small range of near-IR wavelengths, which minimizes the importance of high and/or nonuniform extinction toward the source. Near-IR CO observations will be most useful when observations of this feature in a large sample of red stars--especially supergiants--over a large range of metallicities can be used to calibrate the effects of metallicity in both the bulge and disk populations. Also, near-IR bulge/disk decompositions of normal spirals will be needed to estimate the contribution of bulge stars to the CO bands. The 2.35 μm CO band may be the most powerful single discriminator between an active nucleus and star

formation once the basic data necessary to convincingly calibrate it become available.

On the subject of observations, we wish to stress the importance of imaging at 10 μm and longer wavelengths. Ten micron imaging of extragalactic objects is just becoming available, while imaging at longer wavelengths is unlikely to appear for any significant number of sources until SIRTf is flown. Meanwhile, measurement of IRAS galaxies showing aberrant 25/60 μm colors through smaller apertures at 25 μm , 60 μm , and 100 μm with the Keuper Airborne Observatory would be useful.

Such imaging or accurate, reproducible aperture photometry through at least three different apertures could be used to construct more realistic and unbiased source models along the lines of Chapter 4. These models would yield information on both the relative flux of the compact source and its size scale. Armed with this information, our knowledge of the 12/100-25/60 μm color-color and 60/100 μm color-luminosity relations could be greatly refined; and models of dust-embedded active nuclei and nuclear starbursts attempting to reproduce these relations would be more tightly constrained. Furthermore, knowledge of the spatial distribution of the infrared flux within the compact nuclear source represents an additional, geometric constraint on the source models, over and above the spectral ones. Obviously, a small extended power source, such as a region of star formation or a cluster of accreting stellar remnants, will give rise to a different radial distribution of grain temperatures from a single, point-like source, such as a massive black hole and accretion

disk.

Finally, there is the need for much theoretical work in this area. The need for careful treatment of the $2.35\ \mu\text{m}$ CO feature has already been touched upon. There are many other areas of uncertainty. What parameters of an interaction control the mass of gas and dust transported to the nucleus of the interacting galaxies? What other processes are capable of transporting large quantities of gas to the nuclei of spirals? Can these processes be related to the statistical properties of high luminosity IRAS galaxies and perhaps quasars? What is the expected radial distribution and kinematics of the nuclear gas once it is there? Assuming a burst of star formation follows this event, how does the resulting H II region and surrounding cloud complex evolve under the influence of multiple supernova shock waves? Can this account for the radio continuum and H_2 emission lines seen in these sources? What happens to the stellar remnants? Will they be concentrated in the center or merge with a massive black hole if one is already present? And, of course, what parameters of this (or another) model control the object's location on the $12/100\text{--}25/60\ \mu\text{m}$ and $60/100\text{--}L_{\text{IR}}$ sequences?

Balick and Heckman (1982) have reviewed the impressive contributions to our knowledge of active galaxies from studies of the non-nuclear regions of these galaxies. Davidson and Netzer (1979) have stressed the usefulness of studying the optical emission line spectrum as a clue to the nature of the central source. While both of these approaches have their unique value, infrared studies of active galaxies may represent the

missing link between them. By studying the dust shell which surrounds the ionized gas in many active galaxies, vital clues to what they are and to the processes which form them will almost certainly emerge. This is so because the dust shell, like the host galaxy itself, is larger than the nucleus or the ionized nebula and it is thus easier to resolve its structure and study it. Yet, as we have seen, it is intimately connected with the nuclear regions and powered by the nuclear activity, as is the ionized gas. Furthermore, the remarkable color-color and color-luminosity relationships obeyed by this shell of dust is suggestive of a very general set of physical processes which govern it. Understanding those physical processes and the conditions which cause them to operate may well be the key to unravelling the problem of nuclear activity in galaxies.

Appendix A

NUCLEAR REDDENING ESTIMATES FOR IBGS GALAXIES

We have used the Hydrogen Balmer series emission line fluxes reported in Table 4-4 (Chapter 4) to estimate the reddening of the nuclear emission lines due to foreground dust in several galaxies from the Infrared Bright Galaxy Sample (IBGS). The reddenings assume case B recombination (Osterbrock 1974), which gives rise to intrinsic line flux ratios that vary insignificantly over the relevant region of the electron temperature-density plane. Line ratios for case B recombination with $T_e = 10^4$ K have been taken from Brocklehurst (1971). A standard reddening curve given by Miller and Mathews' (1972) fit to Whitford's (1958) optical data and Nandy's (1968) UV data was assumed. When adjusted to Rieke and Lebofsky's (1985) ratio of total to selective absorption, $R=3.09$, this yields

$$\tau_\lambda / \tau_{H\beta} = \begin{cases} \frac{.618}{\lambda} - .271 & \lambda > .4337 \mu\text{m} \\ \frac{.359}{\lambda} - .373 & \lambda < .4337 \mu\text{m} \end{cases} \quad (1)$$

where $\tau_{H\beta}$ and τ_λ are the dust optical depth at $.48613 \mu\text{m}$ ($H\beta$) and λ respectively, and λ is between 3500 \AA and $1.1 \mu\text{m}$.

It is convenient to ratio Balmer series lines to $H\alpha$, since it is usually bright enough to be well measured, is least affected by underlying stellar absorption features, and provides the longest wavelength baseline. Let $H\beta$ represent the $H\beta$ line flux, and let $H\alpha$ represent the flux from

another Balmer line. Then the equation of radiative transfer gives rise to

$$\tau_{H\beta} = \frac{\tau_{H\beta}}{\tau_{Hx} - \tau_{H\beta}} \left[\ln \left(\frac{H\beta}{Hx} \right)_{\text{Obs}} - \ln \left(\frac{H\beta}{Hx} \right)_{\text{Case B}} \right] \quad (2)$$

where τ_{Hx} is the optical depth at the wavelength of Hx. The subscript Obs represents observed values, while Case B signifies intrinsic Case B values. Values of the constants in equation (2) are given for several Balmer series lines in Table A-1.

Table A-1
Constants Used to Determine Reddening

Line	$\lambda (\mu m)$	$\ln(H\alpha/Hx)$	$\tau_{H\beta}/(\tau_{Hx} - \tau_{H\alpha})$
H β	.48613	1.047	3.040
H γ	.43405	1.804	2.075
H δ	.41017	2.398	1.733
H ϵ	.39701	2.886	1.650

Finally values of $\tau_{H\beta}$ derived from our measurements of H α , H β , and H γ are given in Table A-2. Data for NGC 1068 have been taken from Koski (1978). The approximate validity of our assumption of Case B conditions (namely that the nebula is optically thick to all Lyman lines and that the electron density is $\lesssim 10^9 \text{ cm}^{-3}$) and a standard reddening law is demonstrated by the good agreement of estimates based on various pairs of Balmer emission lines in Table A-2, which is $\lesssim 20\%$ in almost all cases.

Table A-2
Dust Reddening of IBGS Galaxies

Name	$\tau_{H\beta}(\alpha, \beta)$	$\tau_{H\beta}(\alpha, \gamma)$	$\tau_{HB}(\alpha, \gamma)$	$\langle \tau_{H\beta} \rangle$
NGC 972	4.3	4.3
NGC 1022	3.2	4.1	...	3.6
NGC 1068 ^a	1.4	1.6	1.6	1.5
NGC 1084	2.9	2.9
NGC 1222	2.1	2.1
NGC 1614	3.5	3.2	3.5	3.4
NGC 2964	2.5	2.4	...	2.4
NGC 3094	2.5	2.5
NGC 3437	1.4	1.8	...	1.6
NGC 3504	2.1	2.5	...	2.3
NGC 4038	4.5	2.7	...	3.6
NGC 4041	4.1	4.1
NGC 4088	5.1	5.1
NGC 4194	3.2	3.1	...	3.1
Mkn 273 ^b	3.9
NGC 6240	5.9	6.3	...	6.1

Notes to Table A-2

a. Flux ratios taken from Koski (1978).

b. H α not measured. Value in last column derived from H β /H γ ratio.

As a further check on these reddening estimates, we list in Table A-3 three values of $\tau_{H\beta}$ derived from emission line measurements published by other authors, which agree within the expected error of ~20% (see Chapter 3) with those in Table A-2.

Table A-3
Reddening Estimates from Published Spectroscopy

Name	$\tau_{H\beta}(\alpha, \beta)$	$\tau_{H\beta}(\alpha, \gamma)$	$\tau_{HB}(\alpha, \gamma)$	$\langle \tau_{H\beta} \rangle$
NGC 1614 ^a	3.7	3.5	4.1	3.8
Mkn 273 ^b	3.6	3.8	2.9	3.4
NGC 6240 ^c	5.1	5.1

Notes to Table A-3

- a.* Entries based on spectroscopy in Aitken, Roche, and Phillips (1981).
- b.* Entries based on optical spectroscopy in Koski (1978).
- c.* Entries based on spectroscopy in Fosbury and Wall (1979).

List of References

- Aaronson, M., Bothun, G., Mould, J., Huchra, J., Schommer, R. A., and Cornell, M. 1986, Ap. J., 302, 536.
- Aaronson, Marc, Huchra, John, Mould, Jeremy, Schechter, Paul L., and Tully, R. Brent 1982a, Ap. J., 258, 64.
- Aaronson, M. et al. 1982b, Ap. J. Suppl. Ser., 50, 241.
- Aitken, D. K., Roche, P. F., and Phillips, M. M. 1981, Mon. Not. Roy. Astr. Soc. (Short Comm.), 196, 101P.
- Allen, C. W. 1976, Astrophysical Quantities (Third Edition) (London: Athlone Press).
- Armus, Lee, Heckman, Timothy, and Miley, George 1987, A. J., 94, 831 (AHM87).
- Baldwin, J. A., Phillips, M. M., and Terlevich, R. 1981, Publ. Astron. Soc. Pac., 93, 5.
- Balick, Bruce and Heckman, Timothy M. 1982, Ann. Rev. Astr. Ap., 20, 431.
- Becklin, E. E. and Wynn-Williams, G. C. 1987, in Star Formation in Galaxies, ed. Carol J. Lonsdale Persson (Washington DC: US Government Printing Office).
- Beichman, C. A., Neugebauer, G., Habing, H. J., Clegg, P. E., and Chester, T. J., eds. 1985a, IRAS Catalogs and Atlases: Explanatory Supplement (Washington, DC: US Government Printing Office) (PSC).
- Beichman, C. A., Neugebauer, G., Habing, H. J., Clegg, P. E., and Chester, T. J., eds. 1985b, IRAS Catalogs and Atlases: The Point Source Catalog (Washington, DC: US Government Printing Office) (PSC).
- Boroson, Todd 1981, Ap. J. Suppl. Ser., 46, 177.
- Brocklehurst, M. 1971, Mon. Not. Roy. Astr. Soc., 153, 471.
- Burstein, David and Lebofsky, Marcia J. 1986, Ap. J., 301, 683.
- Bushouse, Howard A. 1987, Ap. J., 320, 49.
- Bushouse, Howard A., Lamb, Susan A., and Werner, Michael W. 1988, Ap. J., in press (BLW88).
- Carter, D. 1984, Astronomy Express, 1, 61 (C84).

- Claussen, M. J., Kleinman, S. G., Joyce, R. R., and Jura, M. 1987, Ap. J. Suppl. Ser., 65, 385.
- Cutri, R. M., Rudy, R. J., Rieke, G. H., Tokunaga, A. T., and Willner, S. P. 1984, Ap. J., 280, 521.
- Davidson, Kris and Netzer, Hagai 1979, Rev. Mod. Phys., 51, 715.
- de Grijp, M. H. K., Miley, G. K., Lub, J., and de Jong, T. 1985, Nature, 314, 240 (dG85).
- de Jong, T. et al. 1984, Ap. J. (Letters), 278, L67.
- Désert, F. X. 1986, in Light on Dark Matter, ed. F. P. Israel (Dordrecht: Reidel), p. 213.
- de Vaucouleur, Gerard, de Vaucouleur, Antoinette, and Corwin Harold G., Jr. 1976. Second Reference Catalog of Bright Galaxies (Austin: University of Texas Press) (RC2).
- Devereaux, Nicholas 1987, Ap. J., 323, 91 (Dev).
- Devereaux, Nicholas A., Becklin, E. E., and Scoville, Nick 1987, Ap. J., 312, 529 (DBS87).
- Edelson, R. A. 1987, Ap. J., 313, 651.
- Edelson, R. A., and Malkan, M. A. 1986, Ap. J., 308, 59.
- Edelson, R. A., and Malkan, M. A. 1987, Ap. J., 323, 516.
- Edelson, R. A., Malkan, M. A., and Rieke, G. H. 1987, Ap. J., 321, 233 (EMR, EMR87).
- Eneev, J. M., Kozlov, N. N., and Sunyaev, R. A. 1973, Astr. Ap., 22, 41.
- Fosbury, R. A. E., and Wall, J. V. 1979, Mon. Not. Roy. Astr. Soc., 189, 79.
- Heckman, T. M. 1980, Astr. Ap., 87, 152.
- Heckman, Timothy M., Armus, Lee, and Miley, George K. 1987, A. J., 92, 276.
- Helou, George 1986, Ap. J. (Letters), 311, L33.

- Helou, George and Walker, D. W. 1986, IRAS Catalogs and Atlases: IRAS Small Scale Structure Catalog (Washington, DC: US Government Printing Office) (SSSC).
- Huchra, J. P., and Geller, M. J. 1982, Ap. J., 257, 423.
- Icke, V. 1985, Astr. Ap., 144, 115.
- Jura, M. 1982, Ap. J., 254, 70.
- Kailey, Walter F., and Lebofsky, M. J. 1988, in Comets to Cosmology: Proceedings of the Third International IRAS Conference, ed. A. Lawrence (London: Springer Verlag), in press.
- Keel, William C. 1983, Ap. J. Suppl. Ser., 52, 229.
- Kennicutt, Robert C. 1983, Ap. J., 272, 54.
- Kent, S. M. 1985, Ap. J. Suppl. Ser., 59, 115.
- Kirshner, Robert P., Oemler, Augustus, Jr., Schechter, Paul L. 1978, A. J., 83, 1549.
- Kodaira, Keiichi, Watanabe, Masaaki, and Okamura, Sadanori 1986, Ap. J. Suppl. Ser., 62, 703.
- Koski, Alan T. 1978, Ap. J., 223, 56.
- Larson, Richard B., and Tinsley, Beatrice M. 1978, Ap. J., 219, 46.
- Lebofsky, M. J., and Rieke, G. H. 1979, Ap. J., 229, 111.
- Lauberts, Andris 1982 The ESO Uppsala Survey of the ESO (B) Atlas (Munich: European Southern Observatory).
- Lawrence, A. 1988 in Comets to Cosmology: Proceedings of the Third International IRAS Conference, ed. A. Lawrence (London: Springer Verlag), in press.
- Low, F. J. and Rieke, G. H. 1974, in Methods of Exp. Phys., 12, ed. N. P. Carleton (New York: Academic Press). Malkan, Matthew A. 1983, , Ap. J. (Letters), 264, L1.
- Malkan, Matthew A. 1986, Ap. J., 310, 679.
- Matthews, T. A. and Sandage, A. R. 1963, Ap. J., 138, 30.

- Matthews, K., Neugebauer, G., McGill, J., and Soifer, B. T. 1987, A. J., 94, 297.
- Meurs, E. J., and Wilson, A. S. 1984, Astr. Ap., 136, 206.
- Mihalis, Dimitri and Binney, James 1981, Galactic Astronomy Structure and Kinematics (San Francisco: W. H. Freeman & Co.).
- Miley, G., Neugebauer, G., and Soifer, B. T. 1985, Ap. J. (Letters), 293, L11.
- Miller, Glenn E. and Scalo, John M. 1979, Ap. J. Suppl. Ser., 41, 513.
- Miller, Joseph S., and Mathews, William G. 1972, Ap. J., 172, 593.
- Nandy, K. 1968, Pub. Roy. Obs. Edinburgh, 6, 169.
- Nilson, Peter 1973, Uppsala General Catalog of Galaxies (Uppsala: Uppsala Offset Center AB) (UGC).
- Oke, J. B. 1974, Ap. J. Suppl. Ser., 27, 21.
- Osterbrock, Donald E. 1974, Astrophysics of Gaseous Nebulae (San Francisco: W. H. Freeman & Co.).
- Osterbrock, Donald E. 1984, Ap. J. (Letters), 280, L43.
- Osterbrock, Donald E., and Dahari, Oved 1983, Ap. J., 273, 478.
- Osterbrock, Donald E., and de Robertis, M. M. 1985, Publ. Aston. Soc. Pac., 97, 1129 (OdR).
- Pacholczyk, A. G. and Wymann, R. J. 1968, A. J., 73, 850.
- Palumbo, G. G. C., Tanzella-Nitti, G., and Vettolani, G. 1983 Radial Velocities of Galaxies (New York: Gordon and Breach).
- Persson, Carrol J. Lonsdale 1986, IPAC User's Guide, (Pasadena: Infrared Processing and Analysis Center).
- Phillips, M. M., Aitken, D. K., and Roche, P. F. 1984, Mon. Not. Roy. Astr. Soc., 207, 25.
- Phillips, M. M., Charles, P. A., and Baldwin, J. A. 1983, Ap. J., 266, 485.
- Puget, J. L., Léger, A., and Boulanger 1985, Astr. Ap. (Letters), L19.

- Rice, W. et al. 1988, Ap. J. Suppl. Ser., in press.
- Rieke, G. H. 1978, Ap. J., 226, 550 (R78).
- Rieke, G. H., Cutri, Roc M., Black, J. H., Kailey, Walter F., Mcalaray, Christopher W., Lebofsky, M. J., and Elston, R. 1985, Ap. J., 290, 116.
- Rieke, G. H., Lebofsky, M. J., Thompson, R. I., Low, F. J., and Tokunaga, A. T. 1980, Ap. J., 238, 24.
- Rieke, G. H., and Lebofsky, M. J. 1978, Ap. J. (Letters), 220, L37 (RL78).
- Rieke, G. H., and Lebofsky, M. J. 1979 Ann. Rev. Astr. Ap., 17, 477.
- Rieke, G. H., and Lebofsky, M. J. 1986, Ap. J., 304, 326.
- Rieke, G. H., Lebofsky, M. J., and Low, F. J. 1985, A. J., 90, 900.
- Rieke, G. H., Lebofsky, M. J., and Walker, C. E. 1988, Ap. J., 325, 686 (RLW88).
- Rieke, G. H., and Low, F. J. 1972, Ap. J. (Letters), 176, L95 (RL72).
- Roche, P. F., Aitken, D. K., Phillips, M. M., and Whitmore, B. 1984, Mon. Not. Roy. Astr. Soc., 207, 35.
- Roche, P. F., Aitken, D. K., and Whitmore B. 1983, Mon. Not. Roy. Astr. Soc. (Short Comm.), 205, 21P.
- Rudy, Richard J. 1984, Ap. J., 284, 33.
- Sandage, Allan and Tamman, G. A. 1981, A Revised Shapley Ames Catalog (Washington, DC: Carnegie Institution).
- Sanders, D. B., Soifer, B. T., and Neugebauer, G. 1988, in Comets to Cosmology: Proceedings of the Third International IRAS Conference, ed. A. Lawrence (London: Springer Verlag), in press.
- Sargent, W. L. W. 1970, Ap. J., 160, 405.
- Searle, Leonard, Sargent, W. L. W., and Bagnuolo, W. G. 1973, Ap. J., 179, 427.
- Seyfert, C. K. 1943, Ap. J. 97, 28.
- Simkin, S. M., Su, H. J., and Schwarz, M. P. 1980, Ap. J., 237, 404.

- Slipher, V. M. 1918, Low. Obs. Bull., 3, 59.
- Soifer, B. T., et al. 1984, Ap. J. (Letters), 278, L71.
- Soifer, B. T., et al. 1987, Ap. J., 320, 238.
- Steiman-Cameron, T. Y., and Durisen, R. H. 1984, Ap. J., 276, 101.
- Telesco, C. M., Becklin, E. E., and Wynn-Williams, C. G. 1980, Ap. J. (Letters), 241, L69.
- Tifft, W. G. 1978, Ap. J., 222, 54.
- Toomre, A. and Toomre, J. 1972, Ap. J., 178, 623.
- Twarog, B. A. 1980, Ap. J., 242, 242.
- Veilleux, Sylvain and Osterbrock, Donald E. 1987, Ap. J. Suppl. Ser., 63, 295.
- Véron-Cetty, M. -P., and Véron, P. 1985, ESO Scientific Report, No. 4.
- Véron-Cetty, M. -P., and Véron, P. 1987, ESO Scientific Report, No. 5.
- Ward, Martin, Elvis, Martin, Fabbiano, G., Carleton, N. P., Willner, S. P., and Lawrence, A. 1987, Ap. J., 315, 74.
- Weedman, D. W. 1976, Q. J. Roy. Astr. Soc., 17, 227.
- Weedman, Daniel W. 1983, Ap. J., 266, 479.
- Whitford, A. E. 1958, A. J., 63, 201.
- Yee, H. K. C. 1980, Ap. J., 241, 894.